A Measurement of the $B^0 \to J/\psi K^{*0}$ Branching Ratio and Calorimeter Studies Using the BaBar Detector

James Weatherall

February 2000

THE UNIVERSITY
of MANCHESTER

Particle Physics Group
Department of Physics and Astronomy

A thesis submitted to The University of Manchester for the degree of Doctor of Philosophy in the Faculty of Science and Engineering

Contents

Abstract

The BaBar experiment which has been designed to measure *CP* violation in the B meson system has been collecting data from e^+e^- colliding beam events since May 1999. A principal component of the detector is the CsI crystal electromagnetic calorimeter (EMC). Studies have been carried out to show how effective the EMC can be at identifying muons. Consequently software has been developed as part of the data reconstruction chain to produce particle identification statistics for a given detector measurement under the muon hypothesis.

The calibration of the EMC using minimum ionizing particles has been studied and also put into practice, using cosmic ray muons to provide an initial set of calibration constants for the individual crystals. The software to carry out the calibration procedure is at a stage where it can be used on $e^+e^- \to \mu^+\mu^-$ events as part of a rolling calibration.

An analysis of the B^0 decay modes to $J/\psi(l^+l^-)K^{*0}(K_S\pi^0)$ and $J/\psi(l^+l^-)K^{*0}(K^\pm\pi^\mp)$ involving a full selection process for these events from all data has been pursued. Use of the EMC π^0 calibration is shown to improve the $K^{*0} \to K_S\pi^0$ signal. The branching fraction for the decay $B^0 \to J/\psi(l^+l^-)K^{*0}(K^\pm\pi^\mp)$ is measured to be

$$BR\left[B^0 \to J/\psi(l^+l^-)K^{*0}(K^\pm\pi^\mp)\right] = (9.3 \pm 2.7 \pm 1.6) \times 10^{-5}$$

where the first error is statistical and the second systematic. This is in good agreement with the expected value. The future prospects for this channel given higher statistics are good and it will eventually yield a competitive measurement of the unitarity triangle parameter $\sin 2\beta$.

Declaration

No portion of the work referred to in this thesis has been submitted in support of an application for another degree or qualification of this or any other university or other institute of learning.

The Author

The author was educated at King Edward VI School, Louth, Lincolnshire between 1989 and 1993 before obtaining a 1st class BSc (Hons) degree in Physics at the University of Manchester in 1996. The work presented in this thesis was conducted at the University of Manchester and the Stanford Linear Accelerator Center, California.

Acknowledgements

This thesis would not exist in its current form (or perhaps at all!) if it were not for the assistance of other people, a few of whom I attempt to thank here. At SLAC I was privileged to work with some extremely capable physicists who provided endless help when I really needed it. Two who stand out are Paul Harrison and Helmut Marsiske. As for my time in Manchester, it was helped greatly by the gentle direction and ceaseless wisdom provided by my supervisor, Roger Barlow.

Friends are also invaluable, especially through those dark days of thesis writing. A lot of people came and went during my time at Manchester and SLAC. I thank Paul Bate for the discussion of life in its many guises and constant thrashings at squash in an attempt to tone both my body and mind; Dave Futyan for continuous comical quotes and the immortalization of the word 'gauge'; Nik Savvas for increasing my education in world politics and for those drunken nights in SF, USVI, Padova and Manchester; Dan Smith for the pizzas and philosophical debates at Oasis; Mark Williams for some memorable nights and right wing crosses.

Equally I thank my family who, although not with me in person through the whole sordid business, provided continuous love and support from a distance. Finally, large vats of gratitude to Julie, who tolerated the mood swings of a frustrated wannabe scientist for a large fraction of the journey.

Chapter 1

CP Violation in the B Meson System

1.1 Introduction

The main aim of the BABAR experiment is to study CP violation in the neutral B meson system. CP violation in general is one of the least well tested aspects of the standard model and so far has been seen only in the neutral K meson system [1]. However, it is one of the necessary conditions to explain the baryon asymmetry of the universe [2] and is an essential property of the CKM picture of the quark sector [3]. CP violation requires at least three generations of quarks and indeed was in turn one of the motivations for Kobayashi and Maskawa to construct their theory.

This chapter will explain first the phenomenon of mixing in neutral meson systems, an effect which plays a profound role in the manifestation of CP-violating effects. Specific cases will then be considered, in particular those of the neutral B and K meson systems. Finally, ways of measuring CP violation in the B meson system will be described along with a review of the current status of the CKM matrix parameters.

1.2 Neutral Meson Mixing

Consider first the Schrödinger equation for a *single* particle in its own rest frame

$$i\hbar\frac{\partial|\psi\rangle}{\partial t} = E|\psi\rangle. \tag{1.1}$$

It can also be written

$$\frac{\partial|\psi\rangle}{\partial t} = -i\frac{mc^2}{\hbar}|\psi\rangle \tag{1.2}$$

with solution

$$|\psi(t)\rangle \propto e^{-imc^2t/\hbar} = e^{-imt}(\hbar = c = 1). \tag{1.3}$$

So the wave function oscillates with a frequency given by the rest mass of the particle. Of course there is also a spatial part to the wavefunction, which is omitted in this explanation to highlight the time dependence. Suppose now that the particle is unstable and therefore its amplitude is decreasing according to an exponential decay law. An extra term appears:

$$\frac{\partial|\psi\rangle}{\partial t} = -im|\psi\rangle - \Gamma/2|\psi\rangle \tag{1.4}$$

and now the solution is

$$|\psi(t)\rangle \propto e^{-imt}e^{-\Gamma t/2} \tag{1.5}$$

where the factor of 2 is simply so that the probability $\langle\psi|\psi\rangle$ is proportional to $e^{-\Gamma t}$. This solution can be written more compactly as

$$\frac{\partial|\psi\rangle}{\partial t} = -iA|\psi\rangle, \qquad |\psi(t)\rangle \propto e^{-iAt} \tag{1.6}$$

where A is a complex number with $\Re(A) = m$ and $\Im(A) = -\Gamma/2$.

Now consider a system of two states $|\psi_1\rangle$ and $|\psi_2\rangle$ which in general have different masses and decay constants. In addition, suppose these two states can mix into one another such that ψ_1 has a contribution which is proportional to the amount of ψ_2 present and vice versa. This leads to matrix elements such as

$$\mathcal{M}_{12} = \langle\psi_1|\widehat{H}|\psi_2\rangle = M_{12} - i\Gamma_{12}/2 \tag{1.7}$$

where the M_{ij} and Γ_{ij} are elements of the mass and decay matrices respectively. Now there are two equations

$$i\frac{\partial}{\partial t}\begin{pmatrix} |\psi_1\rangle \\ |\psi_2\rangle \end{pmatrix} = \begin{pmatrix} \mathcal{M}_{11} & \mathcal{M}_{12} \\ \mathcal{M}_{21} & \mathcal{M}_{22} \end{pmatrix}\begin{pmatrix} |\psi_1\rangle \\ |\psi_2\rangle \end{pmatrix}. \tag{1.8}$$

This represents two coupled modes. If you start off with an initially pure state ψ_1 then at any time later you will in general have a $\psi_1 - \psi_2$ mixture. However, one can always decouple the modes by diagonalising the matrix $\mathcal{M}$. Here we consider only cases where $|\psi_1\rangle$ and $|\psi_2\rangle$ are particle and antiparticle, $|\psi\rangle$ and $|\overline{\psi}\rangle$. CPT invariance asserts that the masses and widths of these two states are equal which makes the diagonal elements of $\mathcal{M}$ equal. *CP* symmetry(if it were true!) on the other hand, makes the off-diagonal elements equal yielding

$$i\frac{\partial}{\partial t}\begin{pmatrix} |\psi\rangle \\ |\overline{\psi}\rangle \end{pmatrix} = \begin{pmatrix} A & B \\ B & A \end{pmatrix}\begin{pmatrix} |\psi\rangle \\ |\overline{\psi}\rangle \end{pmatrix}. \tag{1.9}$$

The eigenvalues are readily found to be $A + B$ and $A - B$ and the two decoupled modes are

$$|\psi_+\rangle = \frac{1}{\sqrt{2}}\left(|\psi\rangle + |\overline{\psi}\rangle\right) \qquad |\psi_-\rangle = \frac{1}{\sqrt{2}}\left(|\psi\rangle - |\overline{\psi}\rangle\right) \tag{1.10}$$

with decoupled equations

$$i\frac{\partial|\psi_+\rangle}{\partial t} = M_+|\psi_+\rangle - i\Gamma_+/2|\psi_+\rangle \qquad i\frac{\partial|\psi_-\rangle}{\partial t} = M_-|\psi_-\rangle - i\Gamma_-/2|\psi_-\rangle \tag{1.11}$$

with solutions

$$|\psi_+(t)\rangle \propto e^{-iM_+t}e^{-\Gamma_+t/2} \qquad |\psi_-(t)\rangle \propto e^{-iM_-t}e^{-\Gamma_-t/2} \tag{1.12}$$

where

$$M_\pm = \Re\left(A \pm B\right) \qquad -\Gamma_\pm/2 = \Im\left(A \pm B\right). \tag{1.13}$$

The original states $|\psi\rangle$ and $|\overline{\psi}\rangle$ are eigenstates of the strong interaction. These decoupled states, however are eigenstates of the mass and of *CP*. In particular

$$\widehat{CP}|\psi_\pm\rangle = \pm|\psi_\pm\rangle. \tag{1.14}$$

Thus far the framework for a mixing, *CP* conserving neutral meson system has been outlined. To get the full picture, one must allow for the possibility of *CP* violation and rewrite the mixing equations thus

$$i\frac{\partial}{\partial t}\begin{pmatrix} |\psi\rangle \\ |\overline{\psi}\rangle \end{pmatrix} = \begin{pmatrix} A & B/r \\ rB & A \end{pmatrix}\begin{pmatrix} |\psi\rangle \\ |\overline{\psi}\rangle \end{pmatrix}. \tag{1.15}$$

Using the same diagonalisation procedure as before, the decoupled states are found to be

$$|\psi_S\rangle = \frac{1}{\sqrt{1+|r|^2}}\left(|\psi\rangle + r|\overline{\psi}\rangle\right) \qquad |\psi_L\rangle = \frac{1}{\sqrt{1+|r|^2}}\left(|\psi\rangle - r|\overline{\psi}\rangle\right) \tag{1.16}$$

with the masses and widths of the states coming from the real and imaginary parts of $A \pm B$ as before. The fact that *CP*-violating effects are small means that r is approximately 1 and that ψ_S and ψ_L are almost the same as ψ_+ and $\psi-$. In practice, it is convenient to use the parameter ϵ which is defined as

$$\epsilon = \frac{1-r}{1+r}. \tag{1.17}$$

1.3 Time Evolution of Neutral B_d Mesons

By analogy with equation 1.16 consider the light B_L and heavy B_H neutral B_d meson mass eigenstates as linear combinations of the flavour eigenstates

$$|B_L\rangle = p|B^0\rangle + q|\overline{B}^0\rangle \tag{1.18}$$

$$|B_H\rangle = p|B^0\rangle - q|\overline{B}^0\rangle \tag{1.19}$$

where p and q are complex and obey the normalization condition

$$|q|^2 + |p|^2 = 1. \tag{1.20}$$

The mass difference Δm_B and width difference $\Delta\Gamma_B$ between the two states are defined as follows:

$$\Delta m_B \equiv M_H - M_L, \quad \Delta\Gamma_B \equiv \Gamma_H - \Gamma_L, \tag{1.21}$$

so that Δm_B is positive by definition.

The lifetime difference is expected to be negligible [4],

$$\Delta\Gamma_B/\Gamma_B = \mathcal{O}(10^{-2}) \tag{1.22}$$

and it should be noted that it has not yet been measured. The difference in widths is produced by decay channels which are common to B^0 and $\overline{B}^0$. Their branching ratios are at or below the level of 10^{-3} and since they contribute with differing signs, it is expected that their sum will not exceed the individual level. Therefore the assumption $\Delta\Gamma_{B_d} \ll \Gamma_{B_d}$ is safe and model independent.

In contrast, the mass difference Δm_{B_d} has been measured [5],

$$x_d \equiv \Delta m_{B_d}/\Gamma_{B_d} = 0.723 \pm 0.032. \tag{1.23}$$

From 1.22 and 1.23 it can be seen that,

$$\Delta\Gamma_B \ll \Delta m_B. \tag{1.24}$$

Now, any B state can be written as an admixture of B_H and B_L, with amplitudes that evolve in time as

$$a_H(t) = a_H(0)e^{-iM_H t}e^{-\frac{1}{2}\Gamma_H t}, \quad a_L(t) = a_L(0)e^{-iM_L t}e^{-\frac{1}{2}\Gamma_L t}. \tag{1.25}$$

A state which is created at time $t = 0$ as pure B^0 has $a_L(0) = a_H(0) = 1/(2p)$. An initially pure $\overline{B}^0$ has $a_L(0) = -a_H(0) = 1/(2q)$ (from equations 1.18 and 1.19). Taking the approximation $\Gamma_H = \Gamma_L(= \Gamma)$ gives the time evolution of these states to be

$$|B^0(t)\rangle = g_+(t)|B^0\rangle + (q/p)g_-(t)|\overline{B}^0\rangle, \tag{1.26}$$

$$|\overline{B}^0(t)\rangle = (p/q)g_-(t)|B^0\rangle + g_+(t)|\overline{B}^0\rangle, \tag{1.27}$$

where

$$g_+(t) = e^{-iMt}e^{-\Gamma t/2}\cos(\Delta m_B\, t/2), \tag{1.28}$$

$$g_-(t) = e^{-iMt}e^{-\Gamma t/2}i\sin(\Delta m_B\, t/2), \tag{1.29}$$

and $M = \frac{1}{2}(M_H + M_L)$. These results will be useful later in this chapter when we describe how CP violation arises in B decays.

1.4 Coherent Production of B Meson Pairs

This section considers the consequences of producing neutral B mesons at a 'B factory', that is an e^+e^- collider operating at the $\Upsilon(4S)$ resonance. In this situation, the B^0 and $\overline{B}^0$ are produced in a *coherent* state with $L = 1$. The result is that each of the particles evolves in time individually as in section 1.3. However they evolve in phase such that at any one time, until one of them decays, there is always exactly one B^0 and one $\overline{B}^0$ present. After the decay of one of the particles, the other continues to evolve until it in turn decays.

The implication of this is that it is possible to tag the flavour of the B mesons. To measure CP asymmetries one typically looks for events where one B decays to a CP eigenstate final state f_{CP} at time t_f, while the second decays to a tagging mode, that is a mode which identifies its b-flavour, at time t_{tag}. Say that one B was identified as a $\overline{B}^0$ through its decay to a tagging mode. This then identifies the *other* particle as a B^0 at time $t = t_{tag}$. The method works even when the tagging B decays *after* the CP mode B. In this case the latter must be just that mixture which, had it not decayed, would have evolved to be the opposite flavour at $t = t_{tag}$.

1.5 The Three Types of CP Violation in B Decays

Given this knowledge of the time evolution, and therefore mixing, of neutral B mesons it is useful now to describe the different ways in which CP violation can occur in this system. Study of both the neutral and charged sectors has relevance to CP measurements in this case. There are three possible manifestations of CP violation

within the B meson system and these can be expressed in a model-independent way:

1. *CP* violation in decay, which occurs in both charged and neutral decays, when the amplitude for a decay and its *CP* conjugate process have different magnitudes.

2. *CP* violation in mixing, which occurs when the two neutral mass eigenstates cannot be chosen to be *CP* eigenstates.

3. *CP* violation in the interference between decays with and without mixing, which occurs in decays into final states that are common to B^0 and $\overline{B}^0$. It often occurs in combination with the other two types but in BABAR there are cases when, to an excellent approximation, it is the only effect.

It is useful now to identify a particular *CP*-violating quantity for each case that is independent of phase conventions and discuss the types of processes that depend on this quantity[1].

1.5.1 *CP* Violation in Decay

Let A_f and $\overline{A}_{\overline{f}}$ represent the amplitudes for B and $\overline{B}$ respectively to decay to a final state f. In such a scheme, the quantity $\left|\frac{\overline{A}_{\overline{f}}}{A_f}\right|$ is independent of phase conventions and physically meaningful. There are two types of phases that can appear in A_f and $\overline{A}_{\overline{f}}$.

Complex parameters from Lagrangian terms contributing to the amplitude will appear in complex conjugate form in the *CP* conjugate amplitude. This means that their phases will appear in A_f and $\overline{A}_{\overline{f}}$ with opposite signs. In the standard model, these phases come from the electroweak sector of the theory via the CKM matrix. Hence, they are often called "weak phases". The weak phase of any one term is

[1]Much of what follows can be found in [6].

convention dependent but the difference between the weak phases of two different terms in A_f is convention independent.

A second type of phase can appear in scattering or decay amplitudes even when the Lagrangian is purely real. These phases do not violate *CP* since they appear in the two amplitudes with equal sign. Their origin is the possible contribution from intermediate on-shell states in the decay process. The dominant rescattering of these states is usually due to strong interactions, hence the designation "strong phases" for these phase shifts. As before, only relative phases in different terms of a scattering amplitude have any physical content, an overall phase rotation of the entire amplitude has no physical consequences.

Thus it is useful to write each contribution to A in three parts: its magnitude A_i, its weak phase term $e^{i\phi_i}$ and its strong phase term $e^{i\delta_i}$. Then if several amplitudes contribute to the process $B \to f$, the amplitude A_f is given by:

$$A_f = \sum_i A_i e^{i(\delta_i + \phi_i)} \tag{1.30}$$

and the corresponding convention-independent quantity is

$$\left|\frac{\overline{A}_{\overline{f}}}{A_f}\right| = \left|\frac{\sum_i A_i e^{i(\delta_i - \phi_i)}}{\sum_i A_i e^{i(\delta_i + \phi_i)}}\right|. \tag{1.31}$$

Inspection of the amplitudes A_f and $\overline{A}_{\overline{f}}$ tells us that in the case of *CP* conservation, all the ϕ_i must be equal. This in fact leaves a relative phase between the two amplitudes but one which is arbitrary and can be set to zero. Thus, equation 1.31 tells us that

$$\left|\overline{A}_{\overline{f}}/A_f\right| \neq 1 \implies CP \text{ violation.} \tag{1.32}$$

This is *CP violation in decay.* It is also called *direct CP violation.* It is a result of interference amongst the various terms in the decay amplitude. *CP* violation of this type will not be seen unless at least two terms that have different weak phases have different strong phases also, since

$$|A|^2 - |\overline{A}|^2 = -2\sum_{i,j} A_i A_j sin(\phi_i - \phi_j) sin(\delta_i - \delta_j). \tag{1.33}$$

Asymmetries in charged B decays,

$$a_f = \frac{\Gamma(B^+ \to f) - \Gamma(B^- \to \overline{f})}{\Gamma(B^+ \to f) + \Gamma(B^- \to \overline{f})} \tag{1.34}$$

are from this type of *CP* violation. *CP* violation in the decay can also occur in neutral meson decays but there it competes with the other two types explained below. The most compelling evidence to date for the existence of direct *CP* violation is from the KTeV experiment at Fermilab. This will be reviewed in section 1.6.

1.5.2 *CP* Violation in Mixing

Finding the eigenvalues of the equivalent of equation 1.15 for the B system gives a second quantity which is independent of phase conventions and physically meaningful,

$$\left|\frac{q}{p}\right|^2 = \left|\frac{M_{12}^* - \frac{i}{2}\Gamma_{12}^*}{M_{12} - \frac{i}{2}\Gamma_{12}}\right|. \tag{1.35}$$

If *CP* is conserved, the mass eigenstates are also the *CP* eigenstates. Inspection of q and p shows that in this case the relative phase between M_{12} and Γ_{12} must vanish. In fact there is still a relative phase between q and p but one which can be accounted for by a suitable definition of $B - \overline{B}$ phase difference, which we are free to choose. This leads to

$$|q/p| \neq 1 \implies CP \text{ violation.} \tag{1.36}$$

This is *CP violation in mixing*. It is also called *indirect CP violation*. It arises because the mass eigenstates are different from the *CP* eigenstates. This type of *CP* violation has been unambiguously observed in the neutral kaon system.

This could be measured in the B system by studying semileptonic decays:

$$a_{sl} = \frac{\Gamma(\overline{B}^0(t) \to l^+\nu X) - \Gamma(B^0(t) \to l^-\nu X)}{\Gamma(\overline{B}^0(t) \to l^+\nu X) + \Gamma(B^0(t) \to l^-\nu X)}. \tag{1.37}$$

Or, in terms of $|q/p|$,

$$a_{sl} = \frac{1 - |q/p|^4}{1 + |q/p|^4}, \tag{1.38}$$

since

$$\langle l^- \nu X|\widehat{H}|B^0(t)\rangle = (q/p)g_-(t)\overline{A}, \quad \langle l^+ \nu X|\widehat{H}|\overline{B}^0(t)\rangle = (p/q)g_-(t)A. \tag{1.39}$$

Such asymmetries are expected to be small, $\mathcal{O}(10^{-2})$ [4]. Moreover, it is difficult to calculate $|q/p|$ since this requires calculation of Γ_{12} and M_{12} which involves large hadronic uncertainties. Thus even if these asymmetries are observed, it will be difficult to relate their rates to fundamental CKM parameters.

1.5.3 *CP* Violation in the Interference Between Mixing and Decay

Now consider neutral B decays to final states which are eigenstates of CP, f_{CP}. Such states are accessible in both B^0 and $\overline{B}^0$ decays. The physically meaningful, phase convention independent quantity here is

$$\lambda \equiv \frac{q}{p}\frac{\overline{A}_{f_{CP}}}{A_{f_{CP}}} = \eta_{f_{CP}}\frac{q}{p}\frac{\overline{A}_{\overline{f}_{CP}}}{A_{f_{CP}}}, \tag{1.40}$$

where $\eta_{f_{CP}}(= \pm 1)$ is the CP eigenvalue of the state f_{CP} and

$$\overline{A}_{f_{CP}} = \eta_{f_{CP}}\overline{A}_{\overline{f}_{CP}}. \tag{1.41}$$

When CP is conserved, $|q/p| = 1$, $|\overline{A}_{\overline{f}_{CP}}/A_{f_{CP}}| = 1$ and importantly for this type of CP violation, λ has no overall phase. To see this last point, start with equations 1.26 and 1.27. The amplitudes for the decays of the time evolved neutral B mesons are

$$\begin{aligned} \langle f_{CP}|\widehat{H}|B^0(t)\rangle &= A_{f_{CP}}(g_+(t) + \lambda g_-(t)), \\ \langle f_{CP}|\widehat{H}|\overline{B}^0(t)\rangle &= A_{f_{CP}}\frac{p}{q}(g_-(t) + \lambda g_+(t)). \end{aligned} \tag{1.42}$$

This gives

$$\begin{aligned} \Gamma(B^0(t) \to f_{CP}) &= |\langle f_{CP}|\widehat{H}|B^0(t)\rangle|^2 \\ &= |A_{f_{CP}}|^2 \left[e^{-\Gamma t}\cos^2(\frac{\Delta m_B t}{2}) + e^{-\Gamma t}|\lambda|^2 \sin^2(\frac{\Delta m_B t}{2})\right. \end{aligned}$$

$$+ ie^{-\Gamma t}\lambda\cos(\frac{\Delta m_B t}{2})\sin(\frac{\Delta m_B t}{2}) - ie^{-\Gamma t}\lambda^*\cos(\frac{\Delta m_B t}{2})\sin(\frac{\Delta m_B t}{2})\Big],$$
$$= |A_{f_{CP}}|^2 e^{-\Gamma t}\left[\frac{1+|\lambda|^2}{2} + \frac{1-|\lambda|^2}{2}\cos(\Delta m_B t) - \Im(\lambda)\sin(\Delta m_B t)\right]. \quad (1.43)$$

Similarly

$$\Gamma(\overline{B}^0(t)\to f_{CP}) = |A_{f_{CP}}|^2 e^{-\Gamma t}\left[\frac{1+|\lambda|^2}{2} - \frac{1-|\lambda|^2}{2}\cos(\Delta m_B t) + \Im(\lambda)\sin(\Delta m_B t)\right], \quad (1.44)$$

where the approximation $|q/p| = 1$ has been used (see the discussion in section 1.5.2).

If one now forms the difference of these rates divided by their sum, the time-dependent *CP* asymmetry is given by

$$\begin{aligned} a_{f_{CP}}(t) &= \frac{\Gamma(B^0(t)\to f_{CP}) - \Gamma(\overline{B}^0(t)\to f_{CP})}{\Gamma(B^0(t)\to f_{CP}) + \Gamma(\overline{B}^0(t)\to f_{CP})} \\ &= \frac{(1-|\lambda|^2)\cos(\Delta M t) - 2\Im(\lambda)\sin(\Delta M t)}{1+|\lambda|^2} \end{aligned} \quad (1.45)$$

which is non-zero if any of the three types of *CP* violation are present. However, in the absence of *CP* violation in the decay and in the mixing($|\lambda| = 1$) the asymmetry reduces to

$$a_{f_{CP}}(t) = -\Im(\lambda)\sin(\Delta m_B t). \quad (1.46)$$

where t is the difference in time between the decays of the two B mesons, $t_{f_{CP}} - t_{tag}$. Thus, even if *CP* violation in decay and *CP* violation in mixing are not present there can still be an asymmetry when $\Im(\lambda) \neq 0$. This is called *CP violation in the interference between decays with and without mixing* here. It is sometimes abbreviated to "interference between mixing and decay".

1.6 *CP* Violation in the K System

The description of mixing and *CP* violation given so far is enough to understand effects which have been observed to date in the K meson system. This is reviewed

with the purpose of making comparisons to the B system and to consider the implications for measurements of CP violation in the B system as provided by current knowledge of the K system.

The neutral K meson states differ significantly in their lifetimes [5]:

$$\tau_S = (0.8934 \pm 0.0008) \times 10^{-10}\text{s}, \quad \tau_L = (5.17 \pm 0.04) \times 10^{-8}\text{s} \tag{1.47}$$

where the S and L stand for (rather appropriately) short-lived and long-lived mass eigenstates. Due to this distinction it is often useful to define the eigenstates by the lifetimes,

$$|K_S\rangle = p|K^0\rangle + q|\overline{K}^0\rangle, \tag{1.48}$$

$$|K_L\rangle = p|K^0\rangle - q|\overline{K}^0\rangle \tag{1.49}$$

and say that $\Delta\Gamma_K > 0$ by definition. The q and p parameters here are analogous to their counterparts in the B system. The mass difference in the K system [5] is measured to be

$$\Delta m_K \equiv m_L - m_S = (3.489 \pm 0.009) \times 10^{-12} MeV. \tag{1.50}$$

It turns out that equations 1.47 and 1.50 produce a useful rule of thumb:

$$\Delta\Gamma_K \approx -2\Delta m_K, \tag{1.51}$$

which is in stark contrast to the situation for the B system shown in equation 1.24.

To date, CP violation has only been measured in K decays[2]. A number of complementary measurements have been made. An asymmetry in semileptonic decays of the K_L,

$$\delta = \frac{\Gamma(K_L \to \pi^- l^+ \nu_l) - \Gamma(K_L \to \pi^+ l^- \overline{\nu}_l)}{\Gamma(K_L \to \pi^- l^+ \nu_l) + \Gamma(K_L \to \pi^+ l^- \overline{\nu}_l)} \tag{1.52}$$

[2]The best determination so far of CP violation in the B system is by the CDF collaboration [7] who measured $\sin 2\beta = 0.79^{+0.41}_{-0.44}$. This can be interpreted as evidence for non-zero CP violation in the B system at 93% CL.

has been measured(for example see [8]), giving

$$\delta = (0.327 \pm 0.012)\%. \tag{1.53}$$

These asymmetries represent CP violation in K mixing:

$$\delta = \frac{1 - |q/p|_K^2}{1 + |q/p|_K^2} \tag{1.54}$$

where $|q/p|_K$ is very close to unity. In the two-pion channels, the asymmetries are

$$\eta_{00} = \frac{A(K_L \to \pi^0\pi^0)}{A(K_S \to \pi^0\pi^0)}, \qquad \eta_{+-} = \frac{A(K_L \to \pi^+\pi^-)}{A(K_S \to \pi^+\pi^-)}, \tag{1.55}$$

and fits over several measured values for these parameters [5] yield

$$|\eta_{00}| = (2.275 \pm 0.019) \times 10^{-3}, \quad \phi_{00} = 43.4 \pm 1.0 \tag{1.56}$$

$$|\eta_{+-}| = (2.285 \pm 0.019) \times 10^{-3}, \quad \phi_{+-} = 43.5 \pm 0.6. \tag{1.57}$$

The ratios are sensitive to all three types of CP violation since

$$\eta_{00} = \frac{pA_{00} - q\overline{A}_{00}}{pA_{00} + q\overline{A}_{00}} = \frac{1 - \lambda_{00}}{1 + \lambda_{00}}, \quad \eta_{+-} = \frac{pA_{+-} - q\overline{A}_{+-}}{pA_{+-} + q\overline{A}_{+-}} = \frac{1 - \lambda_{+-}}{1 + \lambda_{+-}}. \tag{1.58}$$

1.6.1 The Parameters ϵ_K and ϵ'_K

It is useful now to consider the two-pion decay amplitudes in terms of isospin channels. The strong interaction does not distinguish between charged and neutral pions but is sensitive to whether the final state is $I = 0$ or $I = 2$. The neutral and charged modes can be decomposed via Clebsch-Gordan coefficients,

$$\langle\pi^0\pi^0| = \sqrt{\frac{1}{3}}\langle(\pi\pi)_{I=0}| - \sqrt{\frac{2}{3}}\langle(\pi\pi)_{I=2}|, \tag{1.59}$$

$$\langle\pi^+\pi^-| = \sqrt{\frac{2}{3}}\langle(\pi\pi)_{I=0}| + \sqrt{\frac{1}{3}}\langle(\pi\pi)_{I=2}|. \tag{1.60}$$

Writing η_{00} and η_{+-} in terms of these amplitudes gives

$$\eta_{00} = \epsilon_K - \frac{2\epsilon'_K}{1 - w\sqrt{2}} \simeq \epsilon_K - 2\epsilon'_K, \quad \eta_{+-} = \epsilon_K + \frac{\epsilon'_K}{1 + w/\sqrt{2}} \simeq \epsilon_K + \epsilon'_K \tag{1.61}$$

where w measures the ratio of isospin amplitudes:

$$|w| \equiv \left| \frac{\langle (\pi\pi)_{I=2} | \widehat{H} | K_S \rangle}{\langle (\pi\pi)_{I=0} | \widehat{H} | K_S \rangle} \right| \simeq 1/22.2. \tag{1.62}$$

The smallness of this experimental value of $|w|$ is known as the $\Delta I = 1/2$ selection rule of $K \to \pi\pi$ decays [9]. The parameters ϵ_K and ϵ'_K represent *CP* violation and are given by

$$\epsilon_K = \frac{\langle (\pi\pi)_{I=0} | \widehat{H} | K_L \rangle}{\langle (\pi\pi)_{I=0} | \widehat{H} | K_S \rangle} \tag{1.63}$$

and

$$\epsilon'_K = \frac{\epsilon_K}{\sqrt{2}} \left\{ \frac{\langle (\pi\pi)_{I=2} | \widehat{H} | K_L \rangle}{\langle (\pi\pi)_{I=0} | \widehat{H} | K_L \rangle} - \frac{\langle (\pi\pi)_{I=2} | \widehat{H} | K_S \rangle}{\langle (\pi\pi)_{I=0} | \widehat{H} | K_S \rangle} \right\}. \tag{1.64}$$

By definition there is no direct *CP* violation in the equation for ϵ_K since it contains only one strong phase. In fact it represents both *CP* violation in the mixing and *CP* violation in the interference between mixing and decay with the two occurring with similar magnitudes. The equation for ϵ'_K has two strong phases and so represents direct *CP* violation to some degree. In fact, in turns out that it represents some combination of *CP* violation in the decay and *CP* violation in the interference between mixing and decay.

There has been a long search for direct *CP* violation in K decays with various experiments measuring the so called double ratio

$$\left| \frac{\eta_{+-}}{\eta_{00}} \right|^2 \simeq 1 + 6\Re \left(\frac{\epsilon'_K}{\epsilon_K} \right). \tag{1.65}$$

The best evidence so far is from the KTeV experiment at Fermilab [10] which found

$$\Re \left(\frac{\epsilon'_K}{\epsilon_K} \right) = (28.0 \pm 4.1) \times 10^{-4}. \tag{1.66}$$

This agrees favourably with the findings of the NA48 experiment at CERN [11] which has used early (1997) data to measure

$$\Re \left(\frac{\epsilon'_K}{\epsilon_K} \right) = (18.5 \pm 7.3) \times 10^{-4}. \tag{1.67}$$

1.7 Quark Mixing and the CKM matrix

Now we turn our attention to the Standard Model description of *CP* violation. For further information on this formalism see, for example [12], [13] and [14].

It is convenient for what follows to group together the left(L) and right(R) handed components of the quark fields u so that

$$U_L^I = \begin{pmatrix} u_L^I \\ c_L^I \\ t_L^I \end{pmatrix} \quad U_R^I = \begin{pmatrix} u_R^I \\ c_R^I \\ t_R^I \end{pmatrix} \quad D_L^I = \begin{pmatrix} d_L^I \\ s_L^I \\ b_L^I \end{pmatrix} \quad D_R^I = \begin{pmatrix} d_R^I \\ s_R^I \\ b_R^I \end{pmatrix} \tag{1.68}$$

where I denotes that these are eigenstates of the weak interaction. Consider the quark part of the Standard Model Lagrangian. The piece of this responsible for generating fermion masses via Yukawa interactions can be written

$$\mathcal{L}_{quarks}^{Y} = -\overline{D}_L^I m^d D_R^I - \overline{U}_L^I m^u U_R^I - \frac{\sigma}{v}\overline{D}_L^I m^d D_R - \frac{\sigma}{v}\overline{U}_L^I m^u U_R^I + \text{complex conjugates} \tag{1.69}$$

where m^u and m^d are the mass matrices for up and down type quarks respectively and σ and v are the usual Higgs field parameters. It is possible to diagonalize the mass matrices by expressing the interaction eigenstates as unitary transformations of the mass eigenstates

$$U_L^I = \Omega_L^u U_L, \quad U_R^I = \Omega_R^u U_R, \quad D_L^I = \Omega_L^d D_L, \quad D_R^I = \Omega_R^d D_R. \tag{1.70}$$

That is to say that the transformations are chosen so that

$$(\Omega_L^u)^\dagger m^u \Omega_R^u = \begin{pmatrix} m_u & 0 & 0 \\ 0 & m_c & 0 \\ 0 & 0 & m_t \end{pmatrix}, \quad (\Omega_L^d)^\dagger m^d \Omega_R^d = \begin{pmatrix} m_d & 0 & 0 \\ 0 & m_s & 0 \\ 0 & 0 & m_b \end{pmatrix}. \tag{1.71}$$

Now consider the charged current part of the aforementioned quark Lagrangian:

$$\mathcal{L}_{quarks}^{CC} = \frac{e}{\sqrt{2}\sin\theta_W}\overline{U}_L^I \gamma^\mu W_\mu^+ D_L^I + \text{complex conjugate} \tag{1.72}$$

where e and θ_W are the usual electroweak parameters and W^+ represents the charge raising operator of electroweak field theory. Rewriting 1.72 using equation 1.70 yields

$$\mathcal{L}^{CC}_{quarks} = \frac{e}{\sqrt{2}\sin\theta_W}\overline{U}_L\gamma^\mu W^+_\mu V D_L + \text{complex conjugate} \tag{1.73}$$

where

$$V = (\Omega^u_L)^\dagger \Omega^d_L \equiv \begin{pmatrix} V_{ud} & V_{us} & V_{ub} \\ V_{cd} & V_{cs} & V_{cb} \\ V_{td} & V_{ts} & V_{tb} \end{pmatrix} \tag{1.74}$$

is a unitary matrix called the *Cabibbo-Kobayashi-Maskawa matrix*. It embodies cross-generational mixing in the quark sector of the Standard Model.

It is perhaps interesting to note that the leptonic sector has no equivalent of this phenomenon within the Standard Model. The reason for this is that the right handed components of the neutrino fields have been excluded and therefore the relevant part of the Lagrangian has no analogue of the up-type mass terms shown in equation 1.69. However, if the neutrino mass is non-zero, then there will be such a contribution from the leptonic sector.

The CKM matrix is a complex matrix of dimension $N = 3$, and as such has in general $2N^2 = 18$ parameters. It is however a unitary matrix and this imposes 9 constraints reducing the number of parameters to 9. Three of these parameters can be represented by Euler angles since if V had been real, then it would just be a three dimensional rotation. The other 6 are phases. One is free to redefine the quark fields so that

$$\begin{pmatrix} \overline{u'}_L \\ \overline{c'}_L \\ \overline{t'}_L \end{pmatrix} = P_u \begin{pmatrix} \overline{u}_L \\ \overline{c}_L \\ \overline{t}_L \end{pmatrix}, \quad \begin{pmatrix} \overline{d'}_L \\ \overline{s'}_L \\ \overline{b'}_L \end{pmatrix} = P_d \begin{pmatrix} \overline{d}_L \\ \overline{s}_L \\ \overline{b}_L \end{pmatrix} \tag{1.75}$$

where P_u and P_d are diagonal and consist only of pure phases. The transformation

causes a redefinition of V:

$$V' = \begin{pmatrix} e^{-i(\phi_1-\xi_1)}V_{ud} & e^{-i(\phi_1-\xi_2)}V_{us} & e^{-i(\phi_1-\xi_3)}V_{ub} \\ e^{-i(\phi_2-\xi_1)}V_{cd} & e^{-i(\phi_2-\xi_2)}V_{cs} & e^{-i(\phi_2-\xi_3)}V_{cb} \\ e^{-i(\phi_3-\xi_1)}V_{td} & e^{-i(\phi_3-\xi_2)}V_{ts} & e^{-i(\phi_3-\xi_3)}V_{tb} \end{pmatrix} \tag{1.76}$$

where ϕ_i is a phase of $(P_u)_{ii}$ and ξ_i that of $(P_d)_{ii}$. It is clear that there can be no more than 5 independent phase differences in this expression and so a maximum of 5 phases can be removed in this way. This leaves 4 parameters: 3 real angles and 1 complex phase. It is the irremovability of this phase that results in *CP* violation.

To see this consider the coupling shown in equation 1.73 in expanded form:

$$\mathcal{L}^{CC}_{quarks} = \frac{e}{2\sqrt{2}\sin\theta_W}\left\{\overline{U}_i\gamma^\mu W^+_\mu(1-\gamma_5)V_{ij}D_j + \overline{D}_j\gamma^\mu W^-_\mu(1-\gamma_5)V^*_{ij}U_i\right\} \tag{1.77}$$

where the left-handed quark field components have been replaced by the left-handed projection operator $\frac{1}{2}(1-\gamma_5)$ acting on the complete quark fields. The operation of *CP* on these terms has the following effect

$$\overline{\psi}_i\gamma^\mu W^+_\mu(1-\gamma_5)\psi_j \quad \rightarrow \quad \overline{\psi}_j\gamma^\mu W^-_\mu(1-\gamma_5)\psi_i. \tag{1.78}$$

Thus *CP* interchanges the two terms apart from exchanging V_{ij} and V^*_{ij}. If the CKM matrix has irremovable complexity, then *CP* can be violated as long as the phase does not equal 0 or π.

All this is still not enough to ensure non-zero *CP* violation. If two quarks of the same charge had equal mass, one Euler angle and the phase could be removed from V. Thus, *CP* violation requires

$$(m_t^2-m_c^2)(m_c^2-m_u^2)(m_t^2-m_u^2)(m_b^2-m_s^2)(m_s^2-m_d^2)(m_b^2-m_d^2) \neq 0 \tag{1.79}$$

where the mass terms are squared because the sign of a fermion mass term is not physical. Similarly, if any of the three mixing angles were 0 or $\pi/2$ then the phase could also be removed.

1.7.1 The Unitarity Triangle

The properties of the CKM matrix become manifest once it is explicitly parametrized. Many different parameterizations are possible, but the standard one is the following [5]:

$$V = \begin{pmatrix} c_{12}c_{13} & s_{12}c_{13} & s_{13}e^{-i\delta} \\ -s_{12}c_{23} - c_{12}s_{23}s_{13}e^{i\delta} & c_{12}c_{23} - s_{12}s_{23}s_{13}e^{i\delta} & s_{23}c_{13} \\ s_{12}s_{23} - c_{12}c_{23}s_{13}e^{i\delta} & -c_{12}s_{23} - s_{12}c_{23}s_{13}e^{i\delta} & c_{23}c_{13} \end{pmatrix}, \tag{1.80}$$

where $c_{ij} \equiv \cos\theta_{ij}$ and $s_{ij} \equiv \sin\theta_{ij}$ represent the three mixing angles ($i \neq j$) and δ is the *CP*-violating phase. A useful way to express the requirements $\theta_{ij} \neq 0, \pi/2$ and $\delta \neq 0, \pi$ was noticed by Jarlskog [15], [16]. Crossing out an arbitrary row r and column s of V and denoting the remaining submatrix by

$$\begin{pmatrix} V_{ij} & V_{ik} \\ V_{lj} & V_{lk} \end{pmatrix} \tag{1.81}$$

yields the quantity J

$$J = (-1)^{r+s}\Im(V_{ij}V_{lk}V_{ik}^*V_{lj}^*). \tag{1.82}$$

It turns out that this quantity is invariant under the phase transformations of equations 1.75 and must be non zero for *CP* violation to occur (where we have assumed non-degeneracy of the like-charge quark field masses). Expressing J in terms of the CKM parameterization shown above gives

$$J = c_{12}c_{23}c_{13}^2 s_{12}s_{23}s_{13}\sin\delta \tag{1.83}$$

which shows explicitly the requirements on the mixing angles and δ. Since the magnitude of J is estimated to be of the order 10^{-4} [17], *CP* violation in the Standard Model is expected to be a small effect.

Another popular parameterization involves making use of the fact that $s_{12} \simeq 0.22$, where λ shall be used in place of s_{12} from now on. Experimentally, it is known

that $s_{23} = \mathcal{O}(\lambda^2)$ and $s_{13} = \mathcal{O}(\lambda^3)$ and so it is natural to define $s_{23} = A\lambda^2$ and $s_{13}e^{-i\delta} = A\lambda^3(\rho - i\eta)$ where A, ρ and η are of order unity. An expansion in λ produces the Wolfenstein parameterization:

$$V = \begin{pmatrix} 1-\lambda^2/2 & \lambda & A\lambda^3(\rho - i\eta) \\ -\lambda & 1-\lambda^2/2 & A\lambda^2 \\ A\lambda^3(1-\rho-i\eta) & -A\lambda^2 & 1 \end{pmatrix} + \mathcal{O}(\lambda^4). \tag{1.84}$$

The unitarity of the CKM matrix produces certain relations among its elements. It turns out that three of these are useful for understanding *CP* violation in the standard model:

$$\begin{aligned} V_{ud}V_{us}^* + V_{cd}V_{cs}^* + V_{td}V_{ts}^* &= 0, \\ V_{us}V_{ub}^* + V_{cs}V_{cb}^* + V_{ts}V_{tb}^* &= 0, \\ V_{ud}V_{ub}^* + V_{cd}V_{cb}^* + V_{td}V_{tb}^* &= 0. \end{aligned} \tag{1.85}$$

These expressions all require the sum of three complex numbers to vanish and so can be represented as triangles in the complex plane. The areas of the triangles are all equal to $|J|/2$ [18] and so the more open a triangle is, the more *CP* violation it represents. Current experimental values indicate that the first two triangles have one side much shorter than the other two. They collapse almost to a line and give some intuitive understanding of why *CP* violation is small in the leading K decays (the first triangle) and the leading B_s decays (the second triangle). The third triangle is the most exciting for the study of *CP* violation as it is rather more open than the other two and predicts large *CP* asymmetries in B decays. It is called *the* Unitarity Triangle. It is useful to show this triangle in its rescaled form. Since $V_{cd}V_{cb}^*$ is real, this side lies along the horizontal axis and its length is normalized by dividing all sides by $|V_{cd}V_{cb}^*|$. The apex of the triangle then lies at (ρ, η) as shown in figure 1.1. The three angles are labelled α, β and γ and are given by

$$\alpha \equiv \arg\left[-\frac{V_{td}V_{tb}^*}{V_{ud}V_{ub}^*}\right], \quad \beta \equiv \arg\left[-\frac{V_{cd}V_{cb}^*}{V_{td}V_{tb}^*}\right], \quad \gamma \equiv \arg\left[-\frac{V_{ud}V_{ub}^*}{V_{cd}V_{cb}^*}\right]. \tag{1.86}$$

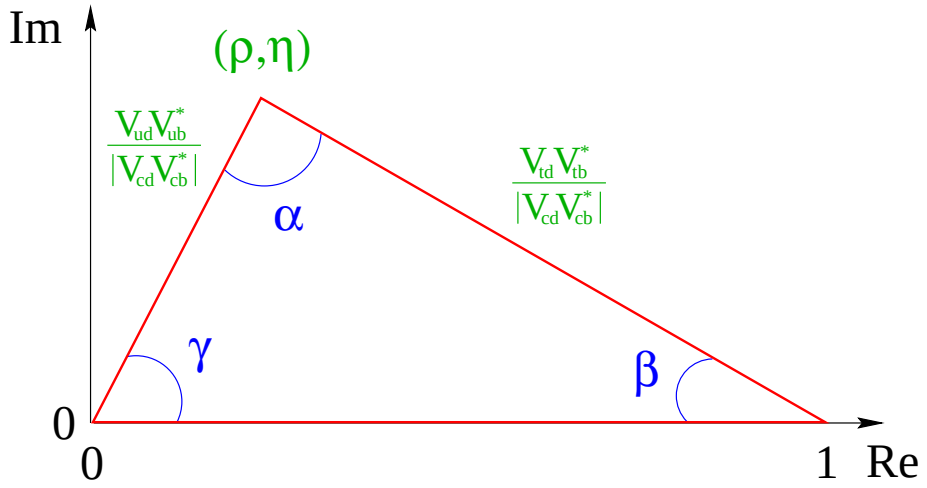

Figure 1.1: *The rescaled Unitarity Triangle.*

They are physical quantities and represent the amount of *CP* violation in the B system. It is possible to measure them by studying *CP* asymmetries in various B decays.

1.7.2 Measurement of Unitarity Triangle Angles

Recall the definition of λ from equation 1.40

$$\lambda = \frac{q}{p}\frac{\overline{A}}{A} \tag{1.87}$$

(not to be confused with the Wolfenstein λ!) where the decay is to a *CP* eigenstate. The q/p part of this comes from B^0 mixing processes such as figure 1.2(a) and can be written as(from equation 1.35)

$$\frac{q}{p} = \left(\frac{M_{12}^* - \frac{i}{2}\Gamma_{12}^*}{M_{12} - \frac{i}{2}\Gamma_{12}}\right)^{\frac{1}{2}} = \left(\frac{\mathcal{M}_{12}^*}{\mathcal{M}_{12}}\right)^{\frac{1}{2}} \tag{1.88}$$

so that

$$\frac{q}{p} = \frac{V_{tb}^* V_{td}}{V_{tb} V_{td}^*}. \tag{1.89}$$

An example of a decay through which the angle β can be measured is $B^0 \to J/\psi K_S^0$.

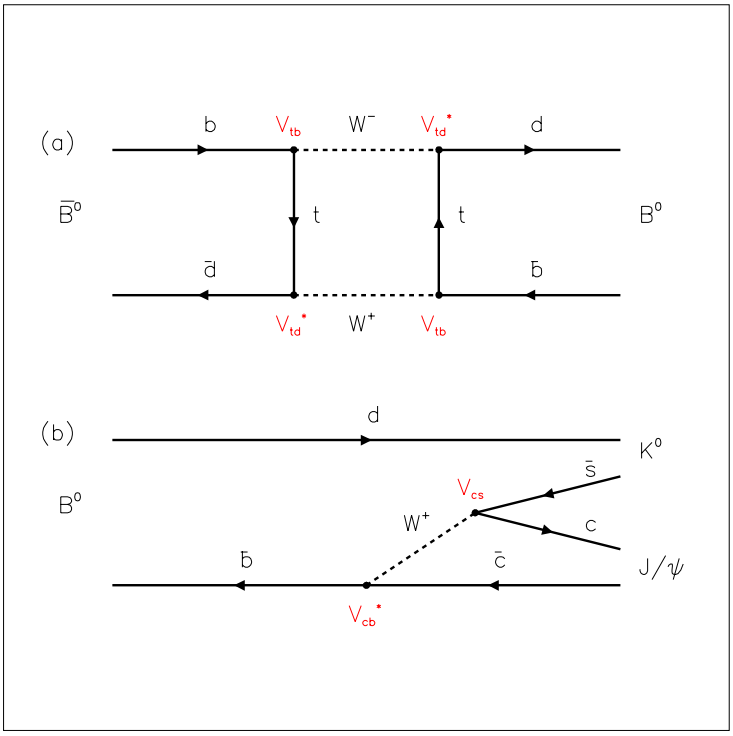

Figure 1.2: *Feynmann diagrams for (a) neutral B meson mixing and (b) a typical tree-level decay.*

Here, there is an extra contribution to λ to account for the K^0 mixing:

$$\lambda = \left(\frac{q}{p}\right)\left(\frac{\overline{A}}{A}\right)\left(\frac{q}{p}\right)_K . \tag{1.90}$$

The decay part is given by tree level processes such as figure 1.2(b):

$$\frac{\overline{A}}{A} = \frac{V_{cb}V_{cs}^*}{V_{cb}^*V_{cs}} \tag{1.91}$$

and the full expression is

$$\lambda(B^0 \to J/\psi K_S) = \left(\frac{V_{tb}^*V_{td}}{V_{tb}V_{td}^*}\right)\left(\frac{V_{cb}V_{cs}^*}{V_{cb}^*V_{cs}}\right)\left(\frac{V_{cs}V_{cd}^*}{V_{cs}^*V_{cd}}\right) \tag{1.92}$$

which gives

$$\Im(\lambda) = -\sin(2\beta). \tag{1.93}$$

This quantity can be measured as shown in equation 1.46.

An example of measuring the angle α is through the decay $B^0 \to \pi^+\pi^-$. In this case the expression for λ is

$$\begin{aligned} \lambda(B^0 \to \pi^+\pi^-) &= \left(\frac{V_{tb}^* V_{td}}{V_{tb} V_{td}^*}\right)\left(\frac{V_{ub} V_{ud}^*}{V_{ub}^* V_{ud}}\right) \\ \Rightarrow \Im(\lambda) &= \sin(2(\pi - \beta - \gamma)) \\ &= \sin(2\alpha). \end{aligned} \tag{1.94}$$

The angle γ could be measured in $B_s^0 \to \rho K_S^0$ decays. This brings in the extra term for kaon mixing again and so

$$\begin{aligned} \lambda(B_s^0 \to \rho K_S) &= \left(\frac{V_{tb}^* V_{ts}}{V_{tb} V_{ts}^*}\right)\left(\frac{V_{ub} V_{ud}^*}{V_{ub}^* V_{ud}}\right)\left(\frac{V_{cs} V_{cd}^*}{V_{cs}^* V_{cd}}\right) \\ \Rightarrow \Im(\lambda) &= -\sin(2\gamma). \end{aligned} \tag{1.95}$$

Most B decay channels have contributions from both tree and penguin diagrams. There are gluonic penguins as in figure 1.3(a) and also electroweak penguins as in figure 1.3(b). In the latter a Z boson or a photon can be radiated from either the top quark or the W. A significant contribution from both tree and penguin processes in a decay tends to inhibit the clean extraction of CP information due to the presence of different weak and strong phases. Having different strong phases is often useful for measuring direct CP violation but with different weak phases, the 'penguin pollution' must be removed if a CKM angle is to be measured cleanly. The amplitude A for a general quark process $b \to q\overline{q}q'$ can be written

$$A_{q\overline{q}q'} = V_{tb} V_{tq'}^* P_{q'}^t + V_{cb} V_{cq'}^* (T_{c\overline{c}q'} \delta_{qc} + P_{q'}^c) + V_{ub} V_{uq'}^* (T_{u\overline{u}q'} \delta_{qu} + P_{q'}^u) \tag{1.96}$$

where P and T denote contributions from penguin and tree diagrams respectively. For each q and q' it is convenient to use a unitarity relation from equations 1.85 in order to eliminate one of the three terms. Thus for $b \to c\overline{c}s$ decays such as $B^0 \to J/\psi K_S^0$,

$$A(c\overline{c}s) = V_{cb} V_{cs}^* (T_{c\overline{c}s} + P_s^c - P_s^t) + V_{ub} V_{us}^* (P_s^u - P_s^t). \tag{1.97}$$

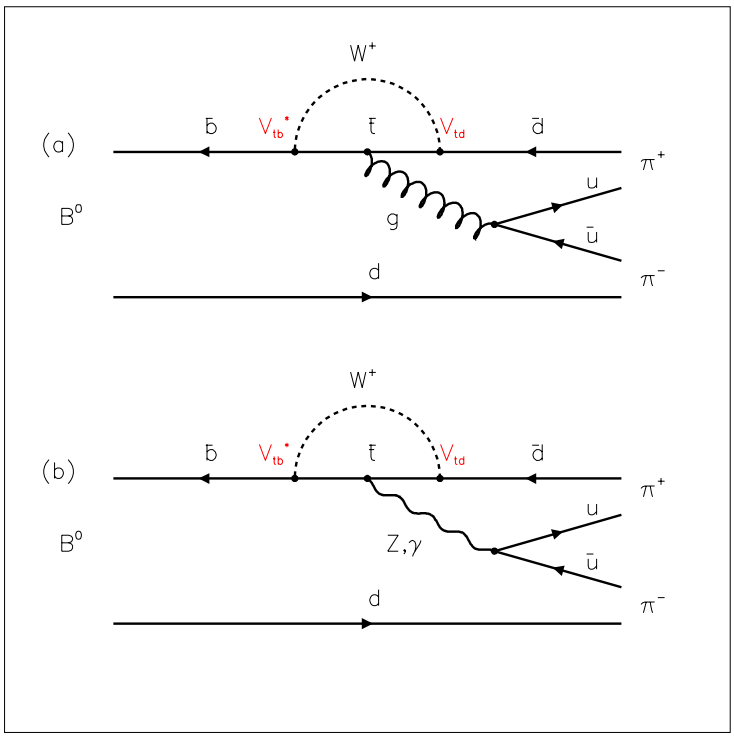

Figure 1.3: *Examples of penguin processes: Figure (a) is a QCD penguin. Figure (b) is an electroweak penguin. Alternatively, the Z or γ can couple to the W.*

In this decay, $V_{cb}V_{cs}^* \gg V_{ub}V_{us}^*$ and the second term can be neglected. This means that both tree and penguin contributions have the same weak phase and therefore these modes allow a clean measurement of the angle β.

For $b \to u\overline{u}d$ decays such as $B^0 \to \pi^+\pi^-$,

$$A(u\overline{u}d) = V_{tb}V_{td}^*(P_d^t - P_d^c) + V_{ub}V_{ud}^*(T_{u\overline{u}d} + P_d^u - P_d^c). \tag{1.98}$$

The two terms in this expression are similar in magnitude implying possible significant penguin pollution for these decay modes. In this case it is necessary to separate the two contributions via an isospin analysis [19] before obtaining a clean measurement of the angle α.

1.7.3 Scalar to Vector-Vector Decays

Another type of complication for the measurement of unitarity triangle angles is present in the decay of a B to a pair of vector mesons. In this case the spins of the two mesons can add up to give an overall spin of 0,1 or 2. Since total angular momentum must be conserved in the decay and the B is spinless, the final state can have an orbital angular momentum of L=0,1 or 2. The partial wave which is present contributes to the *CP* value of the final state by $(-1)^L$ and so the final state is not a pure *CP* state but is some admixture of *CP* even and *CP* odd.

An example is $B^0 \to J/\psi K^{*0}$. This is not actually a *CP* eigenstate so in practice one requires that $K^{*0} \to K^0_S\pi^0$ as well. The three final state particles have an overall intrinsic *CP* value of +1. This comes from the product of their individual *CP* values and an extra $(-1)^1$ from the fact that the K^{*0} has decayed. We now see that S- and D-wave contributions (L=0 and 2) give a final state which is overall *CP* even and the P-wave contribution (L=1) gives a final state which is overall *CP* odd. The two *CP* states have different signs in the decay amplitude and so equation 1.46 now has an extra factor:

$$a_{f_{CP}}(t) = D \sin 2\beta \sin(\Delta m_B t) \tag{1.99}$$

were D is the 'dilution factor' and is given by

$$D = \frac{\Gamma_+ - \Gamma_-}{\Gamma_{tot}}. \tag{1.100}$$

Here Γ_+, Γ_- and Γ_{tot} are partial widths based on the *CP* eigenvalue of the final state. It turns out that the states of definite *CP* can be separated by an angular analysis (see chapter 5). This adds complication to the experimental analysis but once this has been done, these modes are as clean, theoretically, as the vector-pseudoscalar final states.

1.8 Status of CKM Parameters

The aim of this section is to show the current constraints on the parameters of the CKM matrix as determined from experiment. One of the parameters, $\lambda = |V_{us}|$, is known to an accuracy of 1% and is considered fixed in what follows. The other three are somewhat more poorly known and can be written as the Wolfenstein parameters $(A, \overline{\rho}, \overline{\eta})$. The $\overline{\rho}$ and $\overline{\eta}$ are from the extended Wolfenstein parameterization, which includes terms up to $\mathcal{O}(\lambda^6)$ corrections. In terms of the original ρ and η they are

$$\overline{\rho} = \rho(1 - \lambda^2/2), \quad \overline{\eta} = \eta(1 - \lambda^2/2). \tag{1.101}$$

The determination of CKM parameters involves significant theoretical uncertainties when interpreting the experimental measurements. Since the A parameter is better determined than the other two, it is useful to show the CKM constraints in the $(\overline{\rho}, \overline{\eta})$ plane, which represents the position of the apex of the Unitarity Triangle. The sides of the triangle are given by

$$R_u = \frac{1 - \lambda^2/2}{\lambda} \left| \frac{V_{ub}}{V_{cb}} \right|, \quad R_t = \frac{1}{\lambda} \left| \frac{V_{td}}{V_{cb}} \right|. \tag{1.102}$$

and λ is known to be 0.2196 ± 0.0023 from $K \to \pi l \nu$ decays [5]. Thus, measurement of $|V_{ub}/V_{cb}|$ places a constraint on the length of one of the sides of the unitarity triangle. The matrix element $|V_{cb}|$ can be measured in the exclusive semileptonic decay mode $\overline{B} \to D^* l \overline{\nu}$ or from inclusive semileptonic B decays. The CLEO collaboration has measured $|V_{ub}|$ in $\overline{B} \to \rho l \overline{\nu}$ and $\overline{B} \to \pi l \overline{\nu}$ decays [20]. An endpoint analysis in inclusive semileptonic B decays yields a model-dependent determination of $|V_{ub}/V_{cb}|$. The current values are [5]

$$\begin{aligned} |V_{cb}| &= 0.0395 \pm 0.0017 \\ |V_{ub}| &= 3.3 \pm 0.4 \pm 0.7 \\ |V_{ub}/V_{cb}| &= 0.08 \pm 0.02 \end{aligned}$$

where the first error on $|V_{ub}|$ is experimental and the second is from model uncertainties.

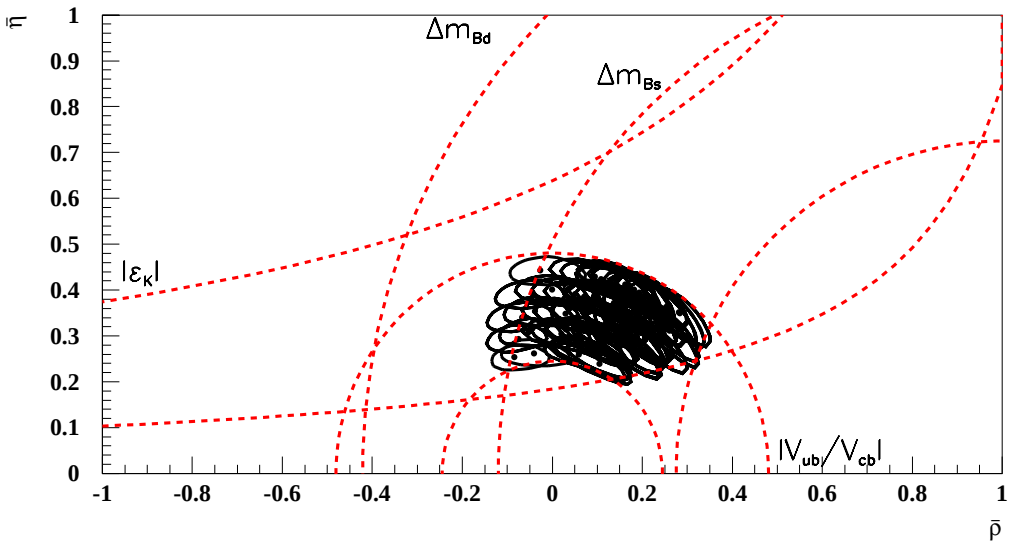

Figure 1.4: *The currently allowed region for the position of the apex of the Unitarity Triangle. Each contour centred with a dot represents the 95% confidence level for a fixed set of theoretical parameters. The individual constraints from different measurements are shown as dotted lines.*

Analysis of $B_d - \overline{B}_d$ mixing yields a value for $|V_{td}V_{tb}^*|$ because of the dominance of the top quark in the box diagram. This in turn constrains the length R_t of the Unitarity Triangle. The oscillation frequency for the mixing is given by the difference in mass of the heavy and light B_d states:

$$\Delta m_{B_d} \propto \eta_B f_{B_d}^2 B_{B_d} |V_{td}V_{tb}^*|^2, \tag{1.103}$$

where η_B is a QCD correction factor, f_{B_d} is the B decay constant and B_{B_d} is a "bag factor" which parameterizes the value of the hadronic matrix element. The main impediment here is that $f_{B_d}\sqrt{B_{B_d}}$ has not been measured experimentally and has a theoretical uncertainty of 20% [21]. The measurement of ϵ_K also limits the range of possible values for $\overline{\rho}$ and $\overline{\eta}$. Finally, there is a lower limit on the rate of B_s mixing, $\Delta m_{B_s} > 12.4ps^{-1}$ [21], which can be plotted together with the other three constraints in the $(\overline{\rho}, \overline{\eta})$ plane. This is shown in figure 1.4. It is expected that results from the BaBar experiment will considerably reduce the size of the allowed

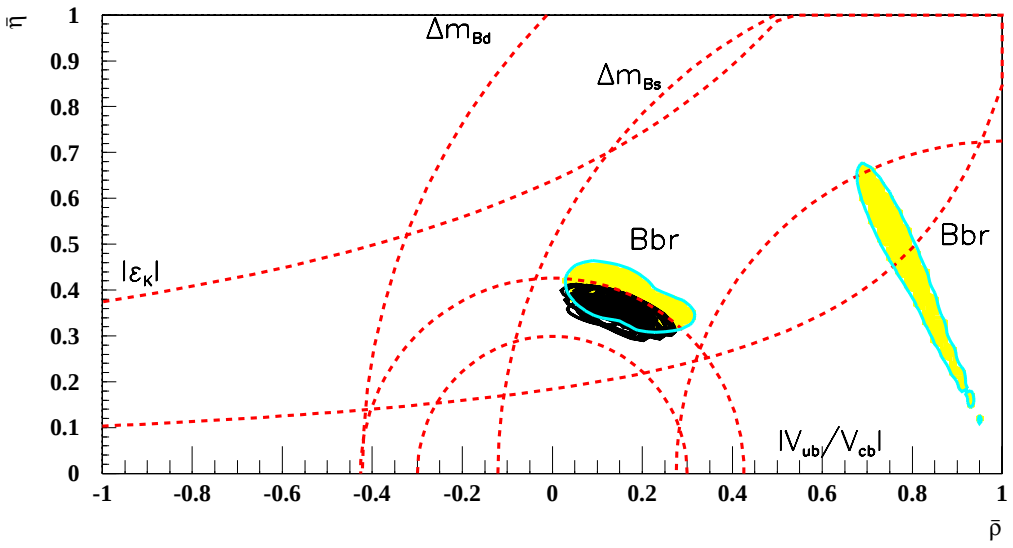

Figure 1.5: *The $(\overline{\rho},\overline{\eta})$ plane after combining all measurements from $180\,fb^{-1}$ of BABAR data at the $\Upsilon(4S)$. Each contour centred with a dot represents the 95% confidence level for a fixed set of theoretical parameters. The full (lightly shaded) contours represent the 95% CL of the BABAR CP measurements alone.*

region such that with an integrated luminosity of $180\,fb^{-1}$ the $(\overline{\rho},\overline{\eta})$ plane will look like that shown in figure 1.5.

Chapter 2

The BaBar Experiment

2.1 Introduction

The physics to be studied with the BABAR experiment requires a high performance detector and collider. The CP asymmetries to be measured may be quite large requiring only a few hundred events in the appropriate channel to observe. However the exclusive B meson final states of interest have very small branching ratios, *e.g.*, $\sim 10^{-5}$ for $J/\psi K^0_S$, so the collider must produce in excess of 10^7 $B^0\overline{B}^0$ pairs. This requires a luminosity of a few $\times 10^{33}\,\mathrm{cm}^{-2}\mathrm{s}^{-1}$ and should allow the asymmetries to be measured with errors at the 10% level or better.

The main CP asymmetry measurements are made using events in which one B, usually decaying to a CP eigenstate, is fully reconstructed and the other B is tagged as a B^0 or $\overline{B}^0$ using a lepton or charged kaon. Reconstruction of the CP mode involves detection of between two and six charged tracks and often one or more $\pi^0 s$. This places constraints on the performance of the detector. The tracking must provide accurate measurements of charged particle momenta and there must be a high resolution electromagnetic calorimeter. Good particle identification is important both for B-flavour tagging and distinguishing between different final states. In order to

measure the positions of the B meson decay points, excellent vertex resolution is a necessity.

2.2 The PEP-II Asymmetric Collider

Perhaps the best environment in which to study CP violation in the B meson system is that provided by an asymmetric e^+e^- collider operating at the $\Upsilon(4S)$ resonance. The low Q-value of the $\Upsilon(4S)) \rightarrow B\overline{B}$ decay means that if such a collider had beams of equal energy, the B mesons would be produced almost at rest. The asymmetry produces a moving center-of-mass system in the laboratory frame which allows the B meson decay lengths to be measured.

2.2.1 BaBar Versus Other Experiments

The e^+e^- environment has several advantages over the hadronic environment when it comes to studying this type of physics [22]. There is a high signal-to-background ratio with $\sigma_{b\overline{b}}/\sigma_{TOT} \simeq 0.28$ and the events are clean, with a charged track multiplicity of ~ 11. This relatively low level of background also means that there is an increased ability to reconstruct final states which contain π^0s and photons, allowing measurements to be made in many more channels. The interaction rate is low with physics events being produced at ~ 10Hz. Finally, the extrapolation of results from existing experiments to BaBar is more straightforward in this environment.

There are also advantages for BaBar over e^+e^- experiments operating at a higher energy, such as those at LEP. Firstly, the B mesons are produced in coherent pairs with no fragmentation products which reduces the effect of combinatorial backgrounds. Secondly there are precisely known kinematical constraints such as the four-momentum of the $B\overline{B}$ system and the momentum magnitudes of the B mesons individually in the center-of-mass frame. These constraints make a significant

contribution to the suppression of backgrounds.

2.2.2 PEP-II Description and Cross-Sections

To produce an asymmetric collision, PEP-II uses two rings. One (the High Energy Ring or HER) contains electrons at 9 GeV and the other (the Low Energy Ring or LER) contains positrons at 3.1 GeV. This produces a boost in the laboratory frame for the resulting B mesons of $\beta\gamma = 0.56$. The electrons and positrons are injected into the machine from the SLAC linac. The design luminosity goal is $3 \times 10^{33}\,\mathrm{cm}^{-2}\mathrm{s}^{-1}$.

The cross-sections for the production of fermion pairs at the $\Upsilon(4S)$ are shown in Table 2.1 [22]. The numbers are effective cross-sections, taking into account the experimental acceptance. All of the quark-antiquark cross-sections except for $b\overline{b}$ are calculated with the `Jetset7.4` event generator [23] and include radiative corrections. The $b\overline{b}$ cross-section is taken from the peak value obtained in CLEO with an adjustment for the slightly larger beam spread expected in BABAR. The uncertainty on this value is less than 0.1 nb.

2.2.3 The Interaction Region

The high luminosity and asymmetry of the PEP-II machine have resulted in an unconventional design for the interaction region. In order to achieve currents of the required magnitude, the beam is divided into a large number of low charge bunches to minimize beam-beam interference effects. For the same reason the beams must collide only at the interaction point(IP). Thus the beams must be brought together just before the IP and separated again before the next collision would occur at 62cm from the IP. This is achieved by utilizing the energy asymmetry and the separation dipoles(B1) at 20cm from the IP to displace the beams horizontally. The layout

Table 2.1: *Production cross-sections at* $\sqrt{s} = M(\Upsilon(4S))$.

$e^+e^- \rightarrow$	Cross-section (nb)
$b\overline{b}$	1.05
$c\overline{c}$	1.30
$s\overline{s}$	0.35
$u\overline{u}$	1.39
$d\overline{d}$	0.35
$\tau^+\tau^-$	0.94
$\mu^+\mu^-$	1.16
e^+e^-	~ 40

of the interaction region is shown in figure 2.1 [24]. Strong focusing of the beams requires quadrupoles near to the IP. The final quadrupole is Q1 which is common to both beams and starts at 90cm from the IP. The next quadrupole Q2 focuses only the low-energy beam(LEB) and the following pair of quadrupoles, Q4 and Q5, focus only the high-energy beam(HEB). The B1 magnets are within the BABAR detector volume. This placed constraints on the design of the detector as will be discussed later in this chapter. The Q1 magnets also enter the detector volume, although only partially.

A final point worthy of note here is that the detector axis is not exactly coincident with the beam collision axis. In fact the detector is rotated by 20 mr relative to the beam direction, around a vertical axis. The reason for this is to reduce the orbit distortion effects caused by the angle between the outgoing beams and the detector's solenoidal magnetic field.

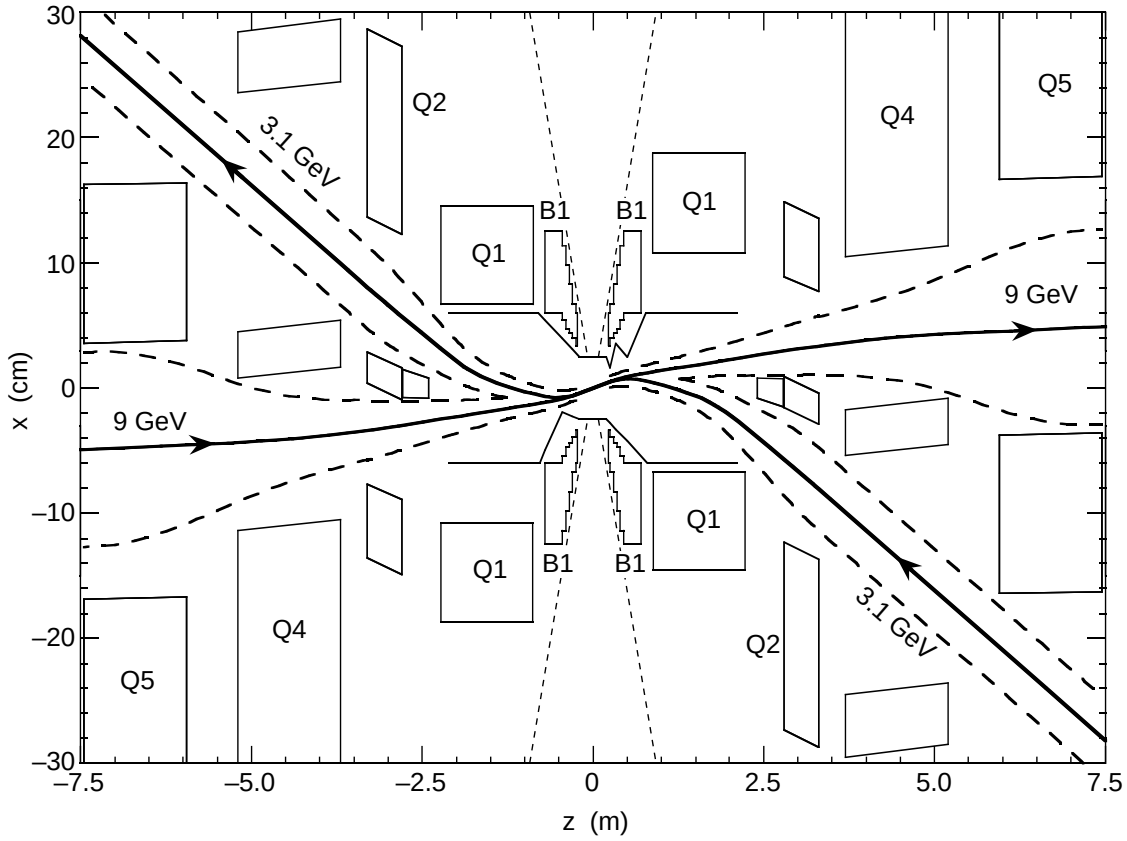

Figure 2.1: *A plan view of the interaction region. The vertical scale is exaggerated. The dashed lines indicate the beam stay-clear envelopes and the detector acceptance cutoff at 300mr.*

2.2.4 Machine Backgrounds

The novel design of the interaction region for PEP-II means that machine backgrounds are a potential problem. The bending of the beams near the IP produces levels of synchrotron radiation not present in more conventional e^+e^- colliders. This bending can also send off-energy beam particles into the detector. The challenge is to achieve background rates similar to those of existing colliders at an order of magnitude higher beam current. The three main sources of background for the detector have been identified [25] as synchrotron radiation, lost beam particles due to

bremsstrahlung with residual gas molecules and lost beam particles due to Coulomb scattering off residual gas molecules. If the background is too high, the detector can suffer from excessive occupancy and/or radiation damage.

2.2.4.1 Synchrotron Radiation

The dominant source of synchrotron radiation is that generated by a beam passing through a bending magnet or an offset quadrupole and is called *fan radiation*. The interaction region optics are designed to minimize the amount of radiation incident on the detector from this source. In particular, the S-bend geometry of the beam lines causes most of the synchrotron radiation from magnets upstream of the interaction region to pass cleanly through the detector region. In addition there are masks to prevent various sources of synchrotron radiation from shining directly on to the IP beam pipe. The synchrotron radiation fans and masks are shown in figure 2.2. Studies show [26] that the occupancy and radiation damage should be at $\sim 1/80$ of their allowed limits.

2.2.4.2 Lost Particles

Beam particles can bremsstrahlung or Coulomb scatter off residual gas molecules in the beam pipe. This can cause high energy electrons and photons to strike the beam pipe wall or radiation masks near the IP and the resulting electromagnetic showers can lead to excessive detector occupancy and/or radiation damage. The beam-gas interactions are simulated using DECAY TURTLE [27]. These "lost particles" are then put through a full GEANT [28] simulation of the interaction region and detector to assess the impact on the various detector components. Table 2.2 shows expected occupancy levels and radiation doses for lost beam particle backgrounds in the two innermost subdetectors of the BABAR experiment.

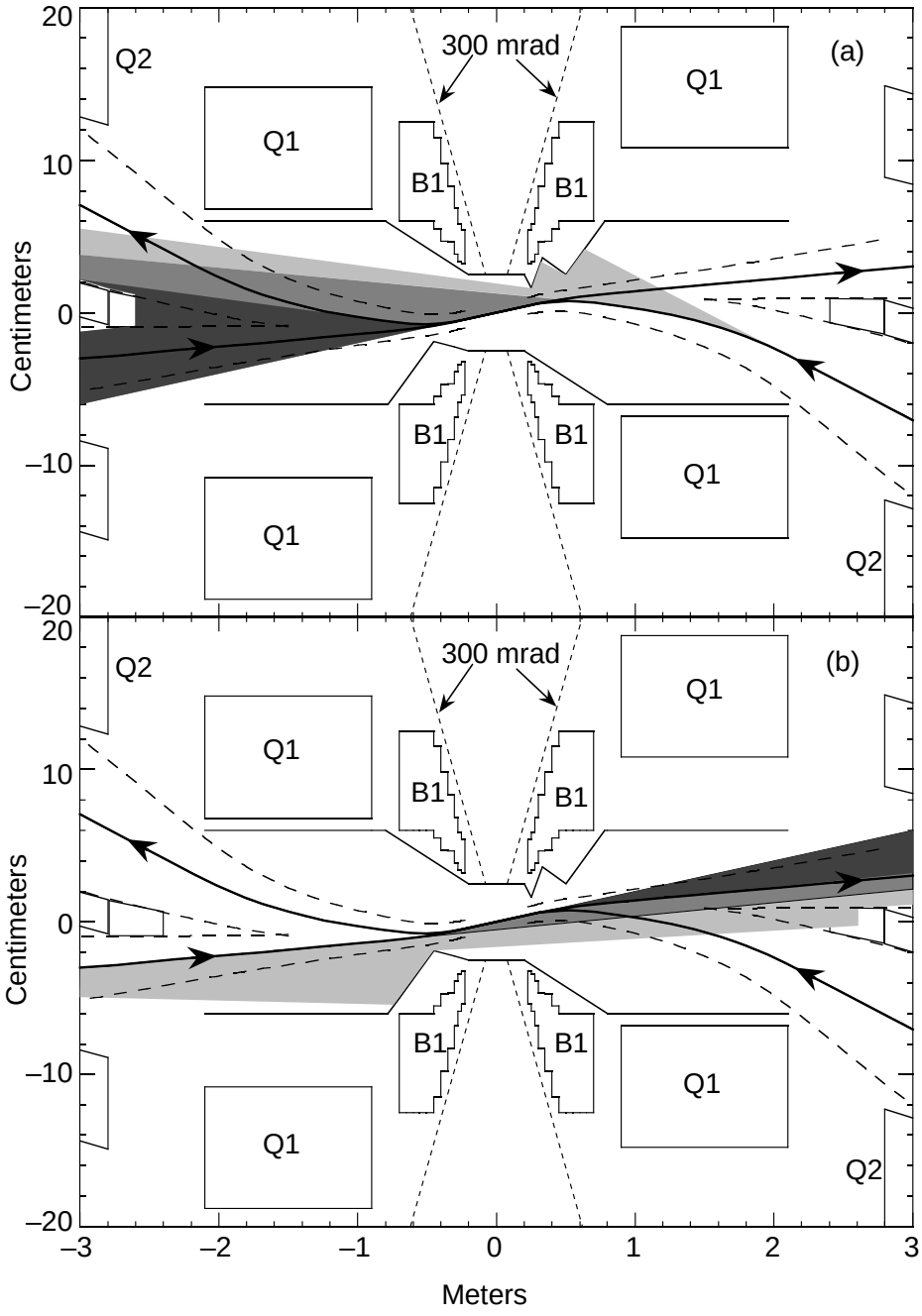

Figure 2.2: *Synchrotron radiation fans from the LEB(top) and HEB(bottom). The density of shading indicates the relative photon intensity from the various radiation fans. The masks located near the IP which are used to shield the detector are also shown.*

Table 2.2: *Occupancy levels and radiation doses from lost beam particle backgrounds in the tracking system of the BABAR experiment.*

	Silicon Tracker		Drift Chamber	
	Average	First layer	Average	First layer
Occupancy	1.3%	3.0%	0.05%	0.5%
Limit	20%	20%	10%	10%
Rad. dose (yr)	33 krad	82 krad	4×10^{-4} C/cm	4.5×10^{-3} C/cm
Limit	1500 krad	1500 krad	0.1 C/cm	0.1 C/cm

2.3 The BaBar Detector

In order to measure *CP* asymmetries in many different B meson decay modes the BABAR detector must meet certain criteria. In general there should be the maximum possible acceptance in the center-of-mass system. The asymmetric beam energies cause the decay products to be boosted forward in the laboratory frame. The detector is necessarily asymmetric to account for this effect as well as possible. Also, the high luminosity of PEP-II requires there to be machine components very close to the interaction region(as described in section 2.2.3) and these have to be accommodated in the design of the detector.

More specifically, individual sections of the detector have their own requirements geared towards achieving the best possible physics performance. The vertex resolution must be excellent since the difference in decay time of the two B mesons is measured in terms of the difference in the z-components of their decay positions. High quality vertexing is also an important factor in discriminating between beauty, charm and light-quark vertices. A related requirement here is the need to minimize multiple scattering. It should be possible to track charged particles over the range ~ 60 MeV $< p_t <\sim 4$ GeV. There must be particle identification capabilities allow-

ing discrimination between e, μ, π, K and p over a wide kinematic range. Flavour tagging of B mesons with a high efficiency and purity is only possible with good e, μ and K identification. In addition, π-K separation at around 2-4 GeV is necessary in order to distinguish between final states such as $B^0 \to \pi^+\pi^-$ and $B^0 \to K^\pm\pi^\mp$. There is a need for photon and π^0 detection over the range ~ 20 MeV $< E <\sim 5$ GeV since final states often contain one or more π^0s. Finally, the detector should have the ability to identify neutral hadrons. This is important for reconstructing channels such as $B^0 \to J/\psi K^0_L$.

2.3.1 Detector Overview

The BABAR detector was designed and constructed in such a way as to fulfill all the above requirements. A cutaway picture of the detector is shown in figure 2.3. The main subsystems are:

1. The Silicon Vertex Tracker (SVT) provides very accurate position information for charged tracks. In addition it is the only tracking device for charged particles with very low transverse momentum.

2. The Drift Chamber (DCH) has a helium based gas mixture in order to try to minimize multiple scattering. It provides the main momentum measurement for charged particles and also contributes particle identification information through $\mathrm{d}E/\mathrm{d}x$.

3. The Detector of Internally Reflected Cherenkov light (DIRC) is optimized for charged hadron particle identification.

4. The Electromagnetic Calorimeter (EMC) which consists of Caesium Iodide crystals. It has a forward endcap to account for the laboratory frame boost that the B decay products experience. In addition to detecting neutral elec-

tromagnetic particles it provides electron identification and information for neutral hadron identification.

5. A superconducting solenoid which produces a 1.5T magnetic field.

6. The Instrumented Flux Return (IFR) which provides muon and neutral hadron identification.

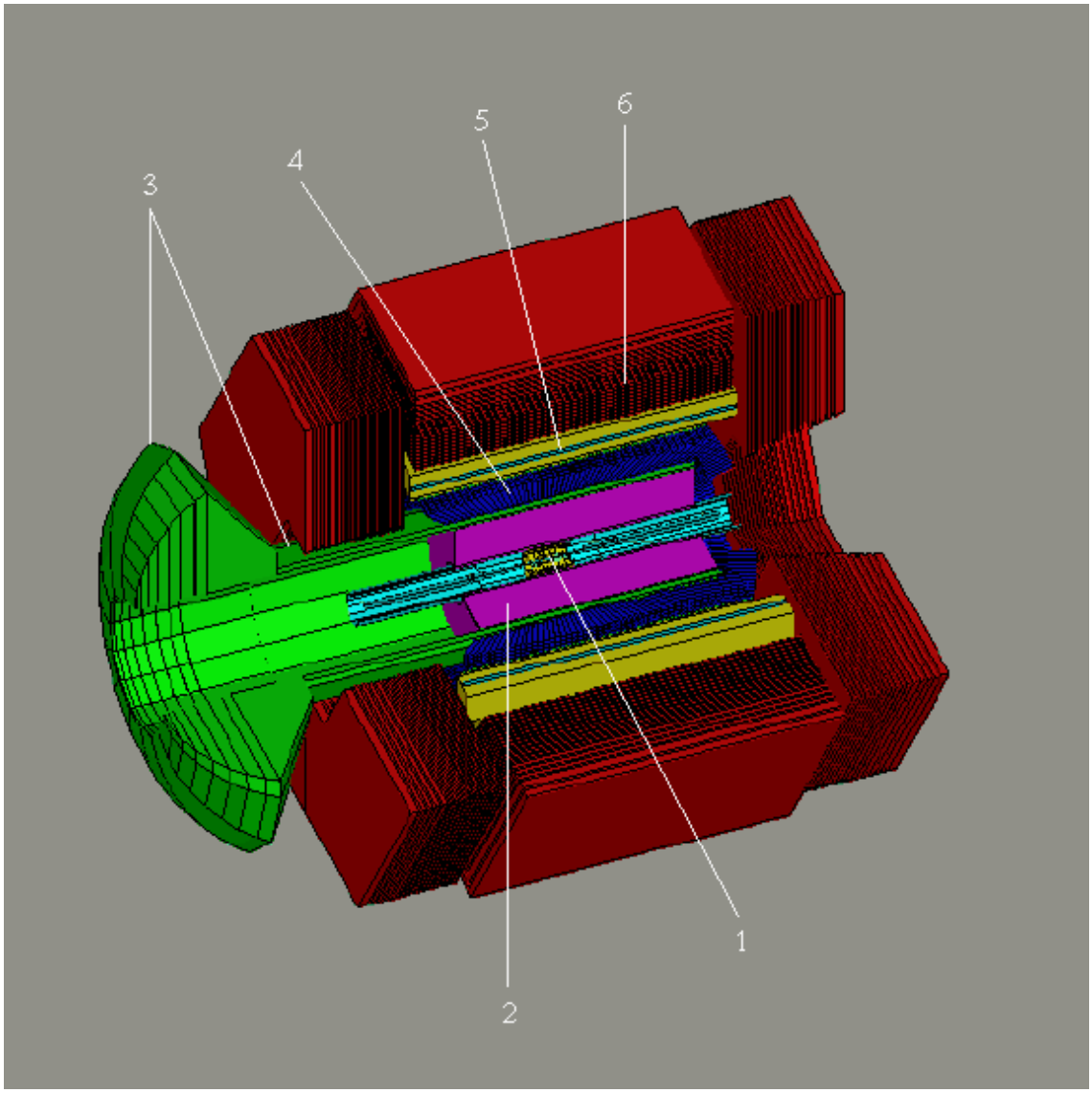

Figure 2.3: *Layout of the BABAR detector. See text for key.*

The next few sections will describe in detail the individual detector components. Some more general design parameters of the BABAR detector are shown in table 2.3.

Table 2.3: *Detector design performance parameters. Acceptance coverages are quoted for the Center of Mass system.*

Parameter	Value [24]
Tracking coverage ($/4\pi$)	0.92
σ_{p_t}/p_t (%) (1 GeV pions at 90°)	0.36
σ_{z_0} (μm) (1 GeV pions at 90°)	52
Calorimetry coverage ($/4\pi$)	0.90
X_0 in front of Calorimeter (at 90°)	0.25
σ_E/E (%) (1 GeV γ at all angles)	1.8
γ efficiency within acceptance (at 100 MeV)	0.92
Charged Hadron ID coverage ($/4\pi$)	0.84

2.3.2 The Silicon Vertex Tracker

The main aim of the BABAR vertex detector is to reconstruct the B meson decay vertices so that the time difference between them can be measured. This in turn allows a measurement of CP violation to be made. The innermost points on a track, which are measured by the SVT, will always provide the most accurate angular information since the outer points are limited by multiple scattering. In addition, the SVT is solely responsible for tracking charged particles with $p_{\rm t} < 100$ MeV/c.

At PEP-II the mean value of the separation of the B vertices is $\sim 250\,\mu$m. Studies show [29] that the required resolution on this value should be better than 50%. This corresponds to a single vertex resolution of better than $80\,\mu$m, which is well within the capabilities of modern silicon microstrip detectors. Ultimately, multiple

scattering sets the limit on point resolution for the SVT. The inner layers achieve 10-15 μm and the outer layers 30-40 μm. Also, the SVT needs to cover the largest possible solid angle for acceptance. Limitations on this are set by the B1 magnets and the various support structures and electronics. The polar angle coverage is from 20.1° to 150.2°.

The SVT has 5 layers of silicon microstrip detectors. The inner two layers are the most important for impact parameter measurements since they are the closest to the interaction point. They should have good point resolution and a high efficiency. The outer two layers are useful for alignment with tracks detected in the drift chamber. The middle layer gives extra tracking information, particularly for charged particles that do not reach the drift chamber. A study was made to determine how best to optimize the resolution of the different layers and can be found in [30].

2.3.2.1 Detector Layout

The SVT consists of five concentric cylindrical layers of double-sided silicon detectors as shown in figures 2.4 and 2.5. Each layer is divided around the azimuth angle into modules. The inner three layers have six modules each, in a barrel arrangement. The outer two layers have 16 and 18 modules respectively and form an arch structure. This feature increases the solid angle coverage and avoids large track incidence angles. Each module is divided into forward and backward half-modules which are kept electrically isolated from one another. Half-modules contain between two and four detectors. The inner sides of the detectors have strips which are oriented perpendicular to the beam direction to measure the z coordinate. The outer sides have strips orthogonal to the z strips to measure the ϕ coordinate. In total there are 340 silicon detectors covering an area of $\sim 1\,\mathrm{m}^2$ and about 150,000 readout channels. The parameters of each layer are shown in table 2.4.

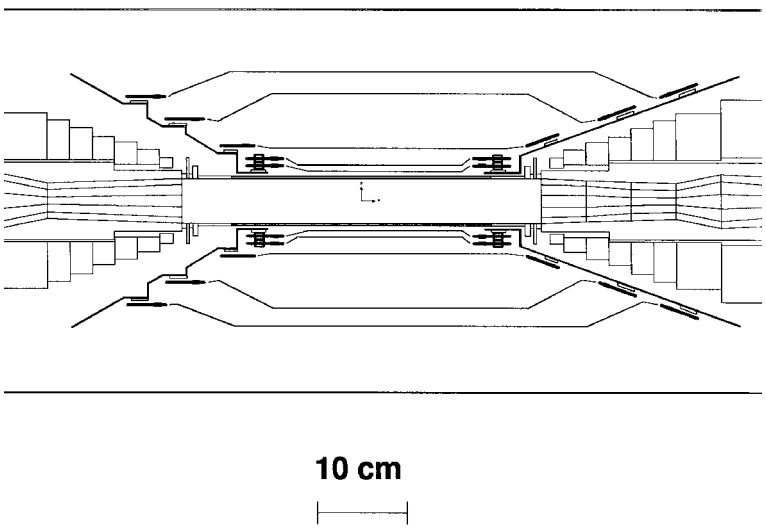

Figure 2.4: *A cross-sectional view of the BABAR silicon vertex tracker in a plane containing the beam axis.*

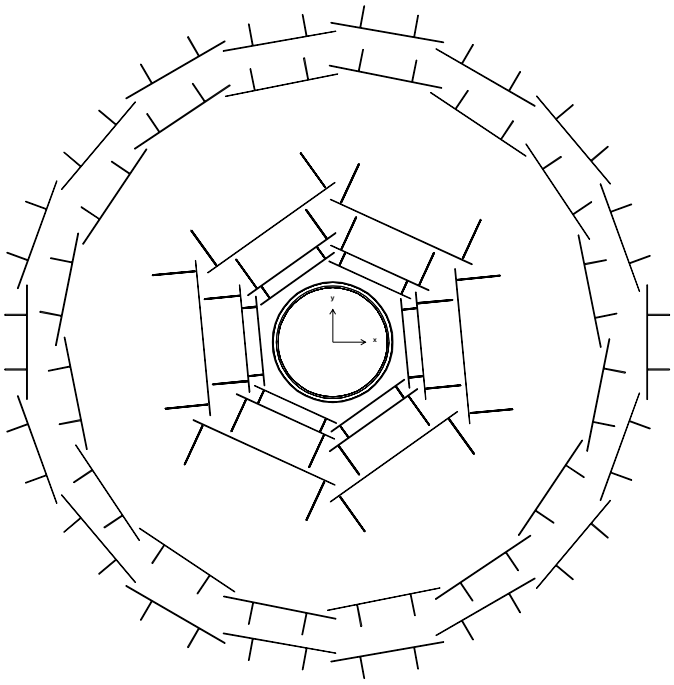

Figure 2.5: *A cross-sectional view of the BABAR silicon vertex tracker in the plane orthogonal to the beam axis.*

Table 2.4: *Some parameters of the silicon vertex tracker layout*

Layer	1	2	3	4a	4b	5a	5b
Radius (mm)	32	40	54	124	127	140	144
Modules/Layer	6	6	6	8	8	9	9
Wafers/Module	4	4	6	7	7	8	8
Readout pitch (μm)							
ϕ	50	55	55	80–100		80–100	
z	100	100	100	210		210	
Intrinsic Resol.(μm)							
ϕ	10	10	10	10–12		10–12	
z	12	12	12	25		25	

2.3.2.2 Readout

The signals from the strips are amplified and shaped before being compared with a threshold. The time which a signal spends over the threshold is approximately logarithmically related to the charge induced on the strip. The advantage of this "time over threshold"(TOT) method is a compression of the dynamic range due to the logarithm relationship. This reduces the number of bits needed to record the information which in turn reduces space and cost requirements of the front-end electronics.

2.3.3 The Drift Chamber

The BABAR drift chamber is the main tracking device of the detector. It has a high efficiency for charged tracks with a transverse momentum of greater than 100 MeV/c. It provides a spatial resolution of better than 140 μm and a dE/dx measurement

with a resolution of 7%. For tracks with $p_t > 1$ GeV/c the momentum resolution is $\sigma_{p_t} \approx 0.3\% \times p_t$. The angular acceptance of the chamber should go right down to the machine components at 300 mr. In addition the DCH serves as one of the principle triggers for the experiment.

Since the material in the DCH affects the performance of the DIRC and the electromagnetic calorimeter, it was built using lightweight materials and uses a helium based gas mixture. The readout electronics are mounted on the rear endplate in order to reduce the amount of material in the forward region. The mechanical design of the DCH is described in the following sections. A more detailed description can be found in [31].

2.3.3.1 Detector Layout

The BABAR drift chamber is a 280 cm long cylinder with an inner radius of 23.6 cm and an outer radius of 80.9 cm. The endplates are made of aluminium with the forward endplate being half as thick as the rear one at 12 mm. The inner cylinder is 1 mm or 0.28% X_0 of beryllium and the outer cylinder consists of 2 layers of carbon fiber on a Nomex core, corresponding to 1.5% X_0. A schematic side view is shown in figure 2.6.

There are 7104 hexagonal drift cells with a typical dimension of 1.2×1.8 cm^2. They are arranged in 10 superlayers, each consisting of 4 layers. Axial(A) and stereo(U,V) superlayers alternate according to the pattern shown in figure 2.7. The angle of the stereo wires varies from 40 mr in the innermost stereo superlayer to 70 mr in the outermost stereo superlayer.

The sense wires are 20 μm gold-plated tungsten-rhenium and carry 1960 V. The field wires are 120 μm and 80 μm gold-plated aluminium. The field-shaping wires at the boundaries of the superlayers carry 340 V and the other field wires are connected to ground. The gas mixture is helium-isobutane (80%:20%) and is chosen to provide

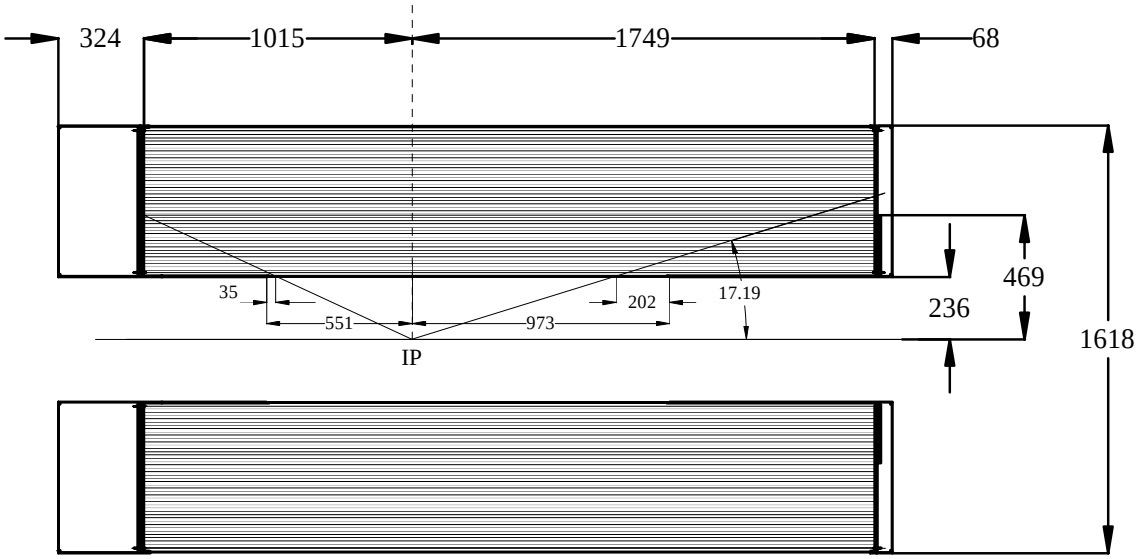

Figure 2.6: *A side view of the BABAR drift chamber. The offset in z with respect to the IP is to take account of the collision asymmetry. All dimensions are in mm.*

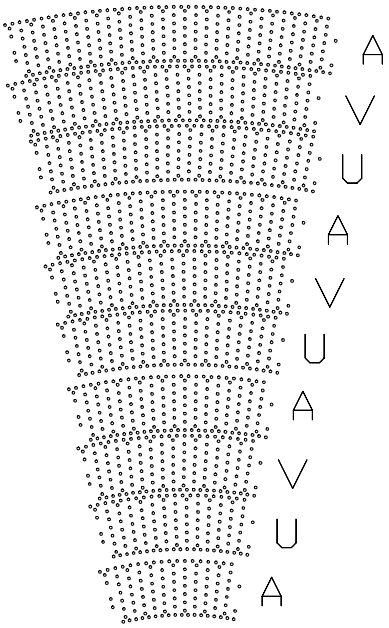

Figure 2.7: *Cell layout in the BABAR drift chamber.*

good spatial and $\mathrm{d}E/\mathrm{d}x$ resolution with a short drift time while minimizing the amount of material present. The gas and wires correspond to 0.3% X_0 for a track at 90° [32].

2.3.3.2 Electronics

The main requirement of the BABAR DCH electronics is to not degrade the performance of the chamber by more than 10%. When measuring drift-time, the electronics looks for the leading edge of the signal from the charge that arrived at the sense wire. The time is then digitized with a resolution of 1 ns. For $\mathrm{d}E/\mathrm{d}x$ measurements, the total charge in the pulse is summed.

The amplifier, digitizer and trigger interface electronics are mounted on the rear endplate of the drift chamber, in water-cooled aluminium boxes. The electronics provides trigger information by sending the data from all 7104 channels to the level 1 trigger system with a sampling frequency of 3.75 MHz. The system is designed to maintain good performance even in the presence of high backgrounds with a single-cell efficiency for the trigger signal of greater than 95%.

2.3.4 The DIRC

The DIRC, Detector for Internally Reflected Cherenkov light, is a new type of particle identification(PID) device. The PID requirements of the BABAR experiment are based around the need to tag the flavour of the non-*CP* eigenstate B meson and to distinguish between different *CP* channels. To satisfy the tagging requirement, the DIRC must provide excellent kaon identification up to momenta of about 2 GeV/c. The need to distinguish between different final states is important in rare decays used to measure the *CP* angle α. For example, it should be possible to separate the channels $B \to \pi^{\pm}\pi^{\mp}$ and $B \to K^{\pm}\pi^{\mp}$ and this needs good K/π discrimination up to

4 GeV/c. In addition it is envisaged that the DIRC will assist in muon identification in the range where the IFR is inefficient, below ~ 750 MeV/c.

The concept of the DIRC is the inverse of that for traditional ring-imaging Cherenkov counters (RICH) in that it relies on the detection of photons that are trapped in the radiator through total internal reflection [33]. This principle is shown schematically in figure 2.8. The Cherenkov radiation is emitted at a well known angle with respect to the track direction, namely $\theta_c = \cos^{-1}(1/\beta n)$ where n is the refractive index of the radiator medium [34].

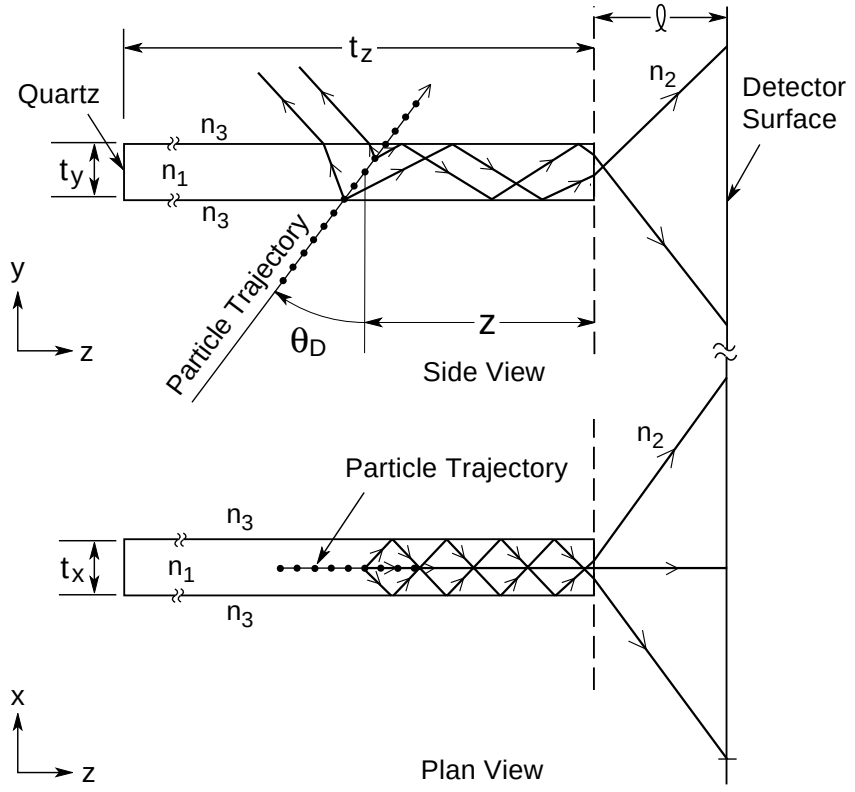

Figure 2.8: *Schematic of a single DIRC radiator bar. The particle trajectory is represented by a series of connected dots. The radiated Cherenkov photons are shown as lines with arrows.*

2.3.4.1 Detector Layout

The DIRC radiator consists of 144 bars of synthetic quartz arranged in a 12-sided polygonal barrel shape. The bars have rectangular cross section with dimensions of 1.7 cm thick by 3.5 cm wide and are 4.9 m long. The quartz extends through the magnet flux return in the backward direction in order to bring the Cherenkov light outside the tracking and magnetic field volumes. All of the readout happens at this end in order to help reduce the amount of material in the forward direction. The forward end has mirrors at the ends of the bars which reflect the light back towards the instrumented end.

The major mechanical elements of the DIRC are shown schematically in figure 2.9. It occupies only 8 cm of radial space and represents 14% of an X_0 for a particle at 90° [35]. The design aims to minimize the effect of the DIRC on the performance of the calorimeter behind it. Coverage in the polar angle in the center-of-mass frame is 87% and in the azimuthal angle it is 93%.

2.3.4.2 Readout

Before detection, the Cherenkov image is allowed to expand in a tank of purified water whose refractive index matches well that of the quartz bars (for which n=1.474). At the far end of the tank is an array of photomultiplier tubes (PMTs) lying on a surface which is approximately toroidal so as to make the photon pathlength constant at 1.2 m over a large angular range. The backward end of each bar has a small, trapezoidal piece of quartz glued to it. This allows for a reduction in the number of PMTs required by folding one half of the image onto the other half and also reflecting photons with large angles in the radial direction back into the detection array. There are about 11,000 PMTs of diameter 2.82 cm and the standoff box is filled with 6 m^3 of water.

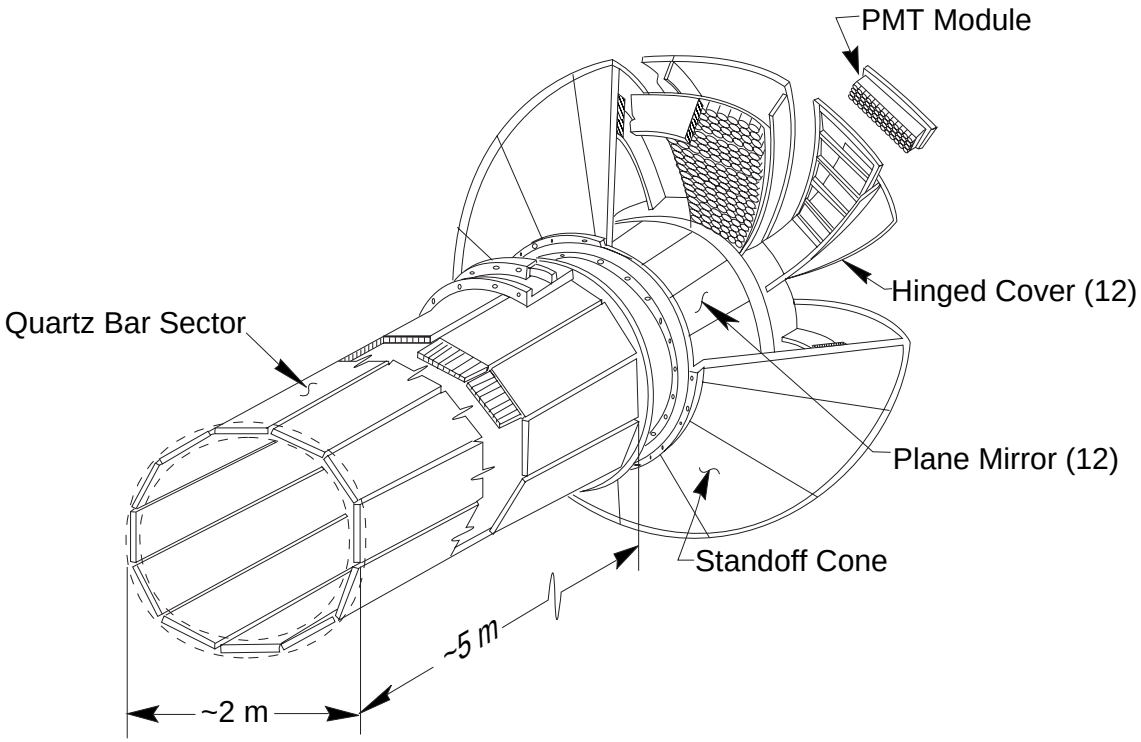

Figure 2.9: *Schematic of the dirc showing the mechanical elements. Included are the mirrors mounted inside the standoff box, used to reflect Cherenkov light towards the PMTs.*

The difference in Cherenkov angle between a pion and a kaon at 4 GeV is about 6.5 mr. This requires the Cherenkov angle of a track to be resolved to 2 mr or better in order to achieve good K/π separation. This is achievable given a single photoelectron resolution of order 9 mr and between 25 and 50 photoelectrons per track [35].

2.3.5 The Electromagnetic Calorimeter

The physics that the BABAR experiment has been designed to study requires excellent electromagnetic calorimetry. On average, generic B decays contain 5.5 photons with about half of the photon energies below 200 MeV [24]. This causes the π^0

and B reconstruction efficiencies to fall off very quickly as the minimum detectable photon energy increases. In addition many of the B decays used to study CP violation contain at least one π^0 and have characteristically small branching ratios. Thus, high efficiency for low energy photons along with good energy and angular resolution is required to accurately reconstruct these states and improve their signal-to-background ratios. The calorimeter also facilitates lepton identification by providing e/π and e/μ separation and therefore provides one of the B flavour tags required by all CP analyses.

2.3.5.1 Detector Layout

The BABAR calorimeter uses a quasi-projective arrangement of crystals made from Thallium doped Caesium Iodide covering a range of center-of-mass solid angle of $-0.916 \leq \cos\theta \leq 0.895$. The target energy resolution for photons at 90° is

$$\frac{\sigma_E}{E} = \frac{1\%}{\sqrt[4]{E(\mathrm{GeV})}} \oplus 1.2\% \tag{2.1}$$

where the constant term arises from front and rear leakage, inter-calibration errors and light collection non-uniformity.

The crystals are divided up into two main sections, the barrel and the forward endcap, as shown in figure 2.10. There are 5760 barrel crystals, arranged in 48 theta rows, each row having 120 identical crystals around phi. The crystals are grouped in 280 modules of 7 × 3 in theta and phi respectively. The length of the crystals varies from 29.76 cm (16.1 X_0) at the rear of the barrel to 32.55 cm (17.6 X_0) at the front. The coverage of the barrel is over a center-of-mass solid angle of $-0.916 \leq \cos\theta \leq 0.715$ and the inner radius is 91 cm. The endcap is a conic section with the front and back surfaces at an angle of 22.7° to the vertical. There are 820 endcap crystals arranged in 8 rings in theta and in modules so as to give a 20-fold symmetry in phi. There is a ninth ring, currently filled with lead shielding blocks, that could be instrumented with CsI(Tl) crystals to provide extra

polar angle coverage. The phi segmentation of the first three rings matches that of the barrel with 120 crystals each. The next three have 100 and the final two rings have 80 crystals each. All the endcap crystals are 32.55 cm($17.6X_0$) long except for those in the inner two rings which are shorter by $1\,X_0$ due to space limitations. The coverage of the endcap is over a center-of-mass solid angle of $0.718 \leq \cos\theta \leq 0.895$.

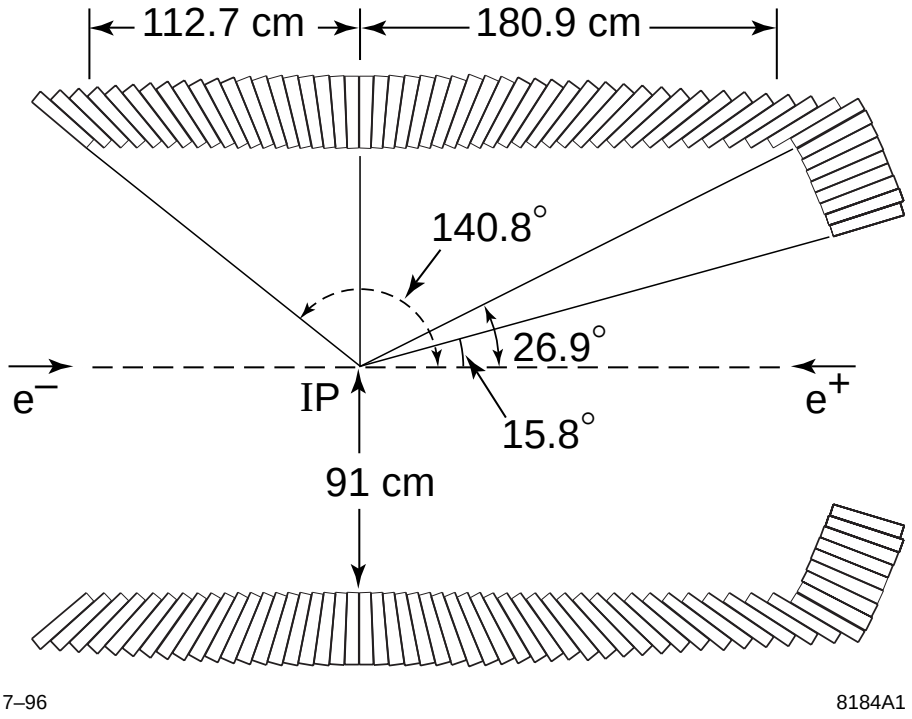

Figure 2.10: *Layout of the EMC showing the barrel and forward endcap. All dimensions are in mm.*

The crystals are trapezoidal in shape with typical dimensions of $47 \times 47\,\mathrm{mm}^2$ at the front face and $60 \times 60\,\mathrm{mm}^2$($55 \times 55\,\mathrm{mm}^2$) at the back face in the central (forward) part of the barrel.

In order to minimize the loss of particles that hit dead material between the crystals, they are arranged to be slightly non-projective in theta with respect to the interaction point. The non-projectivity is ± 15 mr for most of the barrel, increasing to 45 mr in the most-forward module. In the endcap it is 45 mr for the outer ring,

decreasing to 15 mr for the inner ring.

2.3.5.2 Readout

The scintillation light produced in each crystal is picked up by two (for redundancy) 1 cm×2 cm photodiodes glued to its back face. Their output is sent via a preamplifier circuit (which is also fixed to the back of the crystal in order to reduce pick-up noise) to an ADC board. The digital signal is then sent to a DAQ board in the experiment's electronics house. The information stored here is also sent to the level 1 trigger system. A detailed description of the calorimeter electronics can be found, for example in [36] and [37].

The average light yield per crystal is 7300 pe/MeV varying between 5000 and 10000. The incoherent electronic noise has been measured at about 900 pe or 150 keV per crystal which makes a negligible contribution to the overall energy resolution [38].

2.3.6 The Instrumented Flux Return

The outermost subdetector in BABAR consists of layers of resistive plate chambers (RPCs) which use the iron of the magnet return yoke as an absorber. It is optimized for the identification of muons and the detection of neutral hadrons. The IFR consists of a barrel section and forward and backward endcaps. The endcaps allow the solid angle coverage to go down to 300 mr in the forward direction and 400 mr in the backward direction.

2.3.6.1 Detector Layout

The graded segmentation of the iron, which varies from 2 cm to 10 cm is a novel feature of the experiment. It allows for both improved muon identification at low momenta and better K_L^0 detection. There are 18 layers of iron in the IFR giving a

total thickness of 65 cm in the barrel and 60 cm in the endcaps. The innermost nine plates are 2 cm thick, the next four are 3 cm and the next three are 5 cm. The outer two plates are 10 cm thick in the barrel with one 5 cm and one 10 cm in the endcaps. The gaps for the RPCs are 3.2 cm apart from those between the 2 cm barrel plates, which are 3.5 cm. A cutaway view of the IFR is shown in figure 2.11.

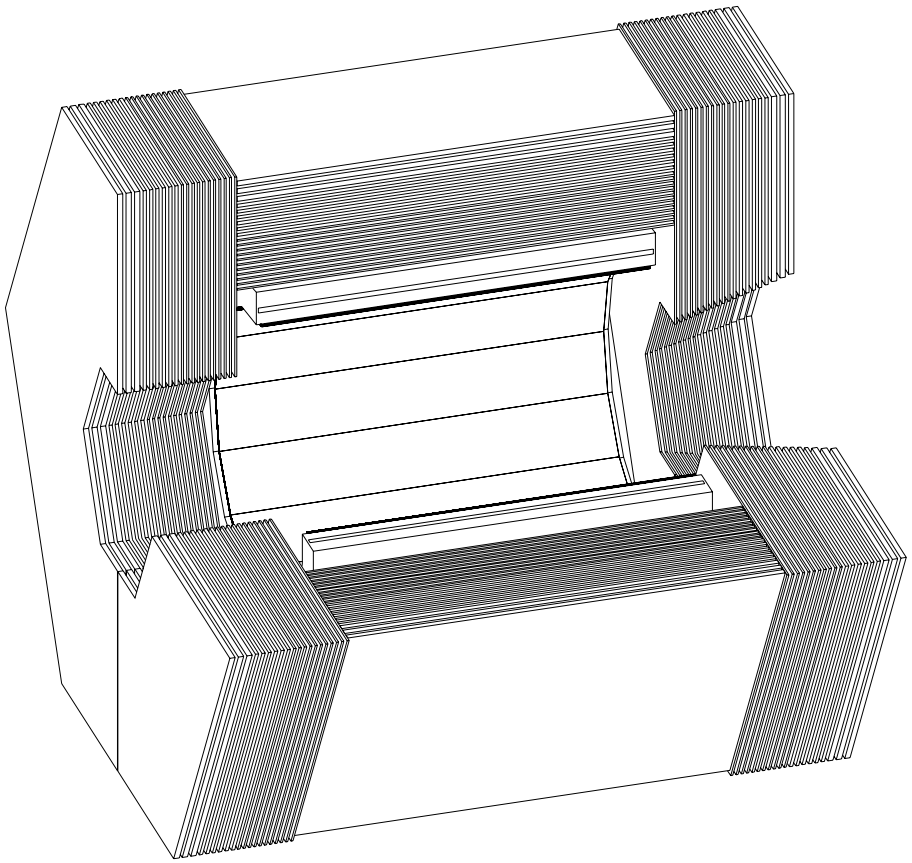

Figure 2.11: *A cutaway view of the IFR detector showing the gradation of the iron layers.*

The barrel region has 21 active detector layers. There are two layers of cylindrical RPCs immediately outside the EMC, a layer of planar RPCs in front of the iron, 17 layers in the gaps and one layer outside the iron. The cylindrical RPC is another novel feature of the BABAR IFR and can be used to provide information on particles which lose most of their momentum in the calorimeter. It consists of eight chambers,

arranged in two layers for maximum efficiency. Each RPC is one quarter of a 147 cm radius cylinder and is made by joining four modules together, for a total of 32 modules. The barrel planar RPCs are made from three modules each which makes for a total of 342 modules since the barrel yoke is divided into sextants.

The endcap doors are also hexagonal in shape and are split into two halves vertically to allow the inner detectors to be accessed. There are 18 RPC layers and each one consists of 6 chambers with a total of 216 modules.

2.3.6.2 The RPCs and Readout System

A cross-section through a BABAR RPC is shown in figure 2.12 and the general principle of operation is described in [39] and [40]. The electrodes are plates of 2 mm thick Bakelite with a graphite coating on the external surfaces. The graphite layers are covered by PVC insulating films and one is connected to ground while the other is connected to high voltage (∼8kV). Spacers made of PVC ensure that the electrodes remain separated and parallel. The gap is filled with comparable quantities of argon and Freon with a few % of isobutane. An induced pulse is picked up by aluminium strips which are present on both sides of the chamber. The strips on one side run orthogonally to those on the other side so that the chamber can provide full three-dimensional position information. The strips are attached to an insulator, on the other side of which is a grounded aluminium plane.

In the barrel, the readout strips that measure the z-coordinate have a pitch of 38.5 mm and those that measure the ϕ-coordinate vary from 19.7 mm to 33.5 mm. In the endcaps, the strips measuring y position have a pitch of 28.4 mm and for those that measure x position it is 38 mm. The data from sixteen strips is passed to a Front End readout Card(FEC) which then passes the active strips to a TDC circuit. The TDC output is stored in buffers which allow for the trigger latency before being passed along an optical fibre to the BABAR DAQ system.

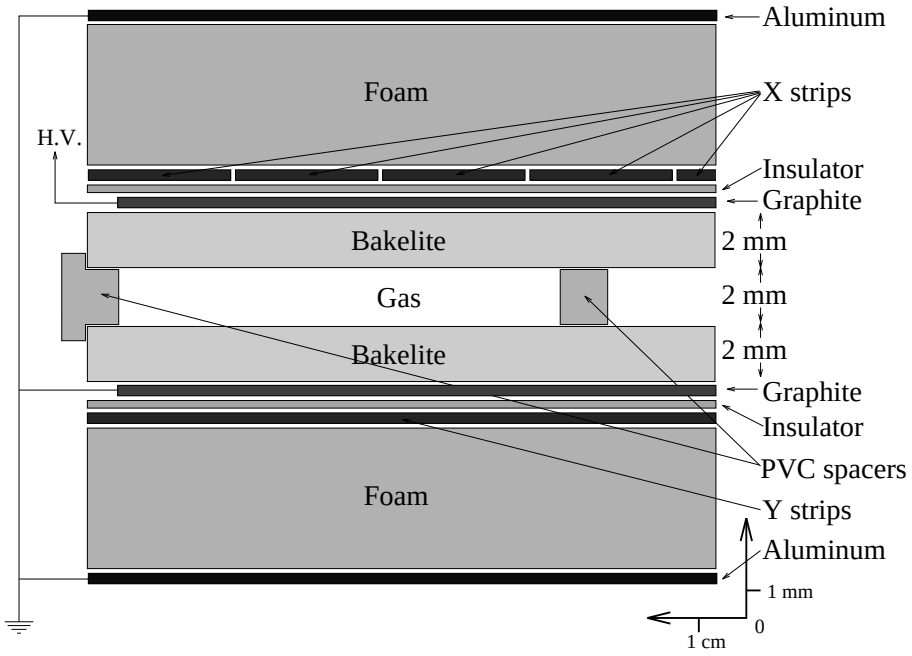

Figure 2.12: *A schematic cross-sectional view of a BABAR RPC.*

2.3.7 The Trigger System

The purpose of the BABAR trigger system is to select interesting physics events, with a high and well known efficiency, for mass storage. The two main components are Level 1, which runs in hardware and Level 3, which is purely software. From the PEP-II beam crossing rate of 238 MHz, the Level 1 trigger must accept events no faster than 2 kHz, as required by the data acquisition system. The job of the Level 3 trigger is to further reduce this rate to no more than 100 Hz, as required by the online computing system. The trigger system design requirements are described in detail in [41].

The Level 1 trigger is comprised of the drift chamber trigger, the electromagnetic calorimeter trigger and the global trigger. The drift chamber and calorimeter triggers construct basic data objects called *primitives* such as track segments and energy sums of fixed sets of crystals. The global trigger then combines these objects in var-

ious ways to produce 24 output trigger lines. For example, the charged track trigger requires at least two tracks in the drift chamber, one with $p_t > 0.18\,\mathrm{GeV/c}$ and one with $p_t > 0.12\,\mathrm{GeV/c}$. The energy trigger requires two clusters in the electromagnetic calorimeter, with energy thresholds designed to be efficient for minimum ionizing muons. These two orthogonal methods allow for good cross-calibration of the trigger efficiency. Simulation of this 'open trigger' in nominal background conditions generates an output rate of 1.5 kHz and 100% efficiency inside the fiducial region of the detector for B and τ physics events [42]. A level 1 accept signal is generated if a pre-determined set of trigger lines fire for a given event. In addition the latency in L1 must not be more than $12\,\mu$s with a jitter of less than $1\,\mu$s.

The Level 3 trigger operates after the event has been assembled and employs various tools to reduce backgrounds while still keeping the physics events. More complex algorithms can now be employed since information from the whole event is available. In particular, track impact parameters can be examined to reject events which did not originate from the primary vertex. Also, timing information can be used to reject background events from other beam crossings. Another way to discriminate background from physics events is by matching tracks from the silicon tracker and the drift chamber. It has been shown under nominal background conditions that the output of L3 can be kept to the budgeted value of 100 Hz. Of these events, ~ 80 Hz are two-photon processes and Bhabhas leaving less than $\sim$ 20 Hz of potentially interesting hadronic events.

The trigger system is designed to meet the 100 Hz output requirement under a range of background conditions and possible luminosity upgrades to $10^{34}\,\mathrm{cm^{-2}s^{-1}}$. However, if the situation arises where Level 1 can no longer meet the 2 kHz requirement for input to Level 3, then it will be necessary to construct a Level 2 trigger system as an intermediary stage.

2.3.8 Data Processing - from Detector to Desktop

It is worthwhile now to make an attempt to describe the various stages of processing that data from the detector experiences before becoming a histogram on a computer screen. When data is first read out by the detector after an event has been triggered on, it is in the form of digitized information produced by the readout electronics of the detector subsystems. This data is assembled into an event by the ODF (online dataflow) system. It is then processed by OEP (online event processing) which performs monitoring and calibration tasks and also includes the L3 trigger classification. The data is then stored in files before being processed by OPR (online prompt reconstruction). This last stage takes the raw data and reconstructs it into more physics-like objects such as tracks and clusters before associating these reconstructed objects to produce candidates for particles. These candidates are then used to carry out some preliminary physics analysis like particle identification and composite particle making. The OPR system is also responsible for running monitoring, calibration and alignment code before storing all the data in an object-oriented database. From here the data is available for any collaborator to run their analysis on it.

Chapter 3

Muon Identification Using the Electromagnetic Calorimeter

3.1 Introduction

The identification of muons in BABAR is crucial for both B-flavour tagging and J/ψ reconstruction. Decay modes such as $B^0 \to D^{*-} l^+ \nu$ reveal the flavour of the initial B through the charge on the lepton. Since two Bs are produced in a coherent state, this measurement allows the flavour of the *other* B, at the same point in time, to be inferred. Many final states of interest for CP studies contain a J/ψ which must be reconstructed in its decay to either two electrons (BR=6%) or two muons (BR=6%). Examples include $B^0 \to J/\psi\, K^0$ and $B^0 \to J/\psi\, K^{*0}$. It is often useful to separate the decays to muons from those to electrons as the resultant mass distributions can look quite different due to bremsstrahlung in the electron mode.

Lepton identification is also of importance in studies of semileptonic and leptonic charm and beauty decays.

3.2 Muon Identification with BaBar

The primary muon identification device within BaBar is the IFR. It relies on the differing interaction patterns of muons and pions in the iron to discriminate between the two particle species. However, as shown in figure 3.1 the IFR muon identification capabilities decrease progressively below about 1.2 GeV/c when muons are not fully penetrating [43]. At momenta smaller than ∼400 Mev/c, charged tracks do not even reach the iron due to the effect of the magnetic field, and energy loss in the inner detector systems. Thus it is helpful to use information from other detector subsystems at low momenta, possibly in conjunction with that from the IFR.

It is useful now to give a description of the method used in the IFR. This will clarify the role of the IFR in detecting and identifying muons and also give a flavour of how particle identification is done within BaBar.

3.2.1 Muon ID in the IFR

Tracks in the IFR are first reconstructed in two-dimensional projections in each sector. The two orthogonal projections are then combined to give a 3D cluster. Extrapolation of charged tracks from the drift chamber out to the IFR then allows for clusters from different sectors to be combined into a composite cluster. This object is then considered as a candidate muon or charged hadron and is processed by a discrimination algorithm. The identification algorithm assumes that the cluster has been produced by a muon or a pion. Other charged hadrons ($K^{\pm}$, proton) interact similarly to pions and are discriminated from pions by other detectors within BaBar. Electrons do not normally reach the iron since they tend to deposit all their energy in the EMC and any leakage has to traverse the inner RPCs and magnet structure before reaching the IFR.

The main discriminating variables for μ/π separation relate to the detailed pattern

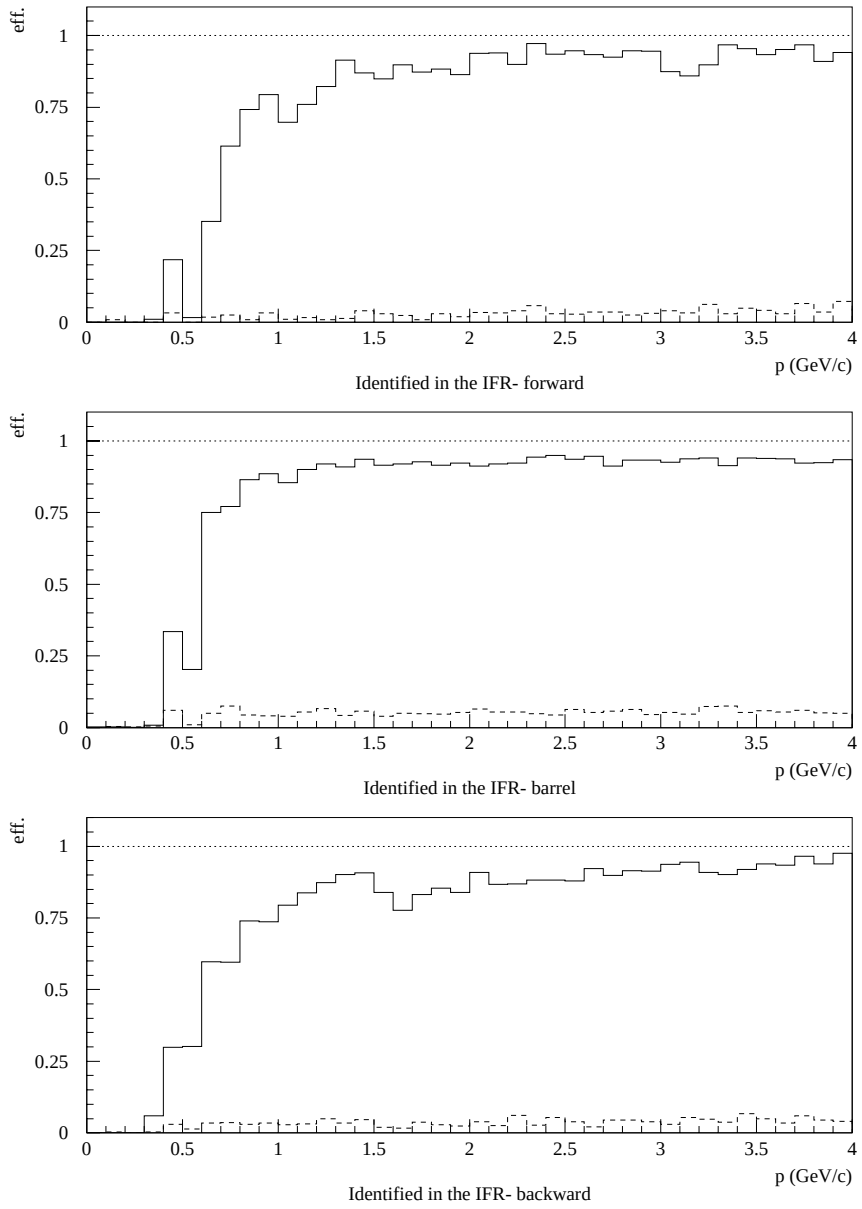

Figure 3.1: *Muon efficiency (solid line) and pion mis-id probability (dashed line) in the IFR as a function of momentum for forward endcap (top), barrel (middle) and backward endcap (bottom).*

of hits within the clusters. Prime examples are the penetration depth in the iron of the track, the transverse size of the cluster and the number of skipped layers along the length of the cluster which may be caused by neutral particles from a hadronic shower. To combine all of the variables, a likelihood ratio is formed. The probability distribution of each variable $x_i, i = 1, \ldots, n$ is calculated in 16 momentum bins from 0 to 4 GeV/c and different angular bins corresponding to the barrel, the endcaps and overlapping regions in between. The likelihood ratio is defined as

$$R = \log_{10}(P_\pi/P_\mu), \tag{3.1}$$

where P_π and P_μ are products of the individual probability distribution values for each variable under the pion or muon hypothesis respectively, i.e.

$$P_{\mu/\pi} = \prod_{i=1}^{n} P_{\mu/\pi}(x_i) \ . \tag{3.2}$$

The distribution of R is then normalized giving a distribution from which a significance level can be derived for a particular candidate under a certain hypothesis.

3.2.2 Muon ID in Other Detector Subsystems

The DIRC can provide some μ/π separation in the range 250 MeV/c<p<750 MeV/c. At lower momenta, particles do not generally reach the quartz and at higher momenta, the Cherenkov angles are too close for discrimination. Measurements of $\mathrm{d}E/\mathrm{d}x$ in the SVT and DCH are generally not useful for μ/π separation due to the closeness of the respective Bethe-Bloch curves.

The EMC however, can provide a reasonable amount of discrimination over a wide momentum range. At 300 MeV/c, around 75% of simulated muons deposit energy in the calorimeter. Identification is then possible for all momenta up to several GeV/c (the upper limit for particles in BABAR). The current algorithm used by the BABAR reconstruction code for identifying muons in the EMC will now be described.

3.3 Principle of Muon Identification in the EMC

It is possible to distinguish to some extent between muons and charged hadrons in the EMC because their distributions of deposited energy look rather different. Being a lepton, a muon will not interact hadronically in the CsI but will rather lose energy through ionization. The mean energy loss rate (or stopping power) via this process is given by the Bethe-Bloch formula, which is defined in Appendix A [5] and shown for CsI in figure 3.2.

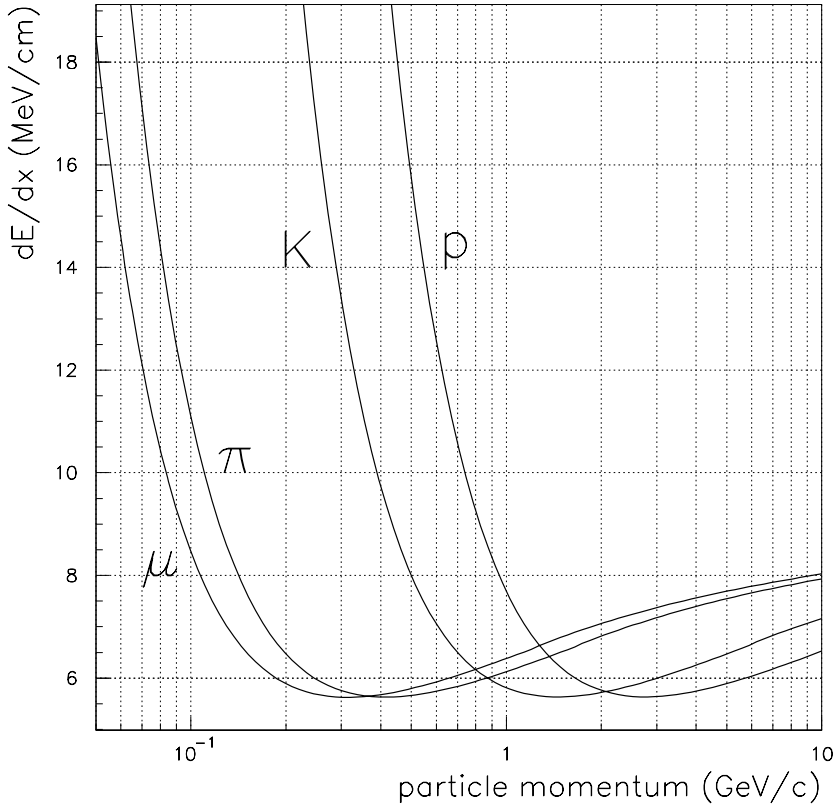

Figure 3.2: *Bethe-Bloch curves for muons and charged hadrons in CsI. The momentum range is from 50 MeV/c to 10 GeV/c.*

On the other hand, pions can also behave as ionizing particles when traversing the

CsI but a significant fraction of them will be involved in a hadronic interaction with a nucleus in the material as well. This will often produce an energy deposit unlike that from a muon, allowing for some separation of the two particle species using the deposited energy as a discriminating variable. The difference in measured energy distributions for Monte Carlo generated particles can be seen in figure 3.3.

Only positively charged muons, pions and kaons are shown as the distributions for their negative partners are very similar. The exceptional case is that for antiprotons. Protons behave rather the same as pions and kaons but antiprotons can undergo annihilation processes with nuclei in the CsI giving a very different distribution to all the other charged hadrons.

3.4 Method of Muon Identification in the EMC

With the knowledge that some muon identification is possible here, we then proceed to find a function that describes the muon energy distribution well. The first guess might be a Landau distribution since this is the energy spread we should expect for an ionizing particle [44]. However, this turns out to be a poor fit as the distributions are often not asymmetric enough and do not fall off sharply on the low side of the peak. The thickness of CsI in the EMC goes a good way to explaining this behaviour. The Landau distribution is most appropriate for thin absorbers. As the material becomes thicker, there is a greater change in the particle momentum as it traverses the material. This results in a greater region of the Bethe-Bloch curve being sampled and therefore the smearing out of the $\mathrm{d}E/\mathrm{d}x$ distribution as it represents many different Landau distributions rather than approximating well to just one.

In fact, due to the variable nature of the shape of the energy distribution with momentum and polar angle, it turns out that a more flexible function is necessary.

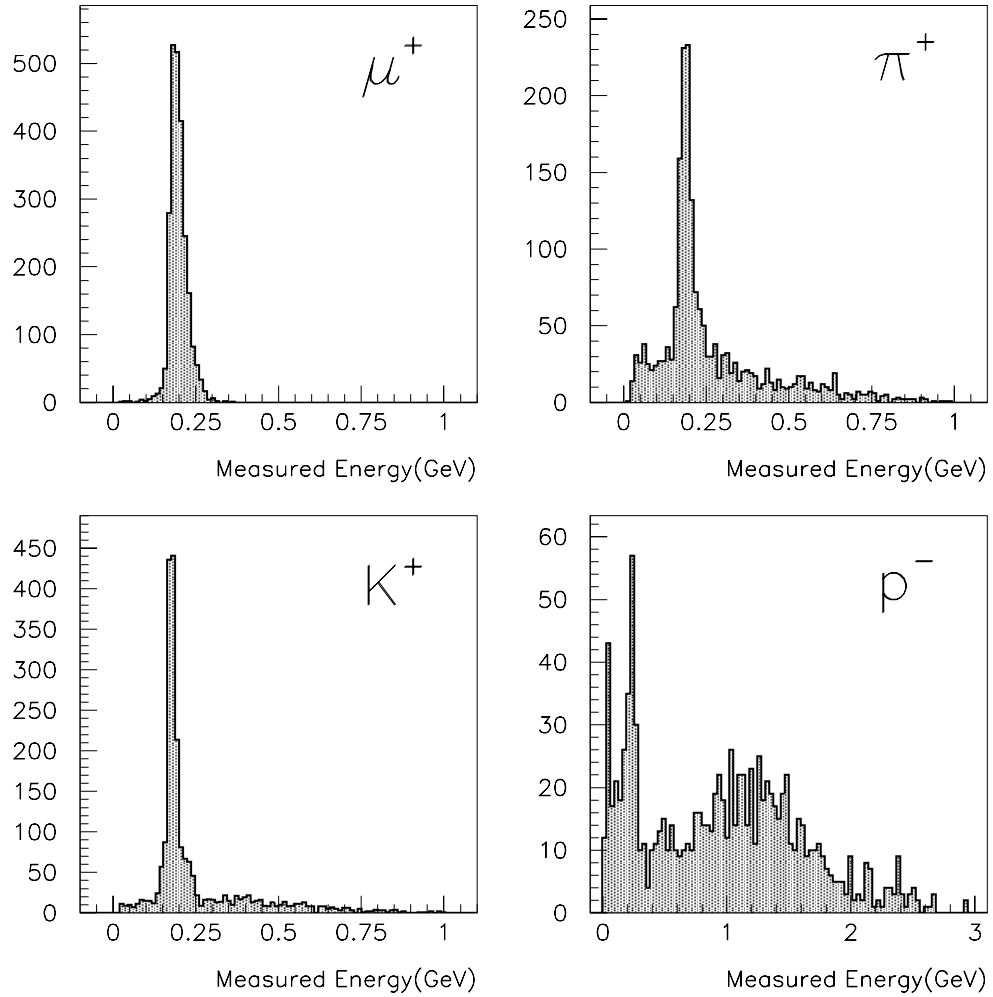

Figure 3.3: *Monte Carlo energy distributions for the interactions of different types of charged particles in the EMC. The particles were generated with a momentum of 1.2 GeV/c.*

A lineshape consisting of the sum of a Gaussian and a Breit-Wigner function fits well:

$$F(x) = N_1 \exp\left(-\frac{(x-\mu_1)^2}{2\sigma_1^2}\right) + N_2 \frac{1}{(x-\mu_2)^2 + \sigma_2^2/4} \tag{3.3}$$

where the N_i, μ_i and σ_i are respectively the normalizations, means and widths of the two distributions and x in this case is the energy as measured by the EMC. Although it does not have the same physical relevance that the Landau formula has, it describes the behaviour of muons in the BABAR calorimeter very well, which is the most important criterion here. It allows for optimal μ/π separation in the EMC over all momenta and polar angles while using energy as a discriminating variable.

All the fitted energy distributions of μ^+ interactions that were used are shown in figures 3.4 to 3.8. The equivalent distributions for μ^- look very similar for all $\cos\theta$ and momenta bins and so are not shown here. The single particle events were generated using the detailed BABAR detector simulation BBSIM. The angular distribution is flat in $\cos\theta$ with an enriched sample in the endcap region to provide usable statistics there. Different MC runs were used with particle momentum at the origin of 300 MeV/c, 500 MeV/c, 800 MeV/c, 1.2 GeV/c and 3.0 GeV/c. The resulting histogram data was divided into five bins in $\cos\theta$, for each of the five momenta. The first four angular bins cover the barrel calorimeter and the remaining bin covers the endcap region. The reason for binning in $\cos\theta$ comes partly from the layout of the EMC(see section 2.3.5.1), in particular the fact that the crystal length is not constant over θ. Another reason is that the amount of material in front of the EMC also varies as a function of polar angle.

It is worthwhile now to discuss some of the distributions, especially those which seem anomalous on initial inspection. The 300 MeV/c muons tend to have a significant tail on the low side. These tracks have a radius of curvature of ~ 65 cm in the absence of material. Given that they lose energy due to material in front of the EMC and subsequently in the CsI itself, they can bend sufficiently to leave the EMC before depositing the average 200 MeV energy there. They can lose energy very quickly

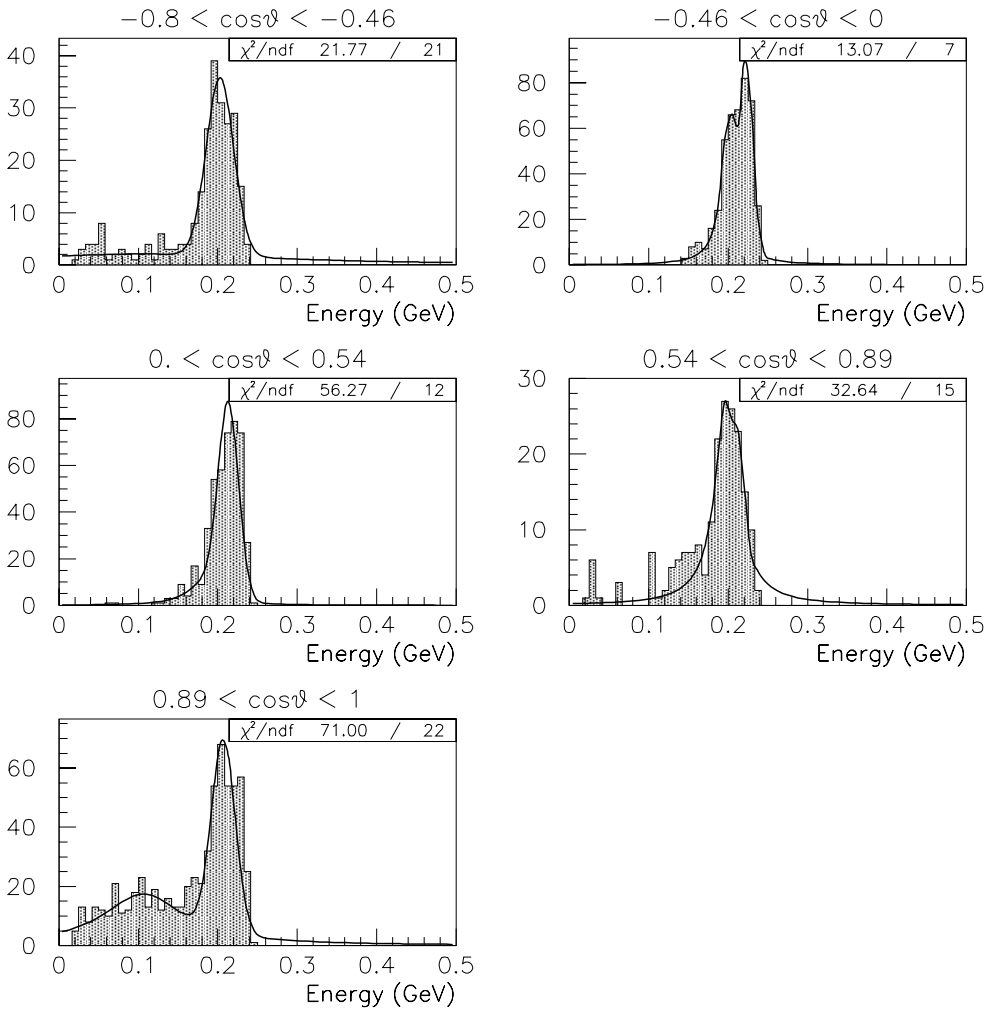

Figure 3.4: *Energy distribution plots for 300 MeV/c muons in the BABAR EMC. The sample is divided into five bins in polar angle.*

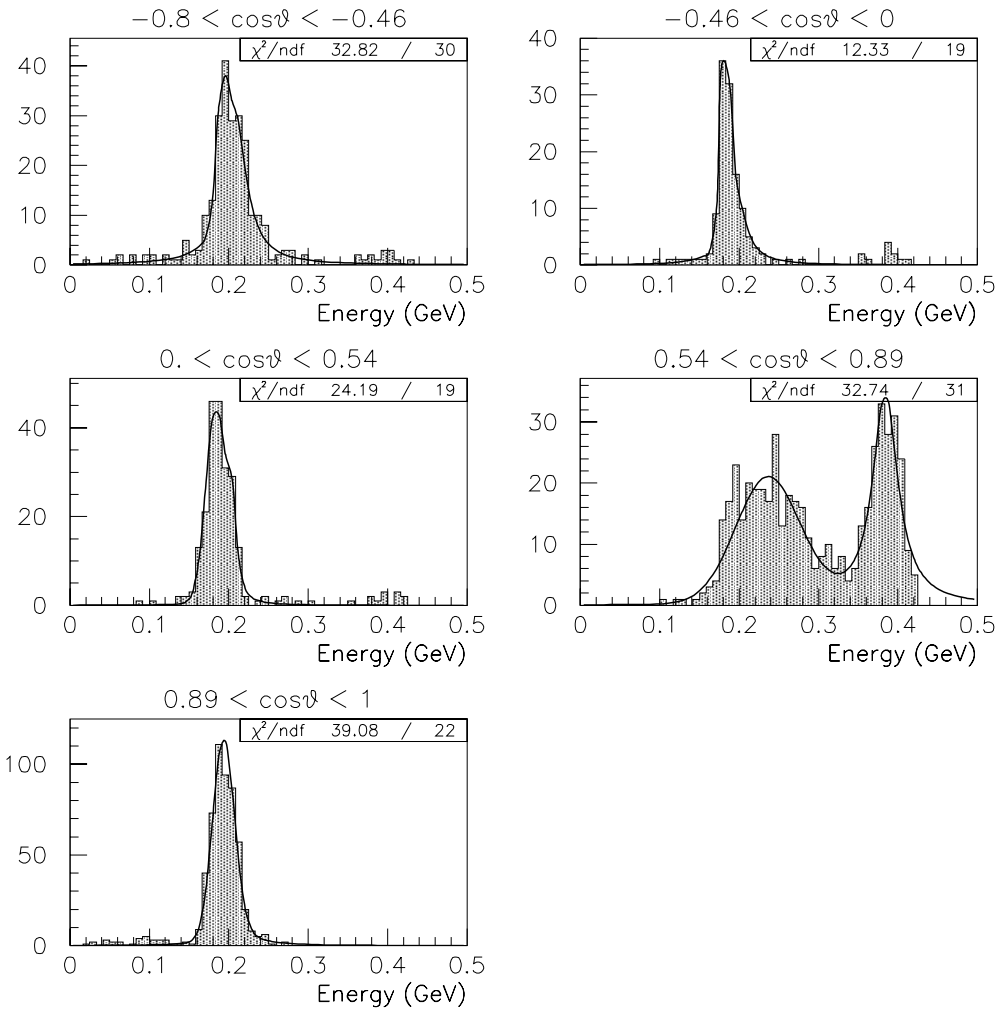

Figure 3.5: *Energy distribution plots for 500 MeV/c muons in the BABAR EMC. The sample is divided into five bins in polar angle.*

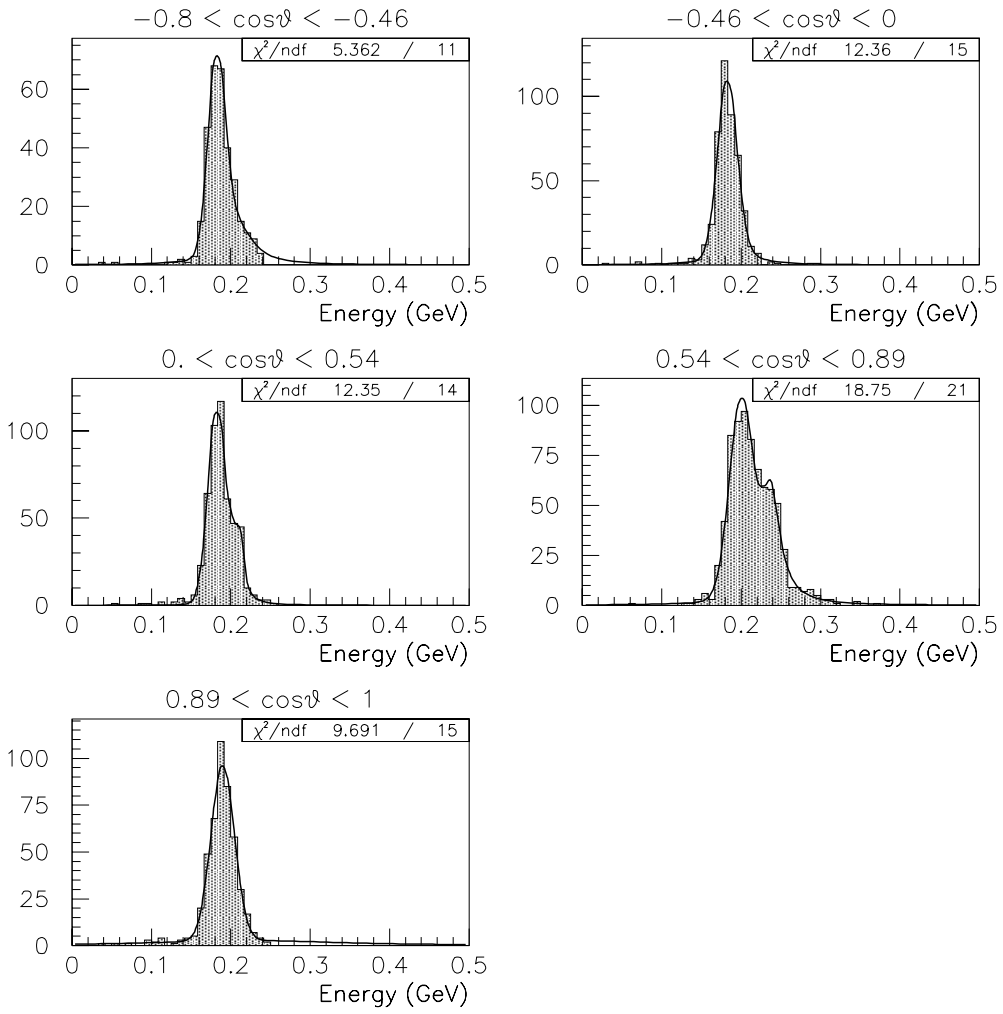

Figure 3.6: *Energy distribution plots for 800 MeV/c muons in the BABAR EMC. The sample is divided into five bins in polar angle.*

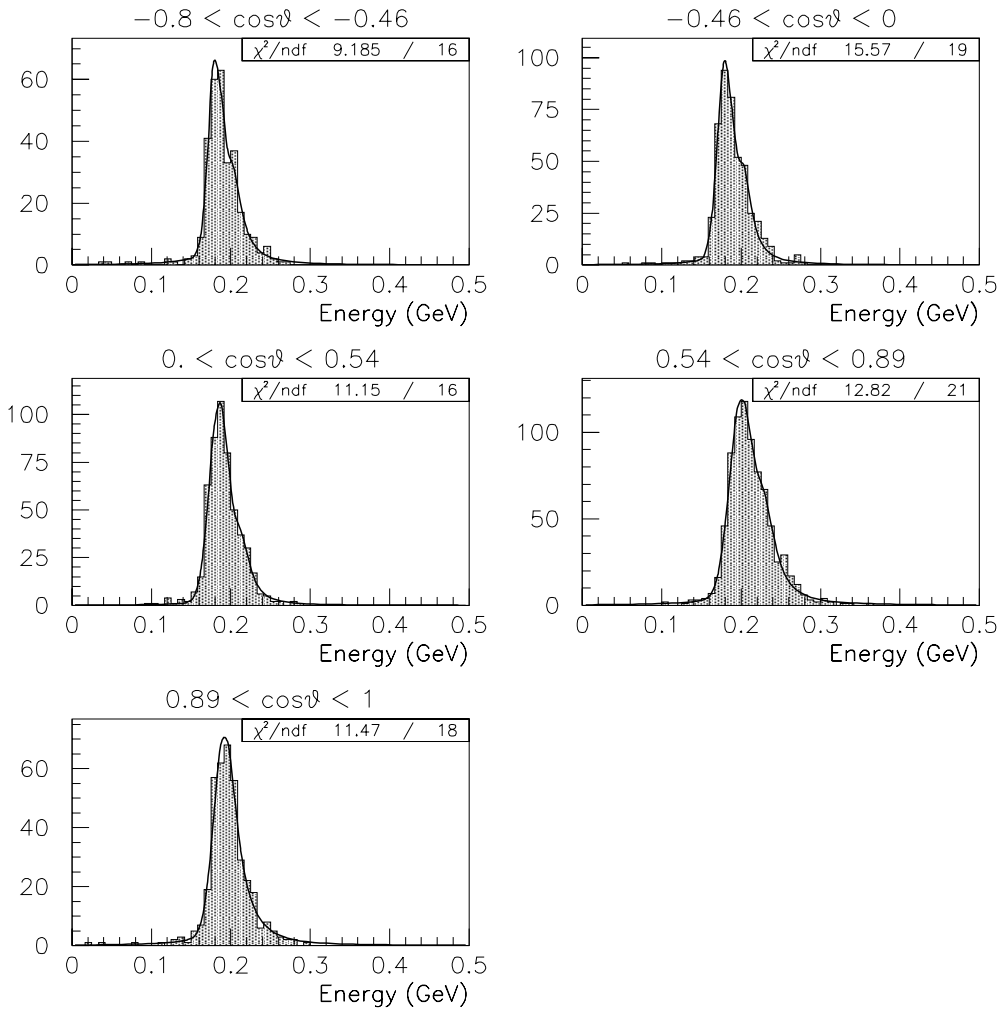

Figure 3.7: *Energy distribution plots for 1.2 GeV/c muons in the BABAR EMC. The sample is divided into five bins in polar angle.*

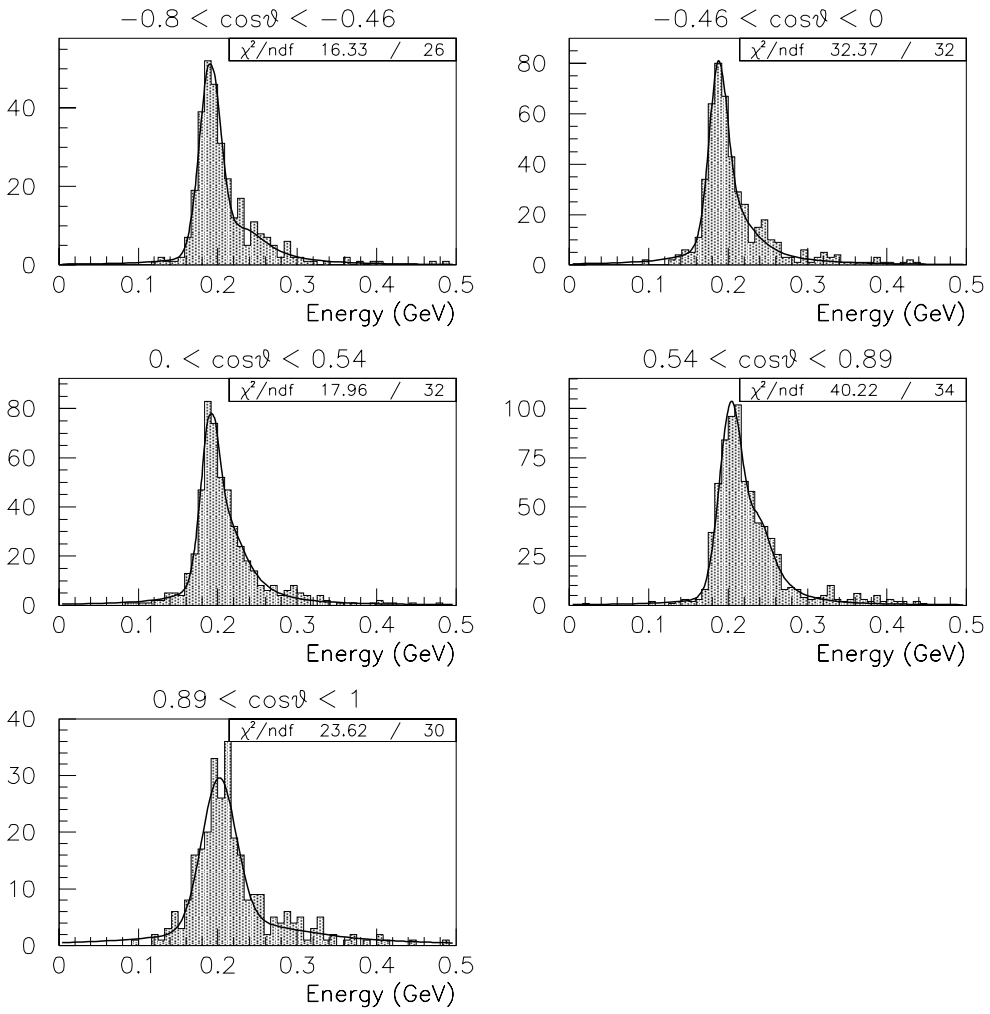

Figure 3.8: *Energy distribution plots for 3 GeV/c muons in the BABAR EMC. The sample is divided into five bins in polar angle.*

once inside the calorimeter due to the shape of the Bethe-Bloch curve (figure 3.2). The tail is more pronounced in the first and last $\cos\theta$ bins due to the finite physical extent of the EMC causing some clusters to be only partially contained. In the final $\cos\theta$ bin, the effect is increased further due to the track encountering significantly more material before reaching the EMC than for other angular bins. At 500 MeV/c there are clusters of events centered at about 400 MeV. This is due to muons which stop and decay in the EMC. This can happen when the particle momentum falls below that for a MIP and energy loss then follows the steep side of the Bethe-Bloch curve. This is as for the previous case except now the muons do not generally leave the EMC but deposit all their kinetic energy (~ 380 MeV) there. Most of the decay products' energy is of course not detected since $\mu \to e\nu_e\nu_\mu$. The effect is most pronounced for the fourth $\cos\theta$ bin due to the geometry of the calorimeter and shows the usefulness of a fit with two peaked functions for this purpose. Looking now at the 3 GeV/c muons, one notices an extended tail on the high side of the distribution. This is again an effect partially due to the shape of the Bethe-Bloch curve, except this time from the high side of the dip, the relativistic rise. However, the majority of this effect probably comes from processes other than ionization beginning to play a part in the energy loss of the muon. Obvious candidates are bremsstrahlung and the ejection of delta ray electrons.

The next step is to study the dependence of the fit parameters as a function of momentum and angle. If the variation of these parameters can be modelled over all p, θ space somehow then the predicted energy distribution for a given track under the $\mu^{\pm}$ hypothesis can be calculated. The variations of all the lineshape parameters for μ^+ are shown in figures 3.9 to 3.13. In practice there are five parameters rather than the six from the original fit function. These are the means and widths of the two distributions and the ratio of their normalizations, N_1/N_2. Forming the normalization ratio as a parameter represents dividing the whole function by N_2. This overall scaling is safe since in practice any quantities derived from the distribution

are normalized and the constant cancels out.

The general trend of the mean of the Gaussian part of the distribution (figure 3.9) roughly follows that expected due to track curvature in the magnetic field and the shape of the Bethe-Bloch curve. The anomaly in the fourth $\cos\theta$ bin at 500 MeV/c as discussed above shows up here also. The errors on the parameters come from the output of the χ^2 fit for each distribution as performed with the PAW physics analysis application [45]. There are occasional error bars which look rather large and these can usually be explained in terms of the fit. For instance, the distribution in the fourth $\cos\theta$ bin at 300 MeV/c (figure 3.4, middle right plot) is not so well described by the fitting function and this resulted in large errors for some of the fit parameters. This can be seen for example in the 300 MeV/c point in the middle right plot of figure 3.13.

Generally however, the fits are good both by eye and by inspection of the χ^2 per degree of freedom of each plot. The worse fits are some of those at p=300 MeV/c which is more or less at a momentum threshold where behaviour is always going to be difficult to model. The variation of the fit parameter errors is perhaps one way of signalling that one cannot describe perfectly all energy distributions in (p, θ) with the same fitting function. In some sense the adopted technique here is an approximation to the ideal solution, an improvisation. Nevertheless it is practical, can be implemented without too much trouble and adequately serves the needs of the problem in question. That is, to provide a reasonable degree of μ/π separation in the EMC.

The remaining question now is how to parameterize the momentum dependence of the fit parameters within each $\cos\theta$ bin. There are definite shapes there as with the Gaussian mean parameter but overall it seems that no one parameter can be modelled using a single function for all angular bins. In fact, for many of the plots it would be difficult to fit a complex curve to the points and also have confidence in the ensuing interpolations. The chosen solution for all plots is a piecewise linear

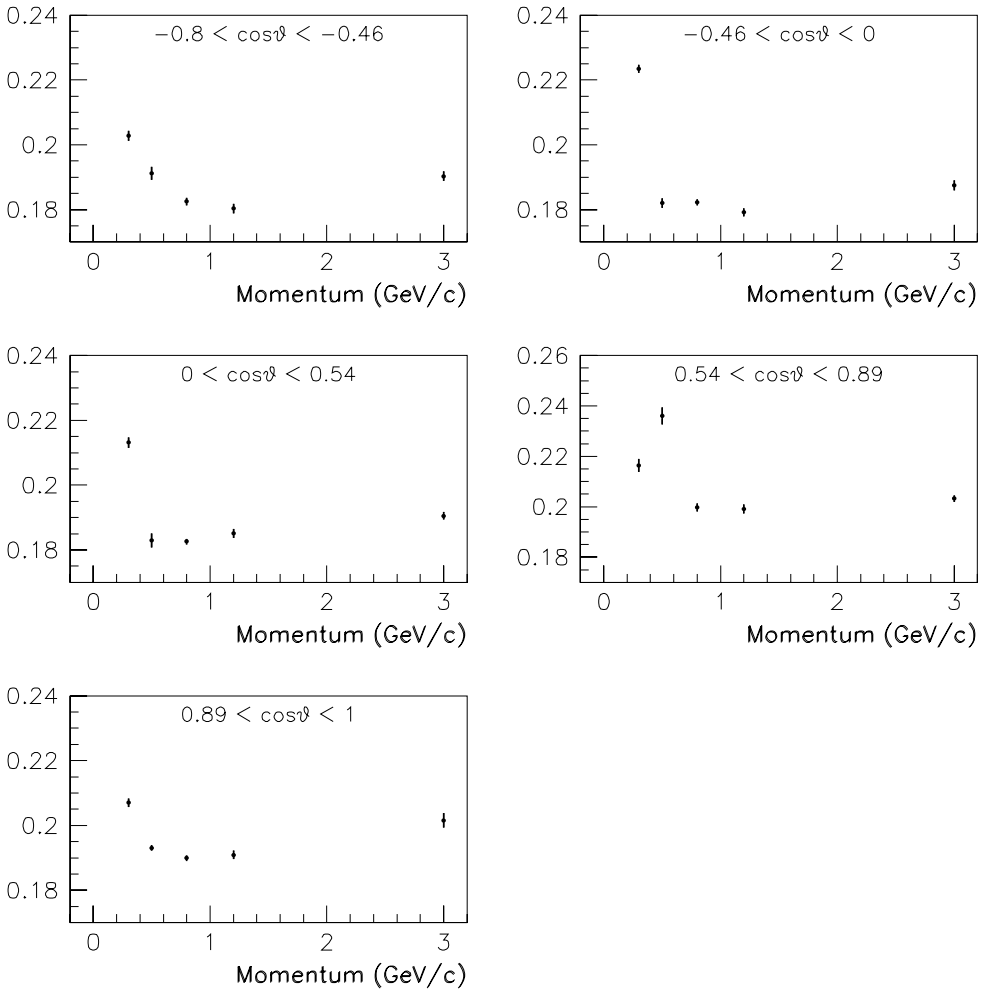

Figure 3.9: *Variation with momentum of the 'Gaussian mean' fit parameter. There are five bins in polar angle.*

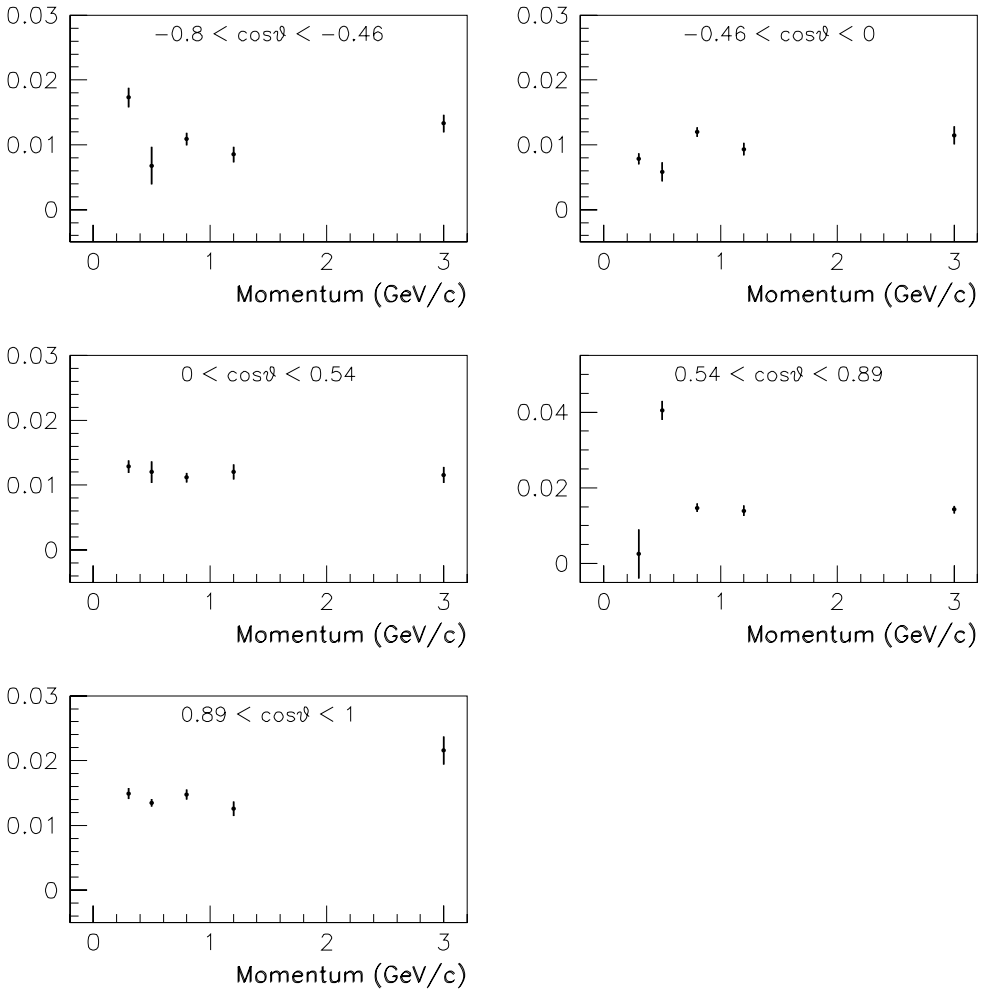

Figure 3.10: *Variation with momentum of the 'Gaussian width' fit parameter. There are five bins in polar angle.*

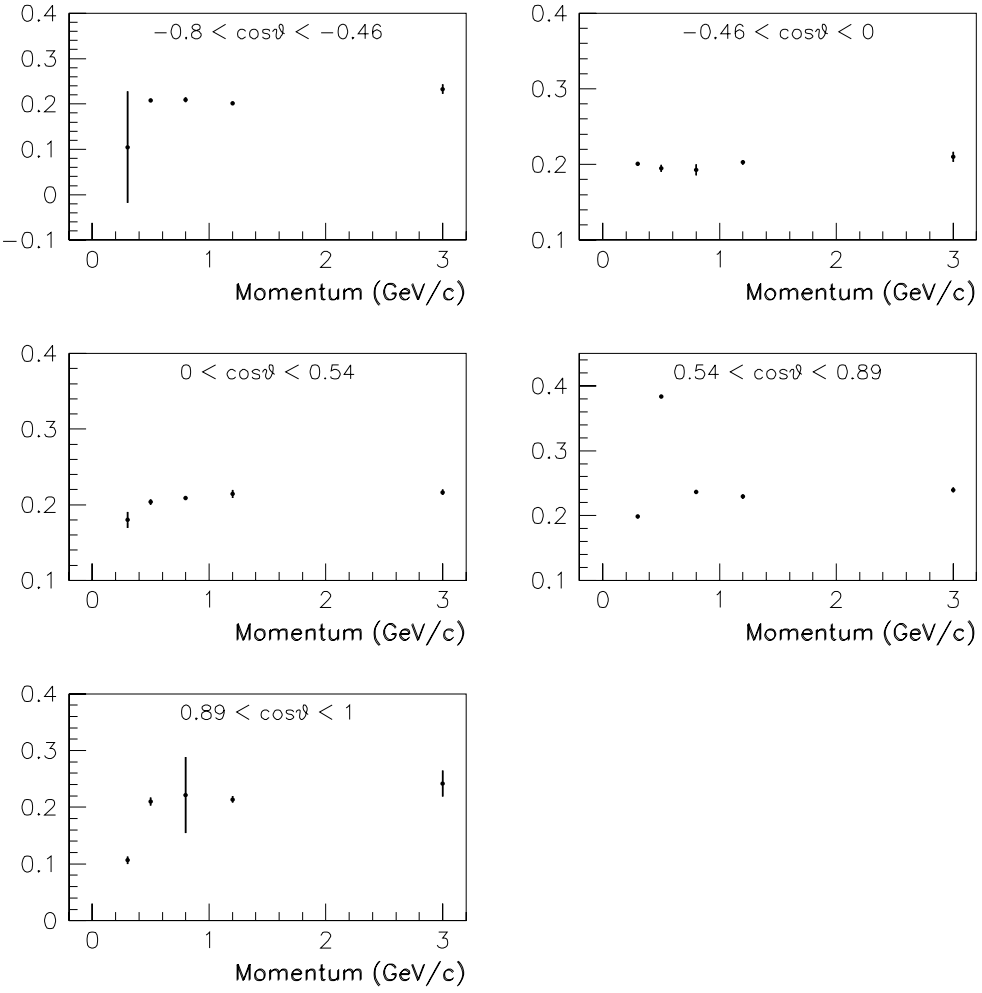

Figure 3.11: *Variation with momentum of the 'Breit-Wigner mean' fit parameter. There are five bins in polar angle.*

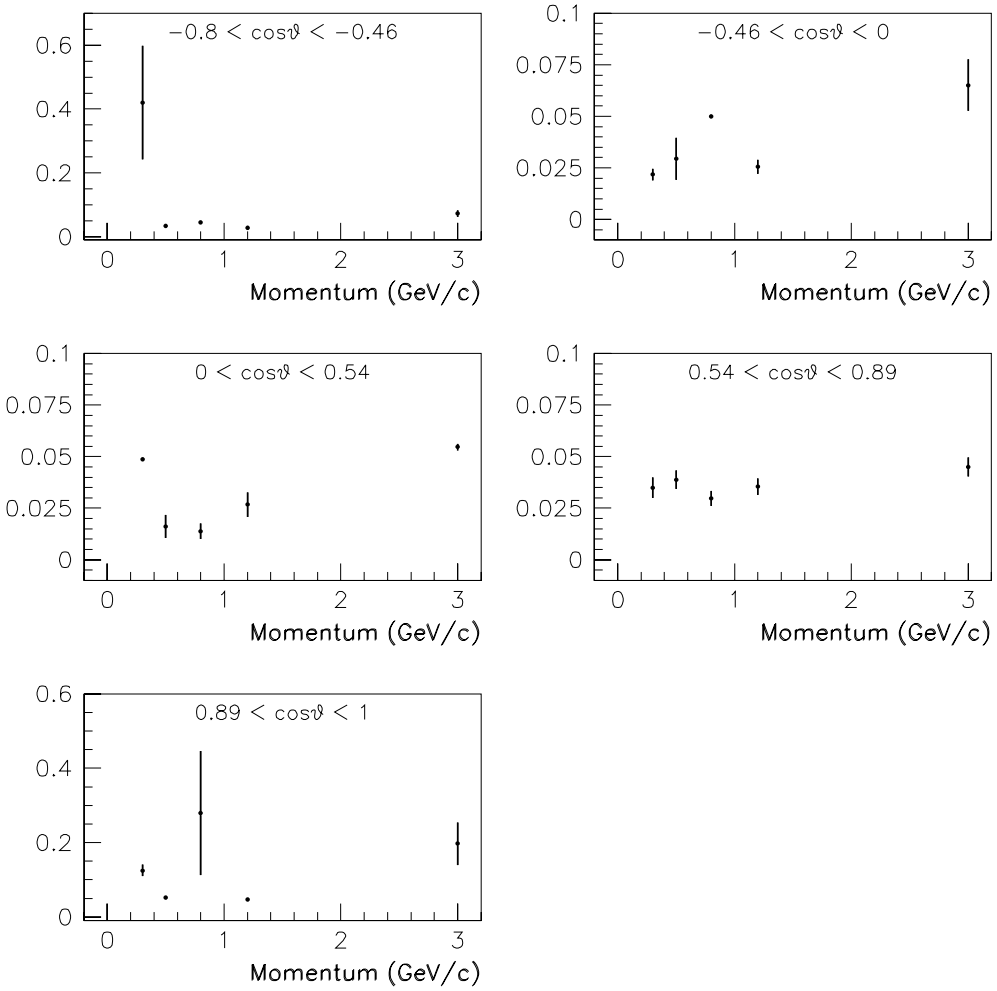

Figure 3.12: *Variation with momentum of the 'Breit-Wigner width' fit parameter. There are five bins in polar angle.*

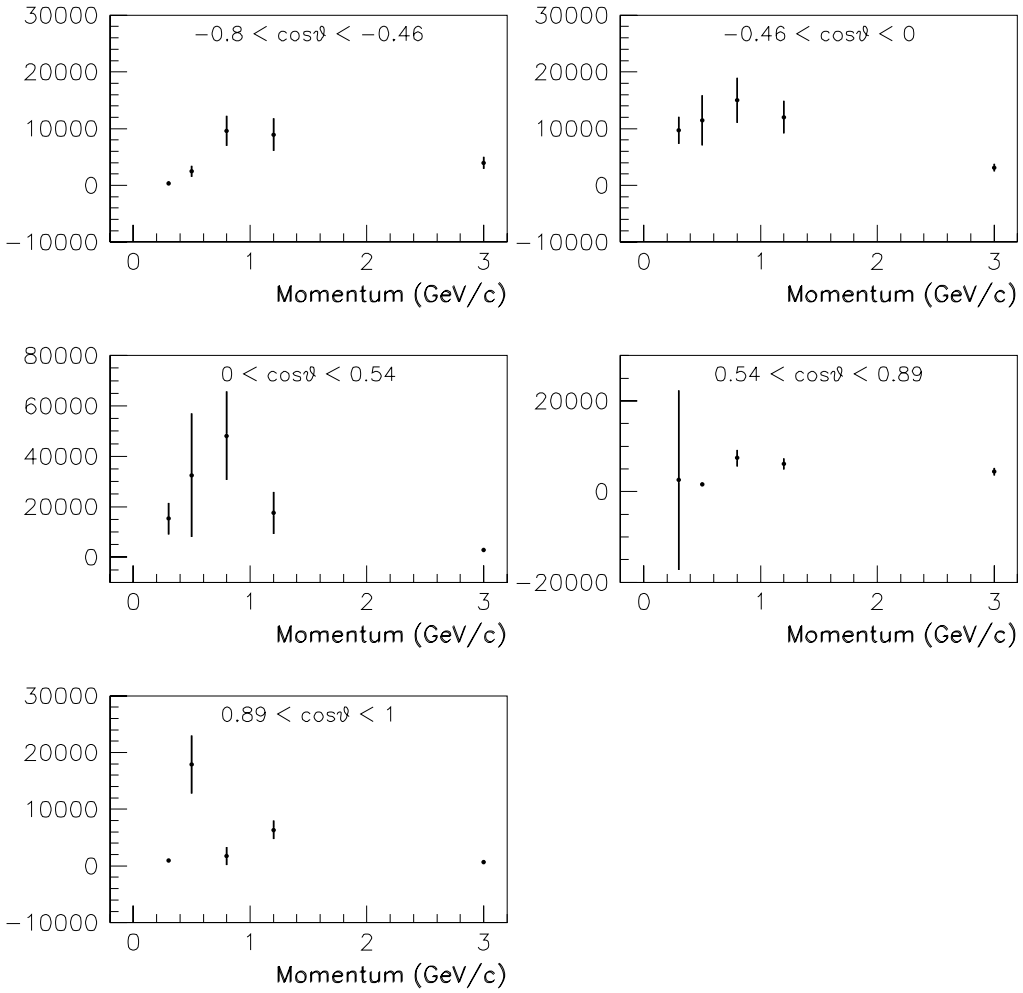

Figure 3.13: *Variation with momentum of the 'normalization ratio' fit parameter. There are five bins in polar angle.*

function joining the points. This is the simplest way to handle the interpolations between points when the behaviour is not fully known. It also takes care of any anomalies such as the 500 MeV/c, fourth bin example discussed above.

The case of extrapolation below 300 MeV/c and above 3 GeV/c still remains. For low momenta, the linear function joining the first two points in each plot is simply extended. This is a less significant region than the high momentum case since few particles reach the EMC if their momentum is much lower than 300 MeV/c. The high momentum case is handled by just keeping the parameter constant at its 3 GeV/c value. This reflects the fact that the parameters have relatively little variation between the last two points on each plot and also avoids numerical exceptions in the C++ implementation of the algorithm for very high momentum tracks.

3.5 Implementation and Results

This method of muon identification using the EMC has been implemented in the BABAR software as part of the EMC reconstruction code. To provide a fuller picture, here is the chain of modules which are executed before particle identification within the EMC is carried out:

1. `EmcCalibrateDigis`[1] - Calibration of all single crystal energies
2. `EmcDigiSparsify` - Removal of all hits which are not either above 10 MeV or next to a hit which is above 10 MeV
3. `EmcRemoveNoise` - Remove noisy and out of time digis
4. `EmcMake2dCluster` - Find a seed digi above a certain threshold and form a group of contiguous crystals around it. The energy threshold for individual

[1] 'Digi' is the generic BABAR name for the smallest unit of detector information provided by the DAQ - in this case a hit in a single calorimeter crystal

crystals is 500 KeV and the cluster threshold is 20 MeV

5. `EmcMakeIntersections` - Intersect charged tracks with the EMC. Store crystal index and coordinates of intersection point.

6. `EmcTrkClMatch` - Form associations of charged tracks with EMC clusters on the basis of whether a given track intersects any of the crystals in a given cluster

7. `EmcMakeBump` - Find local maxima within clusters and split them into 'bumps'

8. `EmcTrackMatch` - Match charged tracks to EMC bumps above 50 MeV. Calculate and store consistencies for the quality of the match.

The next module to be run is `EmcIdentify`. This first makes composite objects (EmcCands) based on the track-EMC match information derived earlier and attaches to each a global calibrator so that their calorimeter energies are correct. The EmcCands are then handed to a set of particle identifiers, including `EmcMuonIdentifier` which calculate useful discriminating statistics under various hypotheses and attach the resultant information to the EmcCands. The operation of the muon identifier for each EmcCand can be described as follows

1. Insist that the candidate contains a charged track

2. Determine from the track which $\cos\theta$ bin should be used

3. From the track momentum and charge retrieve the linear variation equation for each parameter

4. Perform the necessary interpolation/extrapolation to obtain values for all five parameters

5. Given this lineshape compute the significance level and likelihood for the candidate under the muon hypothesis.

The definition of the likelihood is simply

$$\mathcal{L}(\mu^{\pm}; p, \theta, x) \equiv \mathcal{P}(x; p, \theta, \mu^{\pm}) \tag{3.4}$$

where $\mathcal{P}(x; p, \theta, \mu^{\pm})$ is a probability density function (PDF) giving the probability that a muon of momentum p and polar angle θ leaves a signature x in the EMC. The likelihood is then a comparison between hypotheses for a fixed p, θ and x. In this case the signature is an energy deposition and the PDFs in question are the normalized versions of those in figures 3.4 to 3.8. For a full likelihood treatment, the energy distributions for the other charged particle types (e,π,K,p) would also have to be parameterized in the same way to allow formation of likelihood ratios and other useful quantities.

The significance level attached to a measurement x_0 is

$$\mathrm{SL}(x_0) = \int_{\mathcal{P}(x)<\mathcal{P}(x_0)} \mathcal{P}(x)\,\mathrm{d}x \tag{3.5}$$

where the p, θ, $\mu^{\pm}$ labels have been suppressed but are still valid throughout. This statistic provides a measure of consistency between the observed energy deposit and that expected for a muon with the given characteristics. More information on the definition and usage of discriminating statistics for particle identification in BABAR can be found in [46].

These identification statistics are then available to the end user doing physics analysis to examine and cut on as they wish. The resultant distributions are shown in figures 3.14 to 3.17 for significance levels and likelihoods. The plots were produced using Monte Carlo samples of the various particle types over the whole momentum range (200 MeV/c $\rightarrow$ several GeV). The samples were different than those used to derive the parameterization.

As can be seen in figure 3.14, the significance level distributions for muons are roughly flat as expected. Those for the other particle types tend to peak towards zero. For the charged hadrons the distribution always extends across the whole

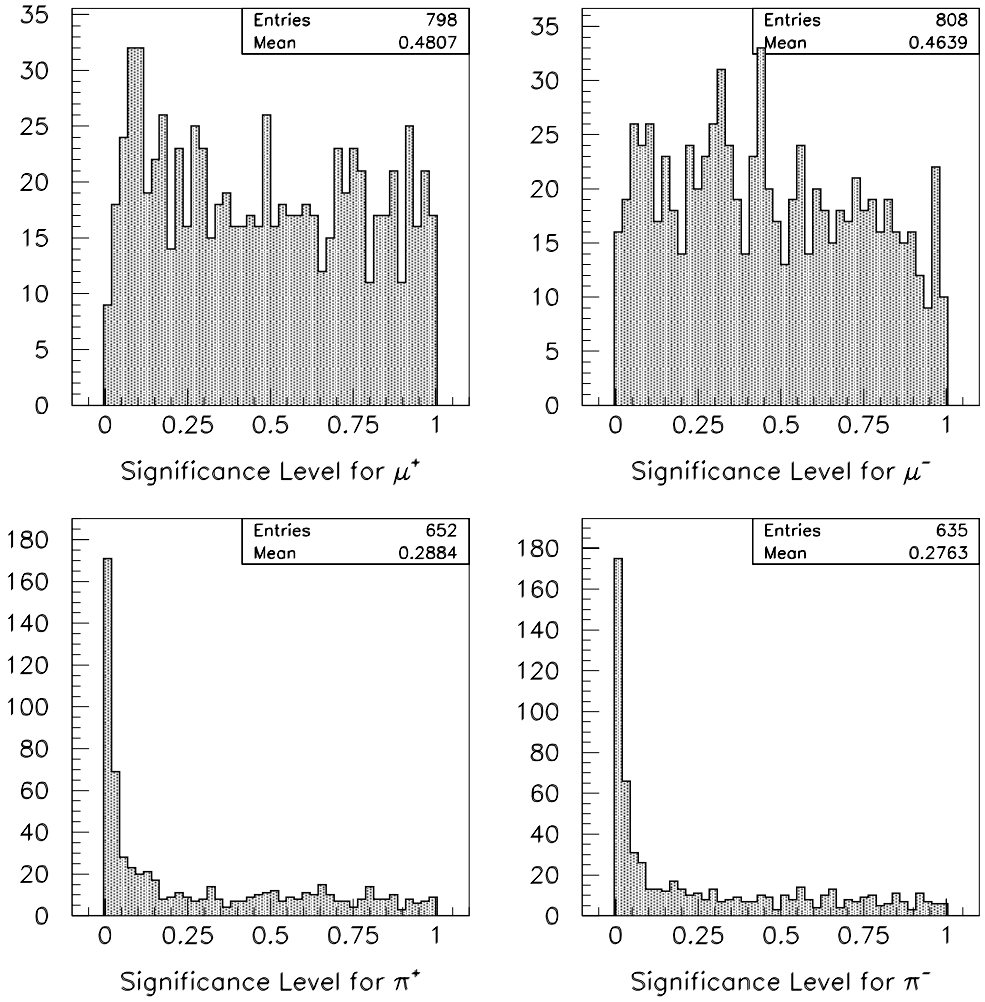

Figure 3.14: *The significance levels for simulated muons and pions.*

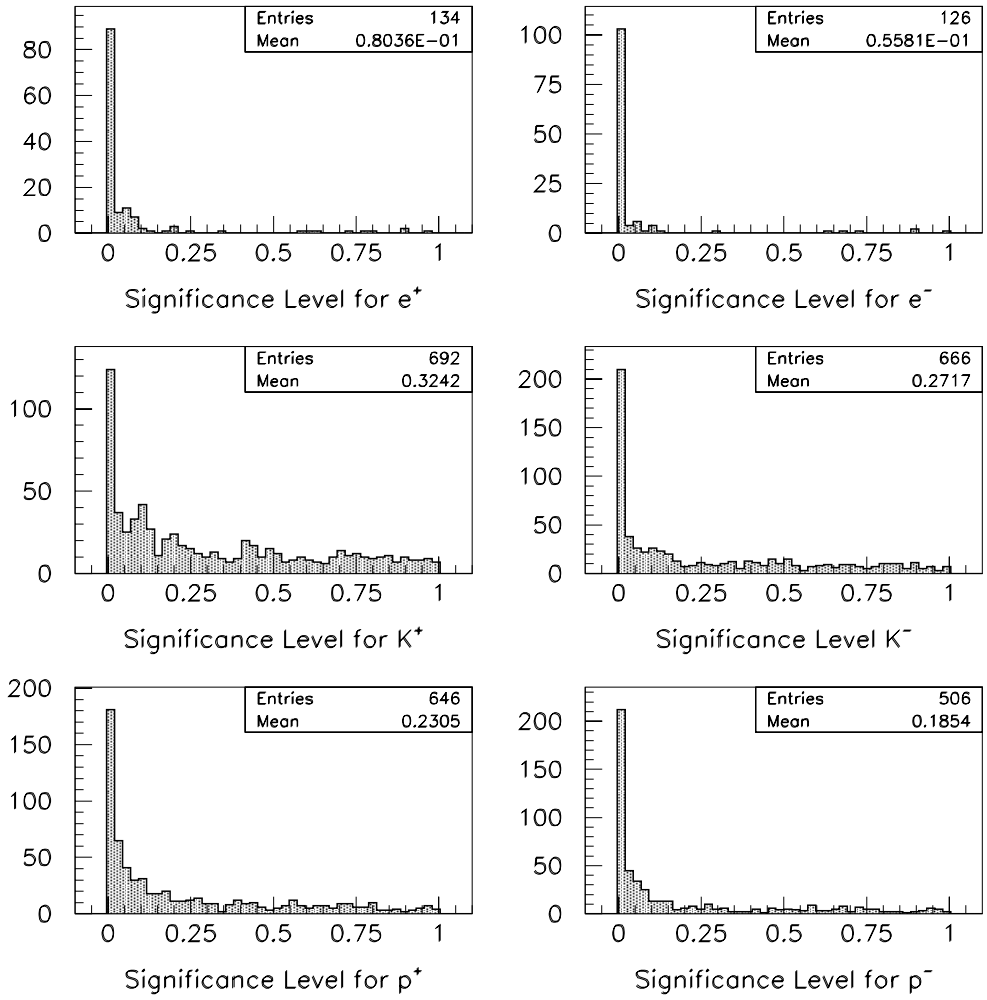

Figure 3.15: *The significance levels for simulated electrons, kaons and protons.*

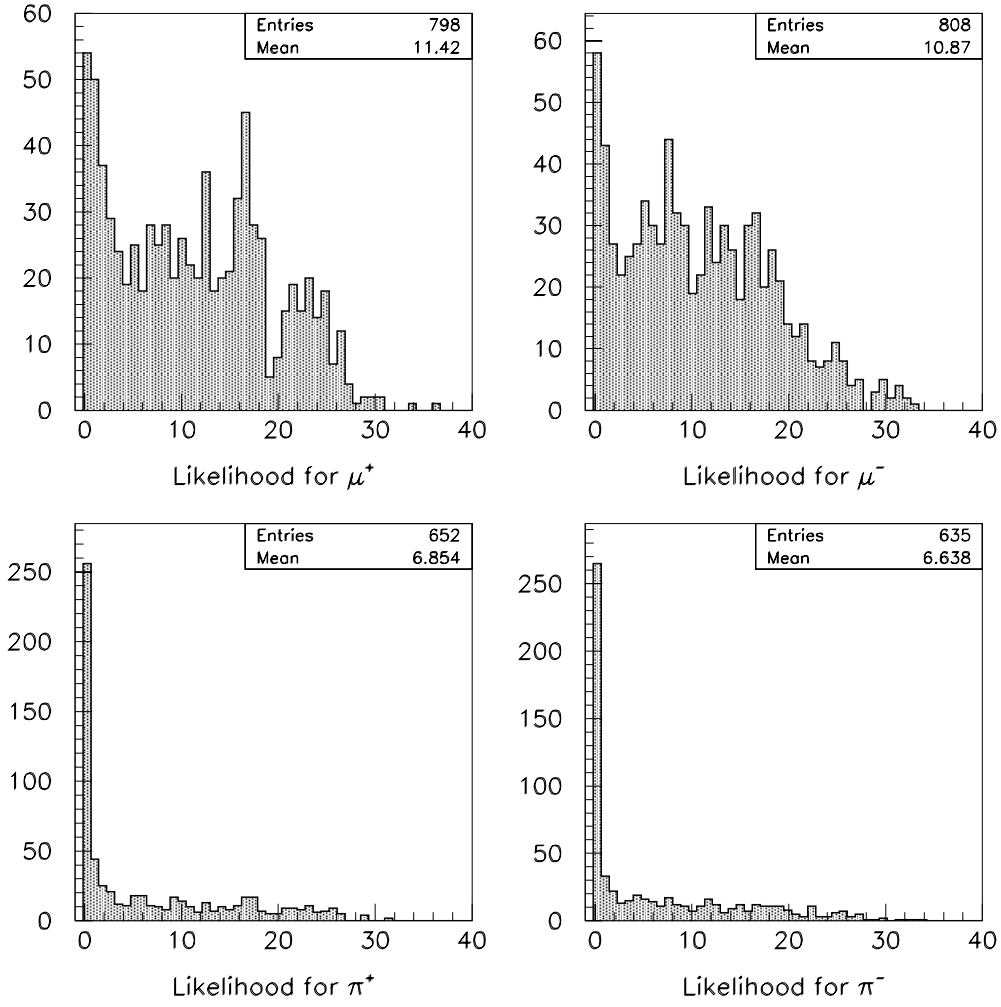

Figure 3.16: *The likelihoods for simulated muons and pions.*

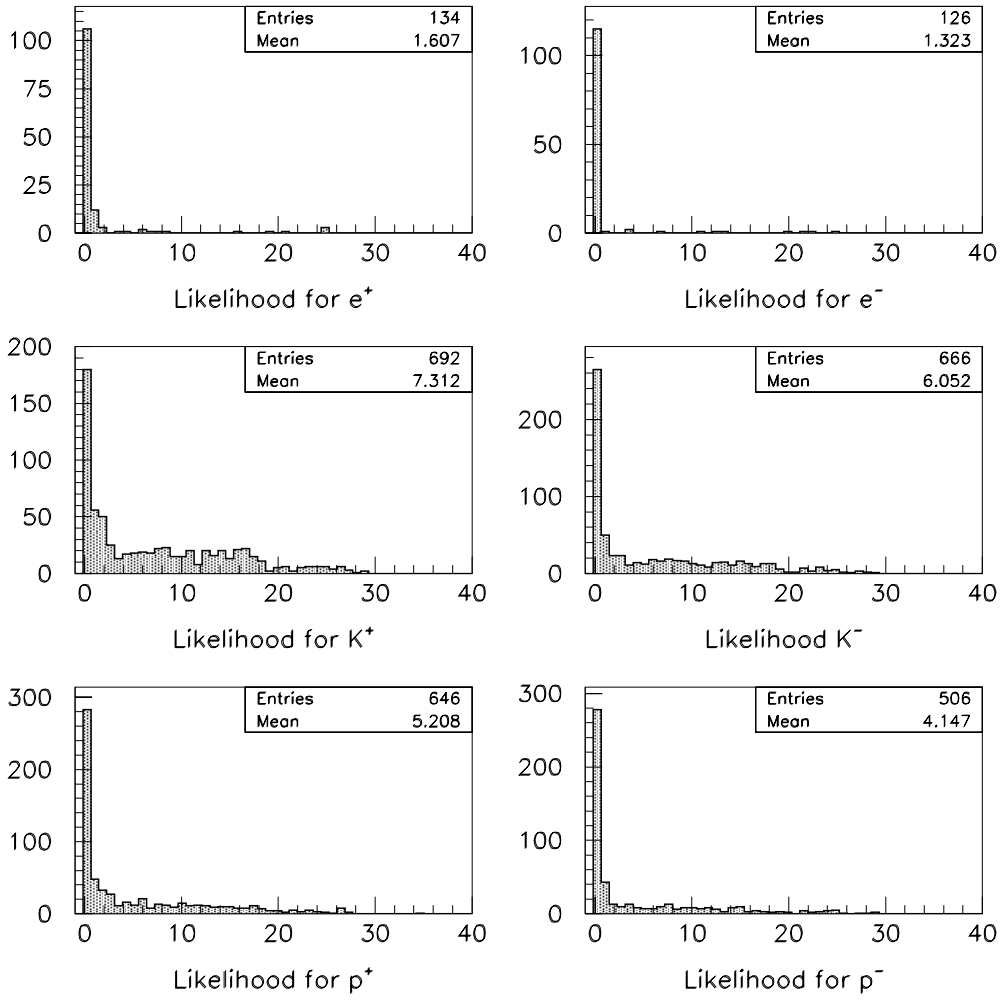

Figure 3.17: *The likelihoods for simulated electrons, kaons and protons.*

range due to the cases where they interact as a MIP and are then indistinguishable from a muon as far as the EMC is concerned. Electrons and positrons are clustered predominantly at low values due to the tendency of these particles to deposit all of their energy in the EMC. That is to say they will only mimic muons at energies around 200 MeV or so. The likelihood distributions have an analogous structure with the muons being more evenly distributed across the range than the other particle types.

The usefulness of these statistics is illustrated by placing a cut at some reasonable value and examining the efficiency and mis-identification probability of the resultant sample. For instance, accepting only particles with a significance level for the muon hypothesis of at least 5% gives a 95% efficiency for muons and a 61% efficiency for pions. With the cut at 10%, the muon efficiency is 88% and the pion efficiency is 53%. In practice however, these statistics are probably combined with those from other detector systems to produce an enhanced selection algorithm. The contribution from the EMC to muon identification is expected to be particularly important at energies intermediate to the DIRC and the IFR.

3.6 Chapter Summary

A procedure has been developed and implemented which provides muon identification using the BABAR EMC. The emphasis of this chapter has been on understanding the various steps required, from studying the behaviour of different particles in CsI through to producing discriminating statistics for physics analysts to use. The algorithm will be refined in the future using more up to date Monte Carlo data as well as real data from the experiment. It will also be necessary in time to provide parameterizations for all particle types, rather than just muons, to allow use of likelihood ratios for this discriminating variable. The important point though is that this procedure is now established and ready for use.

Chapter 4

Calibration of the EMC Using Minimum Ionizing Particles

4.1 Introduction

As with most measuring devices, electromagnetic calorimeters must be calibrated. The BABAR EMC is no exception and the raw data it produces must go through several stages of correction before being considered worthy of a high level physics analysis. This chapter will begin by reviewing the various methods of calibrating the EMC and then describe in detail the method of using minimum ionizing particles (MIPs) for providing single crystal calibrations.

4.2 Calibration of the EMC

There are three distinct levels of calibration that raw electronic data read out from the EMC must undergo before being associated with the energy of a physical particle. Firstly there is the electronics calibration. This uses a charge injection system to

linearize the response of the front end electronics over all four amplification ranges of the ADC cards. It operates to a precision of better than 0.1% [38]. Next comes the calibration of individual crystals within the calorimeter. The aim here is to calibrate to the actual energy deposited within the crystal by a particle. Between scintillation of the CsI and light collection by the photodiodes, energy can be lost since no crystal is a perfect light transmitter. Two of the crystal calibration methods will be discussed below. The radioactive source system is part of the mechanical design of the EMC and non-radiative Bhabha events are an example of a colliding beam physics process that can be used for calibration.

Even after electronics and single crystal calibrations, we still do not arrive at the true energy lost by a particle traversing the EMC. The final stage is to calibrate a cluster of crystals to the true energy of the particle that created that cluster. Energy is leaked due to cracks in between crystals and the finite extent of the EMC, both radially and in polar angle. So despite the fact that the crystal energies are now correct (at least in principle!), their sum still does not represent a true particle energy until this so called 'global' calibration is performed. The method adopted here is to use events with well known constraints to derive 'true' energies to scale to. The two main, established techniques will be discussed in what follows.

4.2.1 Crystal Calibration: The Radioactive Source

This consists of thin tubing passing in front of all crystals and carrying a fluorine-containing fluid. The fluorine is activated by an external generator producing neutrons of a few MeV and then decays via $^{19}F(n,\alpha)^{16}N$. The β decay of ^{16}N to ^{16}O with a half life of $\sim 7\,\mathrm{s}$ decays 69% of the time to an excited state which releases a 6.13 MeV photon [47]. This absolutely known energy can then be used to calibrate all crystals and provide a readily-determined low-energy point on the photon response curve.

4.2.2 Crystal Calibration: Non-Radiative Bhabha Events

Colliding beam events where $e^+e^- \rightarrow e^+e^-$ have a sufficiently high yield that they can be used to provide intercalibration of crystals. They also provide an overall scale at the highest possible energies experienced in BABAR. The algorithm is one originally implemented by CLEO and involves the formation of the χ^2 function

$$\chi^2 = \sum_k (\sum_i c_i \epsilon_i^k - E^k)^2 / (\sigma^k)^2 \tag{4.1}$$

where the c_i and ϵ_i are correction factors and measured energies respectively for individual crystals [48]. The energy of the Bhabha positron or electron is E^k and can be derived once the angle of the particle with respect to the beam axis is known. The error on this measurement is added to the calorimeter resolution to give σ^k. Thus, through kinematic constraints these events can be used for single crystal calibration. At design luminosity, it will take less than twelve hours to collect enough data to calibrate with an accuracy of 0.25% per crystal.

4.2.3 Cluster Calibration: Radiative Bhabha Events

For the class of events where $e^+e^- \rightarrow e^+e^-\gamma$, there are enough kinematic constraints to use the photon for energy calibration [49]. The momentum of the final state electron and positron must be well measured by the drift chamber and the angular position of the photon cluster by the calorimeter. Once these quantities are known along with the total energy and momentum of the event, a scale factor for cluster $\rightarrow$ photon energy corrections can be derived. In reality, this factor is more complicated than a single constant and takes energy and polar angle into account. To achieve this, the event sample is binned in these two variables in order to produce a correction function which is energy and θ dependent. At design luminosity, it will take less than two weeks to calibrate the energy response of a crystal ring to 0.25%.

4.2.4 Cluster Calibration: π^0 Events

Global calibration with π^0 events is expected to compliment that from radiative Bhabhas which should provide calibration from a few GeV down to about 500 MeV. The $\pi^0 s$ should cover the range from about 1 GeV down to the cluster cut-off energy at 20 MeV. The lower limit is uncertain as the method will suffer from background which increases rapidly at the lowest energies. This is from both fake photons within the event and beam background. The idea is to use the π^0 mass constraint to adjust photon energies until the mass peak is in the correct place. The adjusted energy, E_{true} is then related to the measured energy, E by

$$E_{true} = Ee^{C_0+C_1 \ln E+C_2(\ln E)^2+C_3 \cos\theta+C_4(\cos\theta)^2} \tag{4.2}$$

where the C_i are coefficients derived in the calibration procedure and θ is the polar angle of the cluster centroid [50].

4.3 MIP calibration

It is possible to provide an absolute energy scale for each crystal individually by using minimum ionizing particles. Since the energy deposit in the EMC of a MIP peaks at around 200 MeV, this method provides a useful point on the energy dependent calibration curve in between those from the radioactive source and Bhabha events. In fact this is also an important energy regime for physics analysis since many of the photons from π^0s in B decays are at energies of a few hundred MeV (e.g. the energy spectrum for photons from the process $B^0 \to \rho^\pm\pi^\mp, \rho^\pm \to \pi^\pm\pi^0$ peaks at ~ 100MeV).

So far this calibration has been carried out with cosmic ray muons, before the detector was in a colliding beam environment. Now that there is real beam data, the next step will be to use $e^+e^- \to \mu^+\mu^-$ events in a similar way. The remainder

of this chapter will be dedicated to describing the work to date using this method of calibration. This will include a description of the technique used and results gained with cosmic ray events. The study and subsequent analysis of dimuon events is future work and thus will not be covered in this chapter.

4.3.1 Overview

The principle here is based on the fact that a MIP has a characteristic $\mathrm{d}E/\mathrm{d}x$ signature in CsI (as described in section 3.3). At the dip of the Bethe-Bloch curve, a muon has a mean energy deposition of 5.6 MeV/cm through ionization. Of course, there are fluctuations around the mean value and these are rather well described by the Landau distribution, which is discussed in appendix B. So, from the Bethe-Bloch curve it is possible to estimate the energy loss for a muon of a given momentum for a certain pathlength in CsI. To estimate the length of active material in the EMC that a given muon will pass through necessitates some kind of extrapolation from the track that the particle left in the drift chamber.

However, extending the track is not as simple as a pure geometrical extrapolation. The particle will lose energy as it passes through the CsI and other material and will change its trajectory according to the effect of the solenoidal B-field within the detector. The best way to take account of magnetic field and material effects in this case is to 'swim' the track through the calorimeter. This involves taking small steps (of say $\sim$ 1cm) to extend the track taking into account any energy loss and resulting change in trajectory at the end of each step before starting the next one. The energy loss of the individual steps can then be summed to derive a predicted energy loss for a single crystal or a collection of crystals.

4.3.2 Tracking and Kalman Extension

The way the muon calibration has been implemented involves using the `SwimTracks` software package to correctly handle the track extrapolation. Before the swimmer is used, the track already has valid parameters out to the end of the DIRC region so that the extrapolation starts just before the EMC is entered. At present charged track construction within BABAR is carried out in the following steps:

1. Find tracks within the DCH
2. Add hits to the DCH tracks by extrapolating back into the SVT
3. Use SVT track finding for low p_t tracks
4. Kalman fit the SVT-only tracks
5. Kalman fit the merged tracks [1]

Extrapolation through the DIRC region is carried out later in the reconstruction chain, at the point where the DIRC needs to know the angles of tracks crossing its quartz bars. This process involves use of the Kalman filter to accurately extend the tracks through the material present in the DIRC region and account for the corresponding energy loss and change in trajectory encountered there.

So by the time the MIP calibration code is run, there should be a list of tracks each with a valid fit out to the start of the EMC. An important point to make now is why the Kalman filter has not been chosen to extend the tracks through the EMC as is done for the DIRC. The Kalman algorithm can only reliably extend tracks through relatively thin materials (e.g. the DIRC has 1.7 cm of quartz as active material). The helix parameters for a given track are only updated after passing through an entire element of simulated material. 'Element', in this context means an indivisible

[1] The Kalman Filter track fitting algorithm and its implementation in the BABAR software framework is described in [51] and references thereof.

piece of a certain subdetector, e.g. the EMC is represented in the code as 6580 crystals, each of which is a detector 'element'. An EMC element is certainly not thin as far as Kalman extension is concerned and the result is large discontinuities in the extrapolated trajectory due to the approximate way that the track parameters are interpolated between subsequent material intersection points.

One can imagine solutions to this problem. The whole geometry implementation code could change to simulate the EMC with a finer granularity, or the Kalman filter could be modified to be intelligent about subdividing material volumes to gain better fit precision. However, neither of these solutions were viable at the time when the MIP calibration was being developed. It is not desirable to change the EMC geometry within the reconstruction code from its current format - which is the most sensible and realistic. Maybe the Kalman filter implementation within BaBar will change to accommodate thick chunks of material in the future but this has never been a high priority, the real solution is a swimmer.

4.3.3 The `SwimTracks` Algorithm

The software that was written to handle the problem of track extension through thick materials in the BaBar detector is called `SwimTracks`. It is used by the MIP calibration code in order to predict energy deposits in EMC crystals as well as by the IFR reconstruction in matching DCH tracks to RPC hits. The procedure for using the swimmer will now be described.

First one creates a `SwimTrack` specifying some initial parameters such as position, direction, momentum, particle type and charge. The `SwimTrack` is then used to create a `SwimThruDetElem` object which actually performs the track extrapolation. It is also necessary to provide a description of the relevant subdetector geometry (a `DetSet`) along with a `SwimEngine` which specifies the swimming algorithm and a `SwimContext` which defines certain parameters of the swim. The currently used

implementation of the `SwimEngine` is `SwimRKEngine`. This adds straight line segments to the existing trajectory, taking into account the effects of material and the magnetic field as it goes. A fourth order Runge-Kutta algorithm [52] is used to accurately calculate the projected position and momentum at the end of each step. The final result is a list of `SwimDetElemHit` objects, one for each crystal traversed. These carry information such as the pathlength and energy deposited in a single element.

4.3.4 Calibration Using Cosmic Ray Muons

The initial single crystal calibration of the EMC was done in early 1999 using muon candidates from cosmic rays before the detector recorded any colliding beam data. The detector then had a complete IFR, drift chamber and EMC as well as a partial DIRC. The solenoid was also in place and some runs were taken with the field on and others with the field off. It was decided that cosmics would be a good starting point for calibrating the calorimeter, in the absence of real e^+e^- events. There were two calibration data sets, one taken up to February 1999 and the other in April and May 1999. These were used to help provide an initial calibration of the EMC. The detector started taking colliding beam data at the end of May.

In a non-beam environment it is relatively easy to select cosmic ray events since almost everything that leaves a convincing track in the drift chamber is a muon. The tracking reconstruction correctly handles this situation by splitting the track into two pieces and using timing information to assign direction and pathlength along the tracks accordingly. Both tracks can then be used for extrapolation through the EMC to provide predicted energies for the crystals which they traverse. The swimmer must be told when a particular track is incoming rather than outgoing so that it is extrapolated backwards and energy changes are incremented rather than decremented. In the cases where the magnetic field in the detector is off, the

swimmer is passed a zero field and the initial momentum is set to the nominal value of 4 GeV/c. This is not an entirely unreasonable starting value since the cosmic momentum spectrum as seen by the drift chamber extends to very high values as can be seen in figure 4.1. The falloff towards zero is due to the fact that such low momentum tracks often fail to be reconstructed due to them leaving too few hits in the chamber or perhaps not passing close enough to the origin.

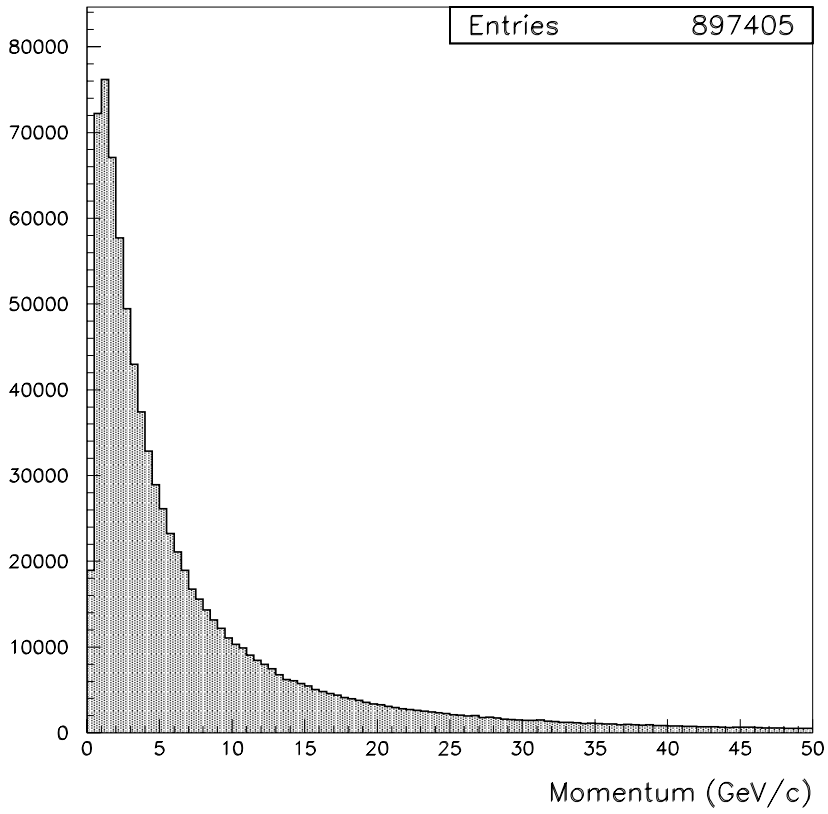

Figure 4.1: *The momentum spectrum for cosmic ray muons as measured by the BABAR drift chamber.*

4.3.5 Accumulation of Data

In order to generate calibration constants for as many calorimeter crystals as possible it was necessary to process several million cosmic events. This necessitated a pared down version of the reconstruction code in order to analyze the events as quickly as possible. Therefore only DCH reconstruction, EMC clustering and track-cluster matching was carried out before the calibration code was run. The extraction of calibration information then proceeds as follows:

1. Assign clusters to tracks on the basis of the already derived matching information
2. Swim each track through the calorimeter producing a list of hit crystals
3. For each crystal find the corresponding measured energy from the cluster
4. Store the measured and predicted energies for each crystal along with other useful information

Once this data has been accumulated for all available, usable runs, it is analyzed in PAW via ntuples to determine the necessary correction factor for each crystal.

4.3.6 Swimmer Performance

In order to have confidence in the `SwimTracks` extrapolation it was necessary to carry out some performance tests to check that it was behaving as expected. Plots which compare the predicted energy to the MC truth energy are shown in figure 4.2. The aim is to show that the swimmer's estimate of deposited energy is reliable. The MC events used were cosmic ray muons generated via the BEGET event generator [54]. The simulated momentum spectrum has a functional form of $1/p^2$ for momenta between 1 GeV/c and 1000 GeV/c. Another way to visualize the accuracy

of the swimmer is to plot points along the extrapolated trajectory and compare them to where the simulated particle really went. `SwimTracks` provides 3D position information at the entrance and exit point of each crystal traversed. The GEANT simulation of the detector provides one 'G-hit' per crystal. These G-hits are always associated with a position corresponding to 0.5 cm inside the crystal, along the particle trajectory. Thus we can get an idea of the accuracy of the extrapolation by putting all these points together on one plot. Some examples are shown in figure 4.3 as a projection on to the x-y plane of the detector coordinate system. The top two plots show typical simulated cosmic tracks of different momentum which have been accurately imitated by the swimmer. Note that there are two swimmer hits for each crystal, an entrance and an exit point, whereas there is only one GEANT hit per crystal, offset from the true entrance point by 0.5 cm. The bottom left plot is an example of when the drift chamber has found a complete two-track cosmic event and the swimmer has extrapolated correctly in both directions. The bottom right plot shows a less accurate extrapolation, perhaps where the initial direction of the track at the start of the EMC was wrong. However, even in a case like this, the crystal energy deposit predictions should still be quite reliable.

There are of course intrinsic sources of error in this method which mean that the swimmer is not expected to get it right every time. Therefore it is more realistic to check that the track extrapolation is reasonably accurately *on average*. The main contributions to any fluctuation about this average are then multiple scattering of the particle as it passes through detector material and the measurement resolution of say, the drift chamber in determining the initial track direction.

4.3.7 Derivation of Calibration Constants

Once satisfied that the swimmer is doing as good a job as can be expected, the next step is to derive the calibration constants by fitting to the distribution of measured

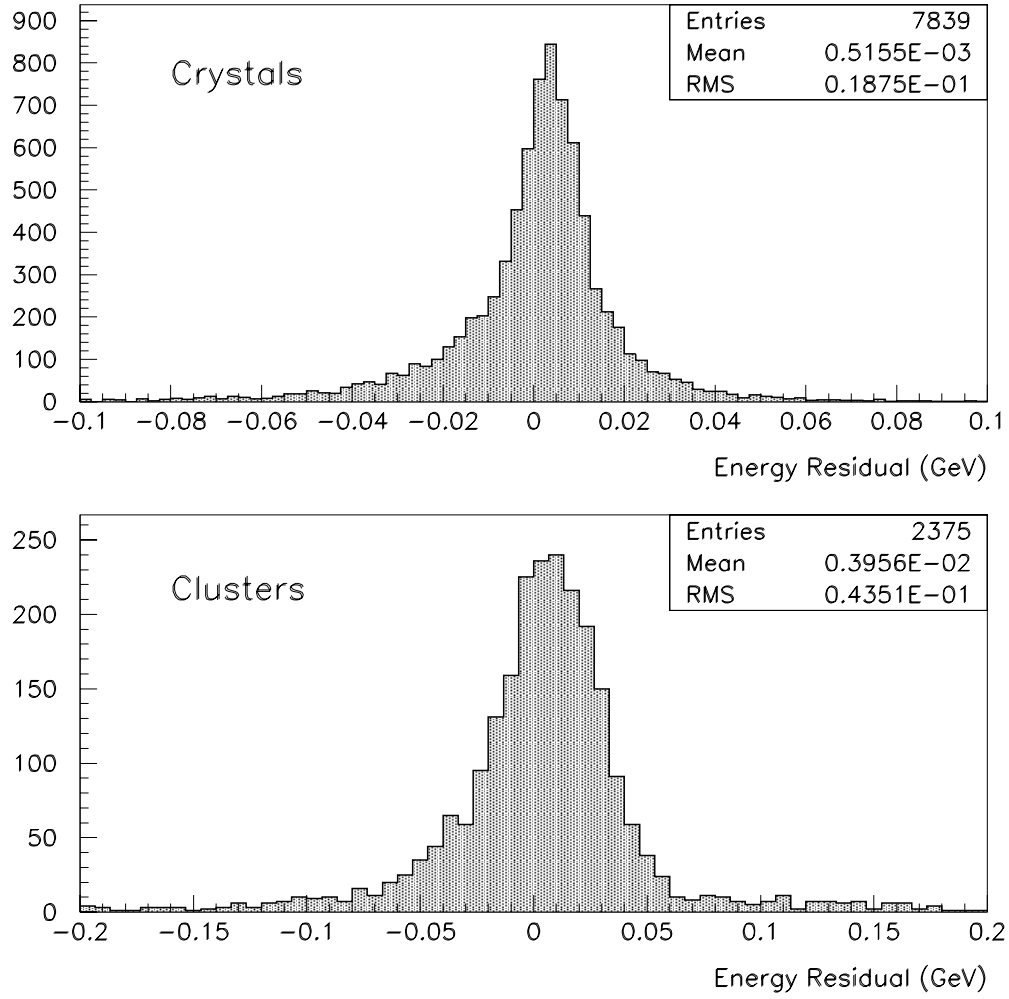

Figure 4.2: *Plots of predicted energy minus MC truth energy for single crystals (top) and clusters (bottom). The shape in each case is asymmetric with the peak slightly above zero. This is expected since for each data point the MC truth energy is from a Landau distribution and the predicted energy is from the mean of a Landau distribution.*

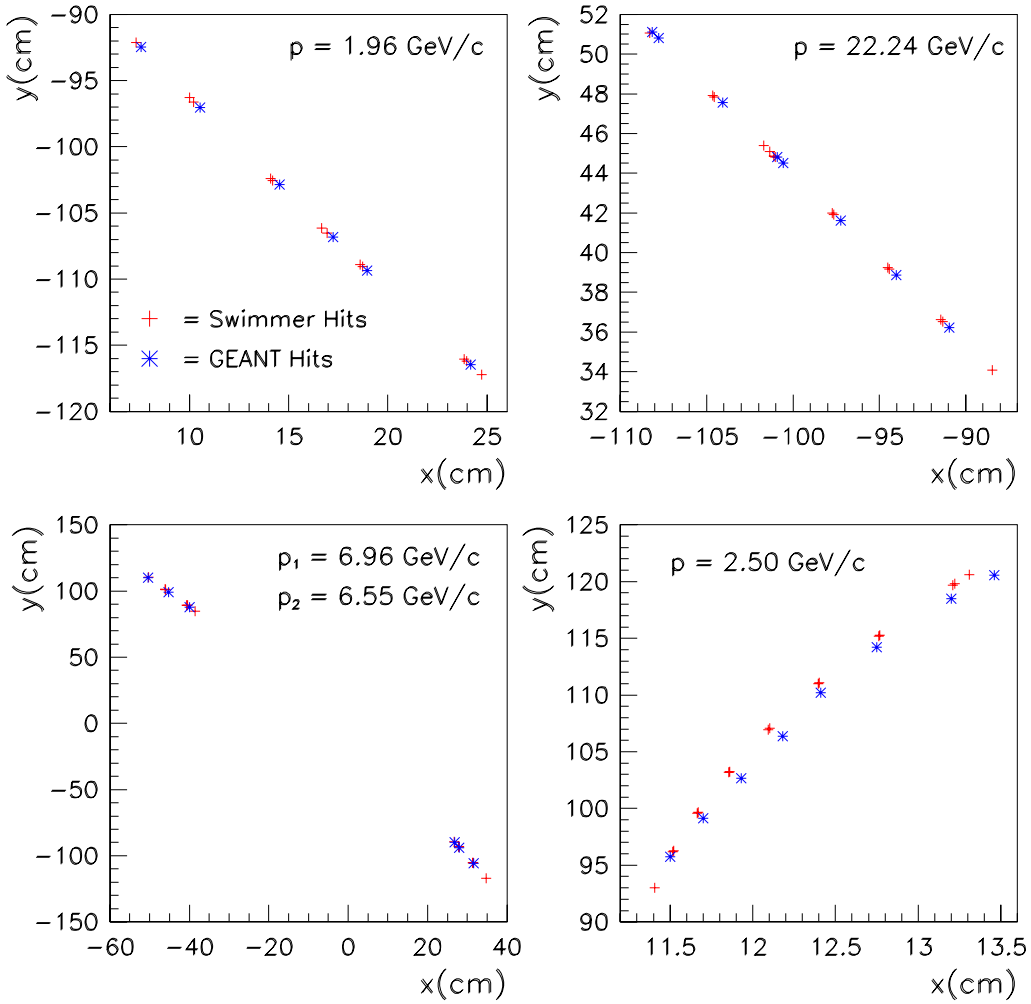

Figure 4.3: *Plots comparing the* `SwimTracks` *extrapolation to GEANT hits of cosmic ray muons in the EMC. The projection shown is that of a cross-section through the detector, perpendicular to the beam-line. The centre of the detector is at (0,0).*

energy divided by predicted energy for each crystal individually. The fitting function found to be most useful and versatile for this purpose with the cosmic data was the Gaussian plus Breit-Wigner lineshape as described in the previous chapter. After fitting, the position of the peak of the Gaussian part of the function - which should be a good estimate of the peak of the distribution - is extracted. The calibration constant for that crystal is then just the inverse of this number, that is the scale factor which will shift the peak to one.

Before making the energy ratio plot, both the measured and predicted energies were required to be less than 1 GeV. In addition, the measured energy was required to be at least 20 MeV to reduce the effect of low energy noise in the calorimeter. The ratio was then formed for the range $0 < E_{meas}/E_{pred} < 2$ and only crystals with at least 200 events in this plot were considered. After the fit, only results with a χ^2 per degree of freedom of less than 10 and fractional error on the calibration constant of less than 0.1 were kept. Finally, the constants themselves were restricted to lie between 0.6 and 1.7. All these post-fit cuts are aimed at rejecting bad fits and there is probably some degree of correlation between them. With all the above criteria, it was possible to provide calibration constants for 3166/6580 crystals. The rest correspond to dead or noisy parts of the calorimeter that were deliberately excluded as well as low statistics areas and individual crystals that failed one or other of the cuts. Some of the relevant quantities are shown in figure 4.4.

A plot of the (θ, ϕ) index plane for the EMC is shown in figure 4.5. The boxes show the crystals for which a calibration constant was provided from the February cosmic run. The gaps around $\phi = 0$, 60 and 119 correspond to the low flux of cosmics in the horizontal direction.

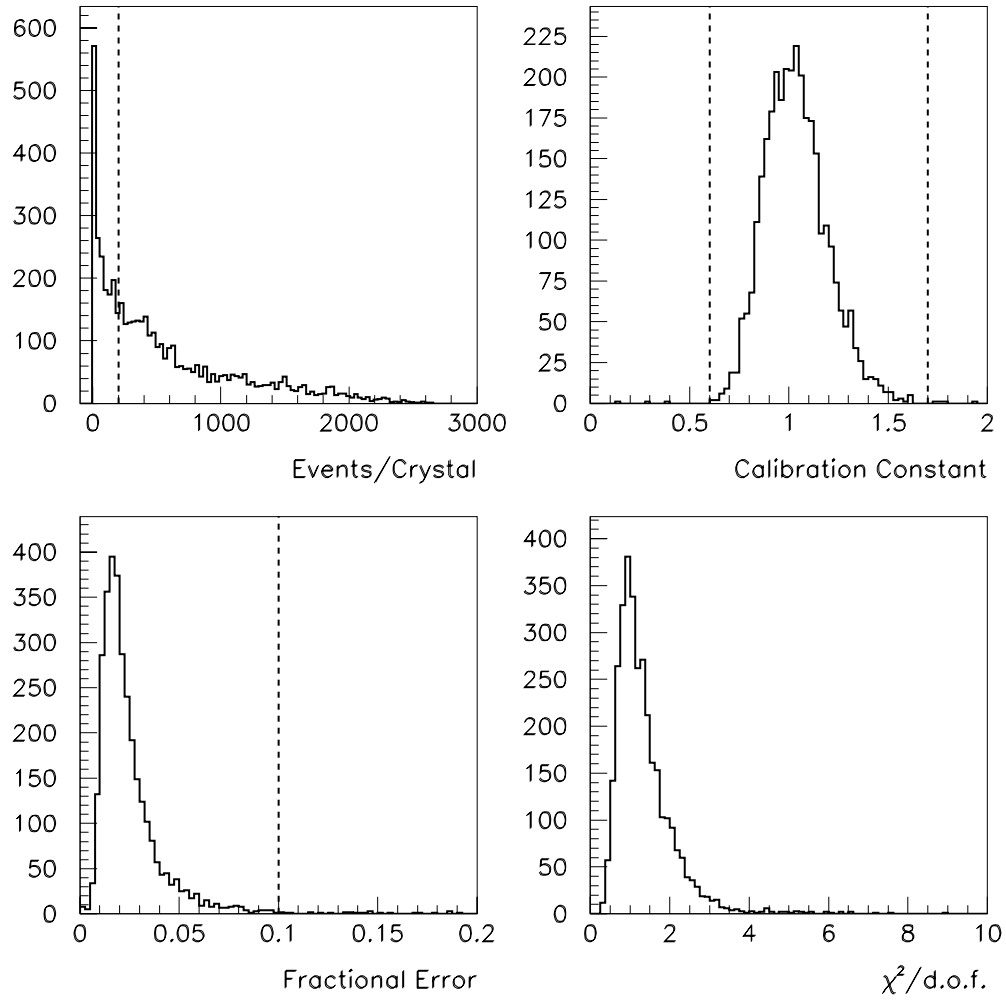

Figure 4.4: *Distributions showing the cuts on the number of events per crystal as well as some quality statistics. The dotted lines represent the cut values. The top left plot does not include crystals for which there were zero events.*

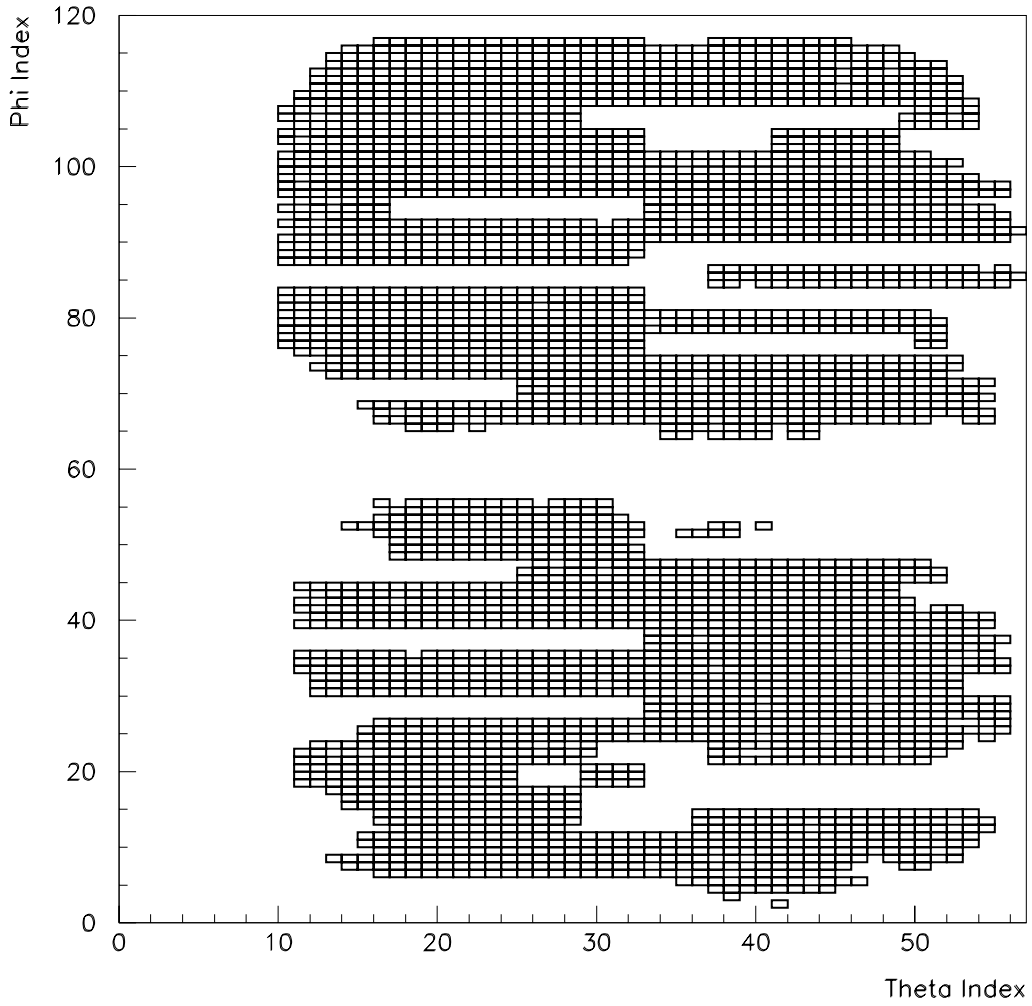

Figure 4.5: *A map of the EMC in terms of θ and ϕ crystal indices. The overall range is $0 < \theta < 56$, $0 < \phi < 119$. The boxes show the crystals for which a calibration was possible.*

4.3.8 Validation of the Calibration Procedure

The fitting used to derive the calibration constants works rather well on the whole. Two example crystals are shown in figure 4.6 where one has low statistics and the other has considerably more events. Both fit well and the estimate of the peak position in these cases can be faithfully taken from the mean of the Gaussian part of the fitting function. To validate the final set of calibration constants it is necessary to see whether the resolution is actually improved when they are applied. The peak of the E_{meas}/E_{pred} distribution should also shift towards one if all is going well. Figure 4.7 shows E_{meas}/E_{pred} before and after the calibration has been applied. After fitting the central region with a Gaussian it was found that the peak shifts in the right direction and also that the resolution improves slightly. However, it should be noted that the peak was still broader than expected after the calibration was applied. In retrospect it has been agreed that the most likely cause of this is a problem with the EMC readout electronics which was only discovered after this analysis was performed.

4.3.9 Systematic Effects

There is a systematic subtlety here which needs some consideration. The predicted energy provided by the swimmer comes from Bethe-Bloch curves, which represent the mean energy loss for a given particle in a given material. We know however, that the Landau distribution is not symmetric and therefore has its mean shifted with respect to its peak[2]. Thus forming the ratio of measured energy to predicted energy in this case is in some sense like dividing a Landau distribution by its mean.

[2]This is slightly misleading since the Landau distribution extends from zero to positive infinity and therefore does not have a mean, as such. Instead, in the practical case being discussed here one should think of the mean as that of a truncated Landau distribution with the cut off placed at some suitably high value.

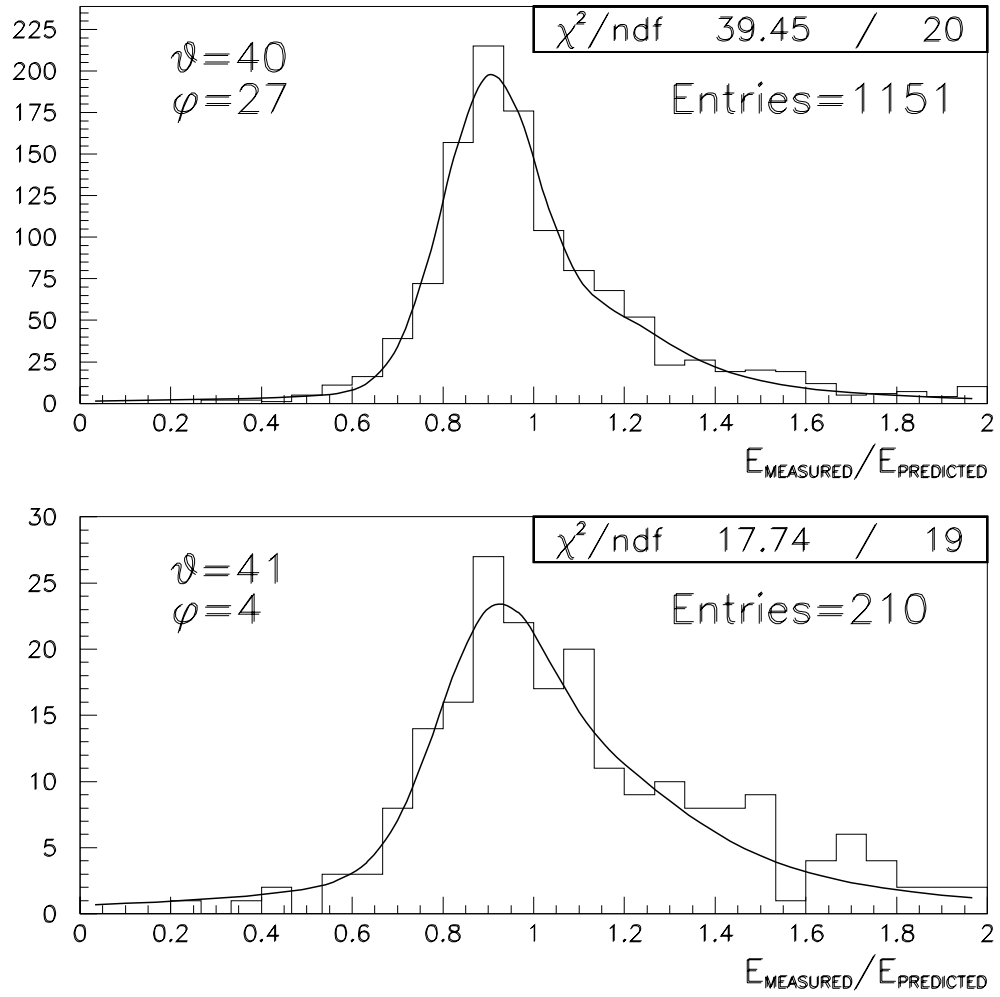

Figure 4.6: *Examples of high and low statistics fits to single crystal energy ratio distributions. The upper plot is for the crystal identified by θ,ϕ indices 40,27 and the lower plot is for crystal 41,4.*

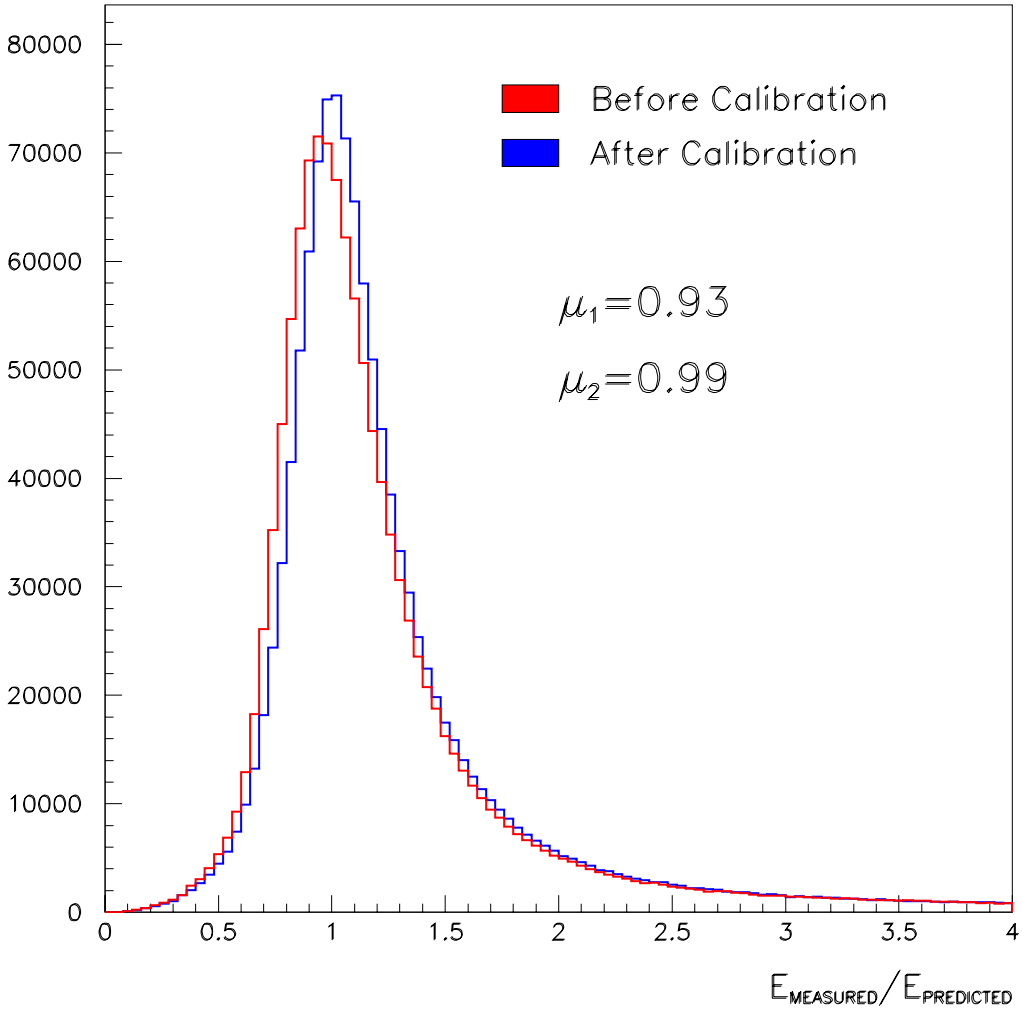

Figure 4.7: *The ratio of measured to predicted energy for all crystals with a calibration constant, before and after calibration. Fitting the region around the peak with a Gaussian shows that the mean μ gets closer to one and the width improves from 16.3% to 15.6%.*

The resultant distribution for a *perfect* crystal would have a peak position below one by some fixed amount and in fact the *mean* would be at one. This suggests that either shifting the peak of the energy ratio distribution to one is not the correct thing to do or that some correction must be applied somewhere to allow for this systematic shift. The ideal solution would probably be to shift the *mean* rather than the peak of the distribution to one. However, this method is fraught with experimental complications. For the very first data taken by the detector especially, we are unsure of background and noise levels and it is uncertain how these factors affect the width of the peak. Coupled with the asymmetric and broad nature of the distribution for this first data set, this makes the mean a much less reliable quantity than the peak position. In addition it would be difficult to know with any confidence where to place the cut-off from which a truncated mean could be calculated.

In the future, the best solution may be to scale the predicted energies before forming the ratio. For the first analysis however, the peak versus mean discrepancy was ignored for the main part of the calibration procedure. Only afterwards was a study done to examine the systematic introduced by calibrating using the peak. The method involved using the analytic form of the Landau distribution as in appendix B with

$$(\Delta E)_{mp} = \xi \left[\ln \left(\xi \frac{2m_e\beta^2}{I^2(1-\beta^2)} \right) - \beta^2 + 0.198 \right], \tag{4.3}$$

to determine the magnitude of the shift between the mean and the peak of the distribution for different momenta and pathlengths. Figure 4.8 shows the main results of this study. It turns out that the difference between the mean and the peak scales proportionally with pathlength through the crystal and stays fairly constant over a wide range of momenta. Taking the mean $\mathrm{d}E/\mathrm{d}x$ of a minimum ionizing muon in CsI to be 5.6 MeV/cm, the systematic so introduced here is estimated to be at the level of 7%. That is, the calibration constants produced from the first batch of cosmic data are high by about 7%.

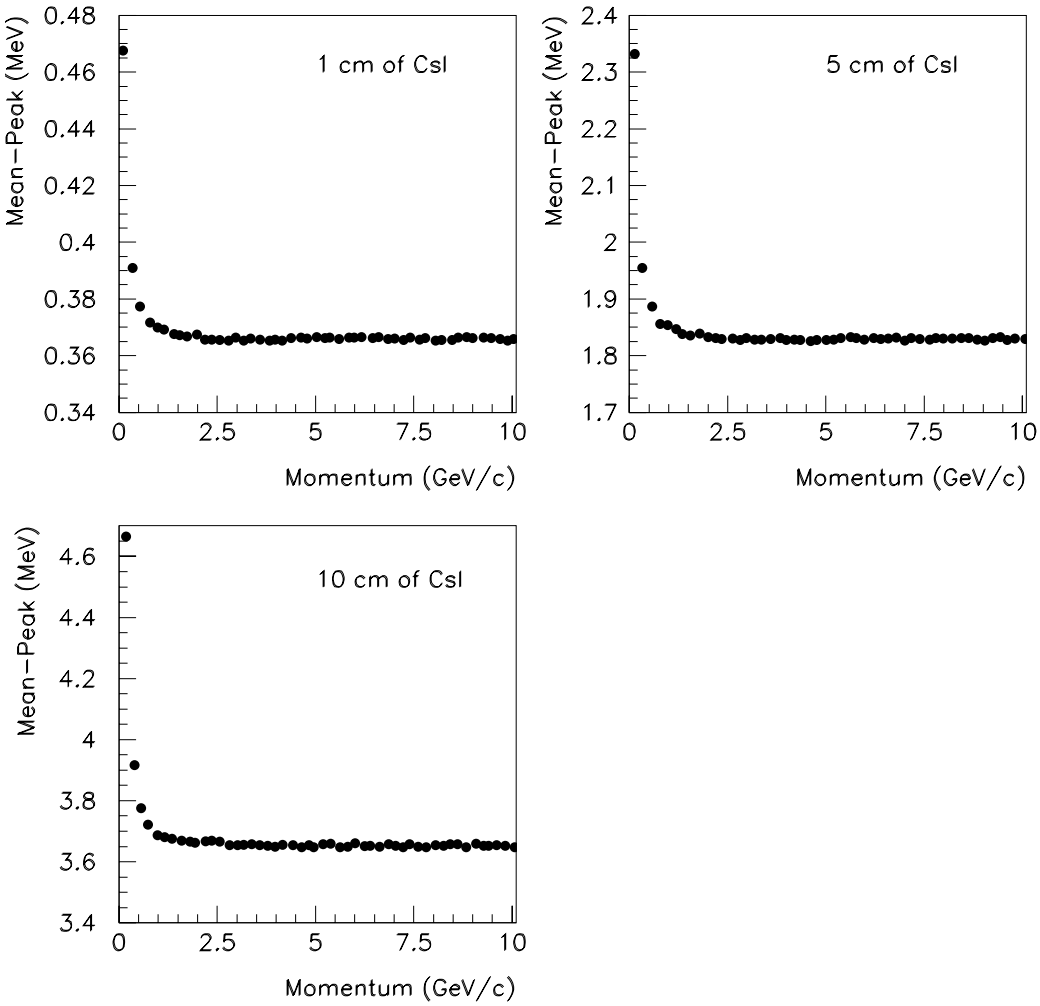

Figure 4.8: *The difference between the mean and the peak of the analytic form of the Landau distribution as a function of particle momentum. The effect seems to be pretty much constant with momentum and scales linearly with pathlength.*

4.4 Chapter Summary

This chapter is an account of the preliminary calibration of the BABAR EMC at the level of individual crystals. Since the work described here was carried out there have been several more iterations, with the calorimeter performance gradually improving over time with better calibrations. Once beam data was available, a non-radiative B-habha sample was obtained and also the radioactive source has been used to provide accurate per-crystal calibration constants. At the level of clusters, the π^0 calibration is currently the preferred method since hadronic data has been available for some months now. In one sense, these other techniques supercede the muon calibration in that they were always going to be those used to calibrate the detector once the first batch of beam data was available. However this is not the end of the story since the MIP calibration will soon be exercised on μ-pair events from the real data set. This will provide an important point on the energy dependent calibration curve for physics studies, bridging the gap between the low energy radioactive source and the high energy Bhabhas. The work done to date on this method has therefore been highly useful in establishing and understanding the technique which will be used for many years hence.

Chapter 5

Analysis of $B^0 \to J/\psi K^{*0}$ Decays

5.1 Introduction

As mentioned in Chapter 1, this decay channel can be used to measure the unitarity triangle angle β through the neutral decay mode of the K^{*0} where $K^{*0} \to K^0_s \pi^0$. There are complications however, due to the fact that scalar $\to$ vector-vector decays lead to a final state which is an admixture of *CP* even and *CP* odd. Theoretically, this provides no additional problem in extracting $\sin 2\beta$ but it does add an extra experimental complication. An analysis of the angular distributions of the vector mesons' decay products is necessary in order to cleanly extract *CP* violation information.

On the practical side, with the data accumulated to date from BABAR it is possible only to do a preliminary $B \to J/\psi K^*$ analysis. The emphasis here is on selection of the final state particles and combining them to fully reconstruct a neutral B meson. The yield of Bs in such an analysis then allows an initial measurement of the $B^0 \to J/\psi K^{*0}$ branching ratio. The latest measurement of this quantity is from CLEO [56] who found it to be $(1.32 \pm 0.17 \pm 0.17) \times 10^{-3}$. The particle data group [5] combined value is $(1.35 \pm 0.18) \times 10^{-3}$.

5.2 How to Measure CP Violation in $B^0 \to J/\psi K^{*0}$

The starting point here is section 1.7.3 and in particular equation 1.99. The dilution factor D stands in the way of a clean, direct measurement of $\sin 2\beta$ in this channel and must be taken into account. This is generally done by analyzing the angular distributions of the vector meson decay products. Since these depend on the mixture of different orbital angular momenta in the vector-vector system, it is possible to use them to determine the relative amounts of CP-odd and CP-even in the final state. There are two general ways to make use of this feature. The first, typically the way theorists think about the problem, involves isolating a particular CP contribution by performing a weighted integral over the data and then looking for β by fitting to the projected quantity. A more experimentally-oriented approach is to use a maximum-likelihood method to simultaneously fit for β and the chosen angular analysis basis amplitudes. The various sets of basis amplitudes which are useful for this purpose will now be discussed.

5.3 Angular Analysis

The decay amplitudes for this process are in general time-dependent but in an appropriate basis, the angular dependence and time dependence factorize, greatly facilitating this study. There are three different angular momentum projections that can be used in this $B \to V_1 V_2$ type of decay: the helicity basis, the transversity basis and the partial wave decomposition. They are all completely equivalent but quantities defined in these basis states have different physical interpretations, and therefore lead to slightly different physical insights about the underlying process. The angular analysis necessary for extraction of CP information in this channel will be described below but is also well detailed in [55].

5.3.1 The Helicity and Transversity Formalisms

The helicity basis defines three amplitudes A_λ, ($\lambda = 0, \pm 1$) which correspond to the helicity of the V_1 or V_2 in the $B \to V_1 V_2$ decay. In the transversity basis, A_0 remains unchanged and the other two amplitudes are defined as the following linear combinations of the helicity amplitudes [57]:

$$A_\parallel = \frac{1}{\sqrt{2}}(A_{+1} + A_{-1}) \qquad A_\perp = \frac{1}{\sqrt{2}}(A_{+1} - A_{-1}). \tag{5.1}$$

It will be seen later that $A_\parallel$ corresponds to transverse polarization parallel to the plane of the other decay and $A_\perp$ to transverse polarization perpendicular to that plane. While the helicity formalism allows a straightforward determination of the longitudinal rate, the transversity formalism is convenient for determination of the *CP*-odd component of the decay rate.

5.3.2 The Partial Wave Decomposition

It is also possible to expand the helicity amplitudes (and therefore the transversity amplitudes as well) in terms of partial waves corresponding to the possible S, P and D orbital angular momenta of the V_1,V_2 system. The decomposition is readily obtained from the Clebsch-Gordan coefficients for a combination of two spin-1 particles:

$$A_{\pm 1} = \sqrt{\frac{1}{3}}S \pm \sqrt{\frac{1}{2}}P + \sqrt{\frac{1}{6}}D \quad , \quad A_0 = -\sqrt{\frac{1}{3}}S + \sqrt{\frac{2}{3}}D. \tag{5.2}$$

Thus, from equations 5.1

$$A_\parallel = \sqrt{\frac{2}{3}}S + \sqrt{\frac{1}{3}}D \quad \text{and} \quad A_\perp = P. \tag{5.3}$$

Here it can be seen explicitly that the $(-1)^L$-odd P-wave term is the same as the transversity amplitude $A_\perp$, while the other two transversity amplitudes are combinations of the $(-1)^L$-even S- and D-wave amplitudes.

5.3.3 Time and Angular Dependence

The above relations are valid for any time t. To make the time dependence explicit, it is convenient to work in the transversity basis, where each amplitude contributes to only one *CP* eigenstate. Then it turns out that (see equation 1.42)

$$\begin{aligned} A_0(t) &= A_0(0)e^{-iMt}e^{-\Gamma t/2}\left(\cos\frac{\Delta m t}{2} + i\eta\lambda_f \sin\frac{\Delta m t}{2}\right) \\ A_\parallel(t) &= A_\parallel(0)e^{-iMt}e^{-\Gamma t/2}\left(\cos\frac{\Delta m t}{2} + i\eta\lambda_f \sin\frac{\Delta m t}{2}\right) \\ A_\perp(t) &= A_\perp(0)e^{-iMt}e^{-\Gamma t/2}\left(\cos\frac{\Delta m t}{2} - i\eta\lambda_f \sin\frac{\Delta m t}{2}\right) \end{aligned} \tag{5.4}$$

where $\lambda_f = \frac{q}{p}\frac{\overline{A}(f)}{A(f)}$ and the *CP* of the final state is $\eta_f(-1)^L$, where η_f is the intrinsic *CP* and L is the partial wave of the V_1,V_2 system. In this case $\eta(J/\psi(K_S\pi^0)_{K^*}) = +1$. The $(-1)^L$ factor is manifest in these equations and is responsible for the minus sign in the expression for $A_\perp$. From these equations, one can deduce the corresponding expressions in the helicity or partial wave basis.

The amplitudes for the *CP* conjugate decay of $\overline{B}^0(t)$ into the final *CP* eigenstate f are

$$\begin{aligned} \overline{A}_0(t) &= \eta\overline{A}_0(0)e^{-iMt}e^{-\Gamma t/2}\left(\cos\frac{\Delta m t}{2} + i\eta\lambda_f^{-1} \sin\frac{\Delta m t}{2}\right) \\ \overline{A}_\parallel(t) &= \eta\overline{A}_\parallel(0)e^{-iMt}e^{-\Gamma t/2}\left(\cos\frac{\Delta m t}{2} + i\eta\lambda_f^{-1} \sin\frac{\Delta m t}{2}\right) \\ \overline{A}_\perp(t) &= -\eta\overline{A}_\perp(0)e^{-iMt}e^{-\Gamma t/2}\left(\cos\frac{\Delta m t}{2} - i\eta\lambda_f^{-1} \sin\frac{\Delta m t}{2}\right). \end{aligned} \tag{5.5}$$

Now it is useful to write down the angular distribution for this decay, in order to show how study of decay angles can allow determination of separate helicity/transversity amplitudes. For the helicity frame, the conventions as shown schematically in figure 5.1 are adopted.

If $\mathbf{p}_1$ is the three-momentum of the K_S in the K^{*0} rest frame, $\mathbf{p}_2$ is the three-momentum of the l^+ in the J/ψ rest frame, $\hat{v}$ is the unit vector along the direction of flight of the K^{*0} and $\hat{c}(\hat{d})$ is the unit vector along the projection of $\mathbf{p}_1(\mathbf{p}_2)$ orthogonal

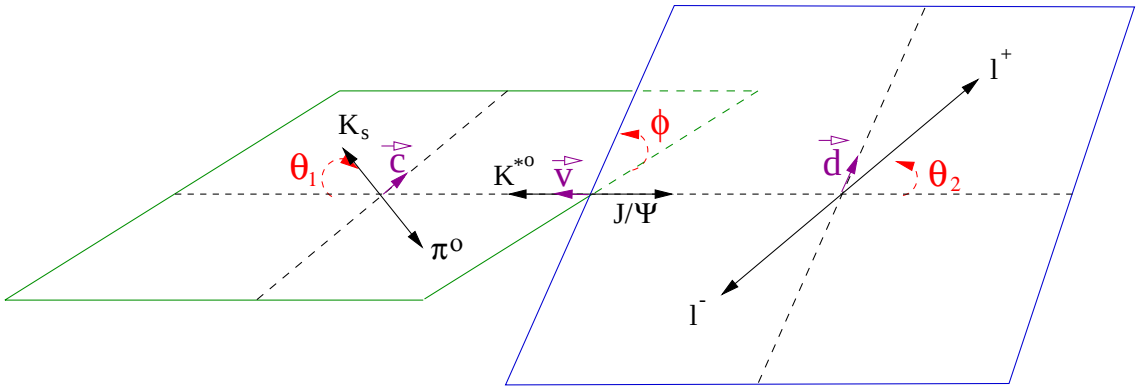

Figure 5.1: *The helicity frame for* $B \to J/\psi K^* \to l^+ l^- K\pi$.

to $\hat{v}(-\hat{v})$, then one can define

$$\begin{array}{lllllll} \cos\theta_1 & = & \hat{v}\cdot\mathbf{p}_1/\mid\mathbf{p}_1\mid & \cos\theta_2 & = & -\hat{v}\cdot\mathbf{p}_2/\mid\mathbf{p}_2\mid \\ \cos\phi & = & \hat{c}\cdot\hat{d} & \sin\phi & = & (\hat{c}\times\hat{v})\cdot\hat{d} \end{array} \tag{5.6}$$

Then the three helicity angles are the polar angle of the l^+ in the J/ψ rest frame θ_2, the polar angle of the K in the K^* rest frame θ_1 and the angle between the decay planes of the two vector mesons ϕ, which can lie in the range 0 to 2π. Using these basis angles, the full angular distribution for B decay in the helicity formalism can be written as

$$\frac{1}{\Gamma}\,\frac{d^3\Gamma}{d\cos\theta_1 d\cos\theta_2 d\phi} = \frac{9}{16\pi}\,\frac{1}{|A_0|^2+|A_{+1}|^2+|A_{-1}|^2} \tag{5.7}$$

$$\left\{\frac{1}{4}\left(1+\cos^2\theta_2\right)\sin^2\theta_1\left(|A_{+1}|^2+|A_{-1}|^2\right)+\sin^2\theta_2\cos^2\theta_1|A_0|^2\right.$$

$$-\frac{1}{2}\sin^2\theta_1\sin^2\theta_2\left[\cos 2\phi\mathrm{Re}(A_{+1}A_{-1}^*)-\sin 2\phi\ \mathrm{Im}(A_{+1}A_{-1}^*)\right]$$

$$\left.+\frac{1}{4}\sin 2\theta_1\sin 2\theta_2\left[\cos\phi\mathrm{Re}\left(A_{+1}A_0^*+A_{-1}A_0^*\right)-\sin\phi\ \mathrm{Im}\left(A_{+1}A_0^*-A_{-1}A_0^*\right)\right]\right\}\quad .$$

The amplitudes in the above equation depend on time and the angular distribution is normalized at time t. In practice it may be more convenient to normalize to the total rate, integrated over time.

The longitudinal polarization ratio is defined as

$$R_0 = \frac{\Gamma_0}{\Gamma} = \frac{|A_0|^2}{|A_0|^2 + |A_{+1}|^2 + |A_{-1}|^2} \tag{5.8}$$

and the transverse polarization is then just $R_T = 1 - R_0$. To determine this quantity from data, one can integrate over ϕ to produce

$$\frac{1}{\Gamma}\,\frac{d^2\Gamma}{d\cos\theta_1 d\cos\theta_2} = \frac{9}{32}(1-R_0)\sin^2\theta_1(1+\cos^2\theta_2) + \frac{9}{8}R_0\ \cos^2\theta_1\ \sin^2\theta_2 \tag{5.9}$$

and then a one-parameter fit in the $\cos\theta_1 - 9\cos\theta_2$ plane will yield R_0.

The relevant angles for the transversity formalism are shown in figure 5.2. The system is constructed as follows: In the J/ψ rest frame, the momentum $\mathbf{p}_\psi$ defines the x axis; the y axis is in the $K\pi$ plane such that $p_y(K) > 0$; the z axis then follows as for a conventional right-handed coordinate system; $\theta_{\rm tr}$ is the angle between the l^+ and the z axis, and $\phi_{\rm tr}$ is defined as the azimuthal angle between the projection of l^+ on the $K\pi$ plane and the x axis. The third angle is the same θ_1 as for the helicity basis.

It turns out that the K^* linear polarization must lie in the $K\pi$ plane and can be considered to be either longitudinal ($\varepsilon_{K^*} = \hat{x}$) or transverse ($\varepsilon_{K^*} = \hat{y}$). The three transversity amplitudes are then defined by the direction of the polarization of the J/ψ :

$$\begin{array}{lllll} A_0 & : & \varepsilon_{K^*} = \hat{x} & \varepsilon_\psi = \hat{x} & (CP = +) \\ A_\parallel & : & \varepsilon_{K^*} = \hat{y} & \varepsilon_\psi = \hat{y} & (CP = +) \\ A_\perp & : & \varepsilon_{K^*} = \hat{y} & \varepsilon_\psi = \hat{z} & (CP = -)\ . \end{array} \tag{5.10}$$

This reinforces the earlier assertion that $A_\parallel$ refers to transverse polarization parallel to the plane of the other decay and $A_\perp$ to transverse polarization perpendicular to that plane. Just as states of definite helicity are combinations of linear polarization states, the linear polarization states of this vector-vector system are combinations of the helicity amplitudes (compare (5.10) with (5.1)).

The angles in the two bases are related by

$$\cos\theta_2 \quad = \quad \sin\theta_{\rm tr}\cos\phi_{\rm tr}$$

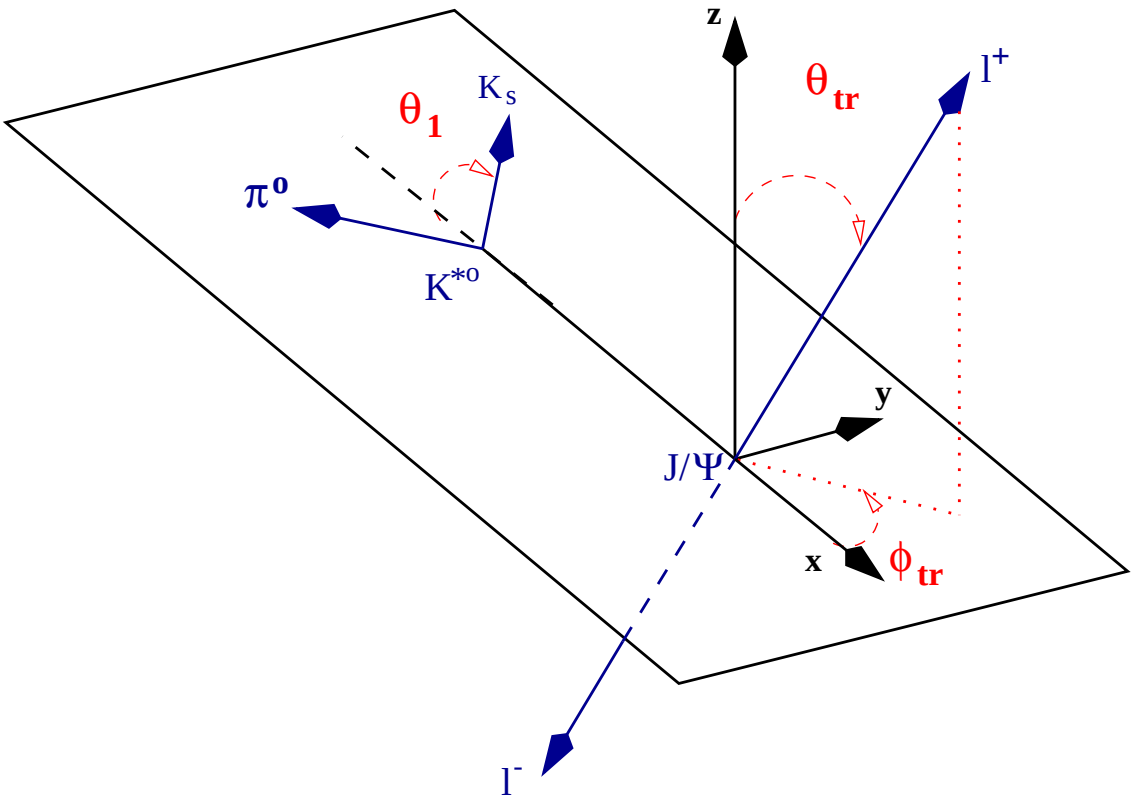

Figure 5.2: *The transversity frame for* $B \to J/\psi K^* \to l^+l^-K\pi$.

$$\begin{aligned} \sin\theta_2 \sin\phi &= \cos\theta_{\rm tr} \\ \sin\theta_2 \cos\phi &= \sin\theta_{\rm tr} \sin\phi_{\rm tr} \end{aligned} \tag{5.11}$$

and so the full angular distribution in the transversity basis is:

$$\frac{1}{\Gamma}\,\frac{d^3\Gamma}{d\cos\theta_{\rm tr} d\cos\theta_1 d\phi_{\rm tr}} = \frac{9}{32\pi}\,\frac{1}{|A_0|^2+|A_\parallel|^2+|A_\perp|^2} \tag{5.12}$$

$$\Big\{ 2\cos^2\theta_1(1-\sin^2\theta_{\rm tr}\,\cos^2\phi_{\rm tr})|A_0|^2 + \sin^2\theta_1(1-\sin^2\theta_{\rm tr}\,\sin^2\phi_{\rm tr})|A_\parallel|^2$$

$$+\sin^2\theta_1\sin^2\theta_{\rm tr}|A_\perp|^2 + \sin^2\theta_1 \sin 2\theta_{\rm tr}\,\sin\phi_{\rm tr}\,{\rm Im}(A_\parallel^* A_\perp)$$

$$+\frac{1}{\sqrt{2}}\sin 2\theta_1 \sin^2\theta_{\rm tr}\sin 2\phi_{\rm tr}\,{\rm Re}(A_0^* A_\parallel) - \frac{1}{\sqrt{2}}\sin 2\theta_1 \sin 2\theta_{\rm tr}\cos\phi_{\rm tr}\,{\rm Im}(A_0^* A_\perp)\Big\}\ .$$

The parity-even ($S+D$ waves) part of the decay is described by $|A_0|^2+|A_\parallel|^2$ while $|A_\perp|^2$ corresponds to the parity-odd (P wave) component. Thus the parity-odd fraction can be defined as

$$R_\perp = \frac{|A_\perp|^2}{|A_0|^2+|A_\parallel|^2+|A_\perp|^2} \quad . \tag{5.13}$$

In order to measure this quantity, one integrates the angular distribution over $\phi_{\rm tr}$ and θ_1 to obtain

$$\frac{1}{\Gamma}\frac{d\Gamma}{d\cos\theta_{\rm tr}} = \frac{3}{8}(1-R_\perp)(1+\cos^2\theta_{\rm tr}) + \frac{3}{4}R_\perp \sin^2\theta_{\rm tr} \tag{5.14}$$

and then $R_\perp$ can be obtained from a one-parameter fit. Such analyses have been done by CLEO [56] for $B \to J/\psi K^*$ yielding

$$R_0 = 0.52 \pm 0.07 \pm 0.04, \qquad R_\perp = 0.16 \pm 0.08 \pm 0.04 \tag{5.15}$$

with relative phases $\varphi(A)$

$$\varphi(A_\parallel) + \pi = 3.00 \pm 0.37 \pm 0.04 \qquad \varphi(A_\perp) = -0.11 \pm 0.46 \pm 0.03. \tag{5.16}$$

where the π comes from the CLEO choice of angle convention and $\varphi(A_0)$ has been chosen to be 0.

It should be noted that there are several decay modes which have this same polarization structure and therefore can contribute to the statistics of the angular distributions for this analysis. While only the $B^0 \to J/\psi K^{*0}(K^0\pi^0)$ *CP* eigenstate mode and its charge conjugate can be used to extract $\sin 2\beta$, extraction of *CP* fractions from an angular analysis can also incorporate the modes $B^0 \to J/\psi K^{*0}(K^+\pi^-)$, $B^+ \to J/\psi K^{*+}(K^+\pi^0)$, $B^+ \to J/\psi K^{*+}(K^0\pi^+)$ and their charge conjugates.

5.4 Practical Requirements

The theory is sound. Now what do we actually need to do with the data in order to measure *CP* violation in this decay channel? The first step is selection of $B \to J/\psi K^*$ events from the e^+e^- data taken by the detector. This requires identification of $\Upsilon(4S) \to B\overline{B}$ events as well as reconstruction of the J/ψ, K_S, π^0 and K^* composite particles before forming the B meson from the J/ψ and K^*. The aim of the selection cuts is to provide a clean sample of such decays which implies rejection of collision events where $e^+e^- \to u\overline{u}, d\overline{d}, s\overline{s}, c\overline{c}, \tau^+\tau^-$ as well as $B\overline{B}$ events which do not produce the specified decay mode. Bhabha and μ-pair events will be automatically rejected since any exclusive reconstruction of $B \to J/\psi K^*$ requires at least three charged tracks to be present. This assumes that any K^0 in a decay mode in practice means $K^0 \to K_S \to \pi^+\pi^-$. The same modes with a $K_S \to \pi^0\pi^0$ or a K_L may well be added eventually but are not included in this analysis.

Once a reasonably clean and sufficiently large sample of $J/\psi K^*$ events is obtained, one can then proceed to fit the angular distributions in order to determine the dilution factor D. Of course, how clean 'reasonably clean' is depends on such factors as whether the various backgrounds distort the shape of the distributions significantly. So, D determines the *CP* mixture in $J/\psi K^*$ events but *CP* violation can only be seen in *tagged* $J/\psi K^{*0}(K_S\pi^0)$ decays. For this measurement, we essentially form the numerator of equation 1.45 where t, the difference in time between the two B decays

is calculated from measurements of the z positions of their decay points. For the *CP* mode B this comes from the J/ψ vertex. The z position for the tag B comes from the fitted common vertex of its tracks according to a specially developed vertexing algorithm. The result is a sine wave modulated by $e^{-\Gamma|t|}$ with an amplitude that can be directly related to $\sin 2\beta$.

5.5 The Creation of Data Skims

The events which are stored in the BABAR database by the OPR system as described in section 2.3.8 can be analyzed offline and samples made which satisfy certain criteria. The dataset used for this analysis comes from skims over all usable physics events up to run 9973 (24th October 1999), selecting only those with a candidate for $J/\psi \to l^+l^-$. Two skims are used in this analysis, one designed to select $J/\psi \to e^+e^-$ and the other to select $J/\psi \to \mu^+\mu^-$. A general selection was applied in both cases, aimed at choosing $B\overline{B}$ events that might contain $J/\psi \to l^+l^-$ by cutting on tag[1] variables. This is summarized in table 5.1.

A J/ψ candidate is defined as two oppositely charged tracks with an invariant mass between 2.5 GeVand 4.0 GeV. The GoodTracksTight list is comprised of all charged tracks satisfying the following criteria: $p_t > 100\,\mathrm{MeV/c}$; $p < 10\,\mathrm{GeV/c}$; # DCH hits ≥ 20; χ^2_{prob} of track fit > 0; DOCA in the xy plane $< 1\,\mathrm{cm}$; and abs(z-DOCA) $< 3\,\mathrm{cm}$. Here DOCA is just the distance of closest approach of the track to the primary vertex of the event. The GoodTracksLoose list is as the above but with xy-DOCA $< 1.5\,\mathrm{cm}$ and abs(z-DOCA) $< 10\,\mathrm{cm}$.

Additionally, each skim has its own set of cuts applied to the J/ψ daughters aimed

[1]The tag database contains event variables such as trigger flags, physics process flags and other global quantities like those in the table. The idea is to use the tag database to run quickly over a large dataset, cutting on a few of the quantities, to select a much smaller sample of events for full analysis.

Cut	Description of Variable
nTracks > 3	Number of charged tracks
nGoodTrackTight > 1	Number of GoodTracksTight
$0.4 <$ p1mag < 3.0 GeV	Momentum of highest momentum track
$0.3 <$ p2mag < 2.5 GeV	Momentum of second highest momentum track
abs(totalChargeLoose) < 6	Sum of charge in GoodTracksLoose
R2 < 0.7	Ratio of 2nd to 0th Fox-Wolfram moments
$N_{J/\psi} \geq 1$	Number of J/ψ candidates in the event

Table 5.1: *The cuts used for general selection of $B\overline{B}$ events containing a $J/\psi \to l^+l^-$ candidate from all physics events.*

at selecting either electrons or muons. The electron skim requires that at least one of the J/ψ candidates has both tracks identified as electrons. The muon skim requires that both of the tracks from at least one of J/ψ candidates have a MIP signature in the EMC. The IFR has not been used for muon identification in the analysis of this particular set of data since it was not in full working order at the time. These criteria are summarized below in table 5.2. The case $E = 0$ corresponds to a track having no associated EMC energy deposit.

5.6 J/ψ Reconstruction

The most prominent signature of this decay channel is the presence of a convincing candidate for $J/\psi \to e^+e^-$ or $J/\psi \to \mu^+\mu^-$. The J/ψ signal in the BABAR environment has low background compared to particles such as the K^0_S or π^0 and also helps in the rejection of light quark events. Part of the reconstruction of the J/ψ is common to both leptonic decay modes. All pairs of oppositely charged tracks found

Cut	# tracks	Description of Variable
Electron Skim		
$E/p > 0.6$ or $E = 0$	2	EMC energy, DCH momentum
Muon Skim		
50 MeV < E < 400 MeV or $E = 0$	2	EMC energy

Table 5.2: *The additional cuts used for making individual electron and muon skims from all physics events. The central column denotes whether one or both of the J/ψ daughters must satisfy the criteria.*

in the SVT and DCH are required to have an invariant mass between $2.5\,\mathrm{GeV/c^2}$ and $3.2\,\mathrm{GeV/c^2}$ after being fitted to a common vertex. The χ^2 probability of the fit is then required to be at least 1%. The kinematics of the process permit a cut on the measured momentum of the leptons as well as the J/ψ momentum in the CMS[2]. Both leptons must have a momentum greater than 700 MeV/c and one must be greater than 1.7 GeV/c. The J/ψ is restricted to $1.3\,\mathrm{GeV/c} < \mathrm{p}^*_{\mathrm{J}/\psi} < 1.9\,\mathrm{GeV/c}$. A comparison between data and MC for the χ^2 probability and CMS momentum is shown in the top two plots of figure 5.3. The mismatch between data and Monte Carlo for the J/ψ CMS momentum is due to the fact that the MC represents only signal events. The data sample has an accumulation of events around 1.6 GeV/c also, it is just overwhelmed by the amount of other events in the sample.

5.6.1 $J/\psi \to e^+e^-$

The J/ψ will decay to electrons 6% of the time. This signal can be detected with the help of the EMC for identifying the e^+ and e^-. The E/p ratios for each track are

[2]The center of mass system referred to throughout is that corresponding to the rest frame of the $\Upsilon(4S)$.

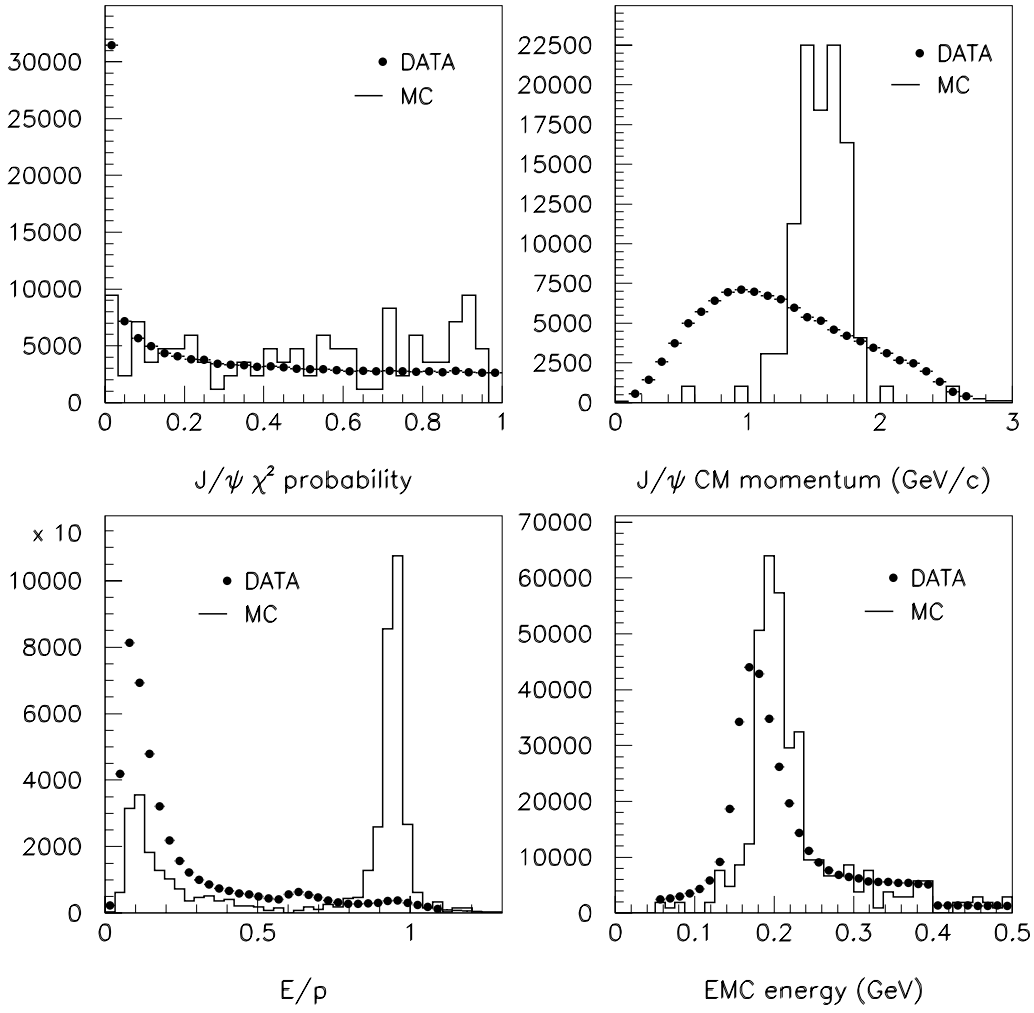

Figure 5.3: *Data versus signal Monte Carlo comparisons of the cut variables for* $J/\psi \to l^+l^-$ *selection.*

formed where $E = E_{EMC}$ and p is just the momentum as measured by the tracking system. The electron selection requires that for both tracks $0.8 < E/p < 1.4$[3]. Tracks are also accepted as electrons if $E = 0$, that is there was no associated EMC energy deposit. This reflects the optimistic view that it is worth keeping them in case they are electrons, rather than throw them away in ignorance. The distribution of E/p for both data and MC is shown in the lower left plot of figure 5.3. There is a significant peak near $E/p = 1$ for the MC sample since it contains many more electrons than the data sample.

5.6.2 $J/\psi \to \mu^+\mu^-$

The branching ratio for J/ψ to muons is 6%, the same as for the electron channel. The primary muon identification device in BABAR is the IFR but it was not fully operational when this data was collected and therefore no attempt has been made here to use information from that subdetector. However, as mentioned in previous chapters, E_{EMC} for muons comes almost exclusively from ionization and is largely independent of momentum. Thus it helps to require $50\,\mathrm{MeV} < \mathrm{E_{EMC}} < 400\,\mathrm{MeV}$. Since the muon channel is not as clean as the electron channel, mainly due to the absence of IFR information, extra cuts are required to get a clean selected sample. In this case, tracks with $E = 0$ are not accepted. The distribution of measured EMC energy for muon candidates is shown in the lower right plot of figure 5.3. The discontinuities at 50 MeV and 400 MeV are due to the preselection cuts described in table 5.2. The shift between the data and MC peaks shows that the EMC was not well calibrated at these energies for much of this data set. Additional cuts that are used for this channel only are described below in section 5.12.

[3]Values of E/p that are greater than one tend to correspond to high energy particles which bremsstrahlung early in the detector. The radiated photon is almost colinear and so contributes to the same EMC cluster as the charged particle itself.

5.7 K_S^0 Reconstruction

Once there is an identified J/ψ candidate in the event, the next step is to look for a possible $K_S \to \pi^+\pi^-$. The strategy here is to fit each oppositely charged pair of tracks to a common vertex using an algorithm that allows for detached vertices. The K_S has a $c\tau$ of 2.68 cm with an average boost of $\beta\gamma \sim 2.4$ and so has a decay distribution which extends away from the interaction point by a substantial amount. The vertex fit is required to have $\chi^2_{prob} > 0.01$ and the resultant invariant mass must be between 450 MeV/c^2 and 550 MeV/c^2. The decay point must then be at least 2 mm from the primary vertex in the xy plane and no more than 50 cm away in any direction. The latter cut ensures that there are enough hits in the tracking system to provide an accurate measurement of the K_S momentum. To ensure that the candidate really came from the primary vertex, a cut is made on the angle between the K_S momentum vector and a line pointing from the primary vertex to its decay point. This angle must be no more than 150 mrad in the xy plane. Finally, one can define the helicity angle as that angle between the momentum vector of one of the pions in the K_S rest frame and the K_S direction. The absolute value of the cosine of this angle is restricted to $|\cos\theta_H| < 0.95$. This is because one finds that the background in this decay peaks at $|\cos\theta_H| = 1$ due to combinations of one fast and one slow track adding to make the K_S mass. Distributions for the main cut variables are shown in figure 5.4 and the resultant K_S candidate mass spectrum is shown in figure 5.5. The overall asymmetry in the $\cos\theta_H$ distribution is due to the way charged tracks are ordered according to their momenta when they are reconstructed. This results in the first track in the list of K_S daughters to have on average a greater momentum than the second track. Since it is this first track that is used in the helicity angle calculation, the distribution is biased towards $\cos\theta_H = 1$.

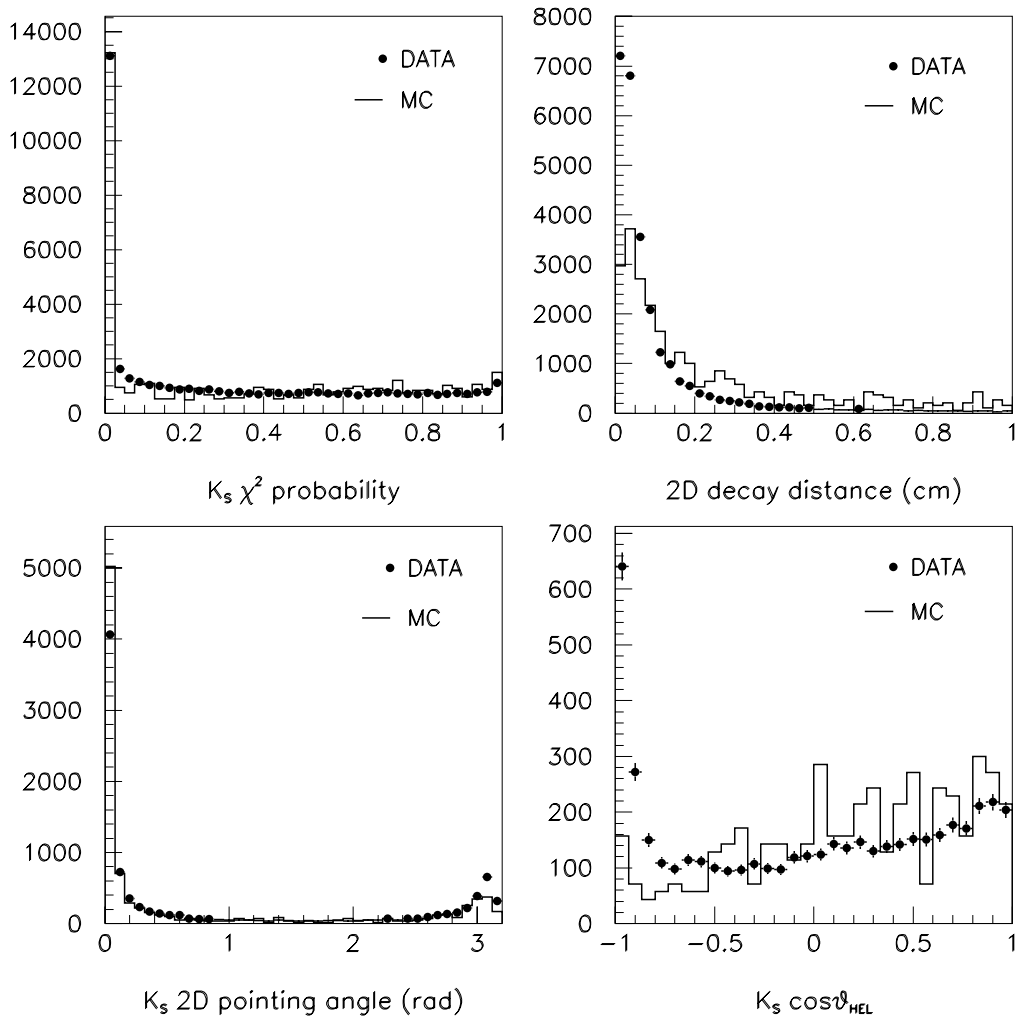

Figure 5.4: *Distributions showing data and signal MC distributions for the geometrical cuts used to select K_S candidates.*

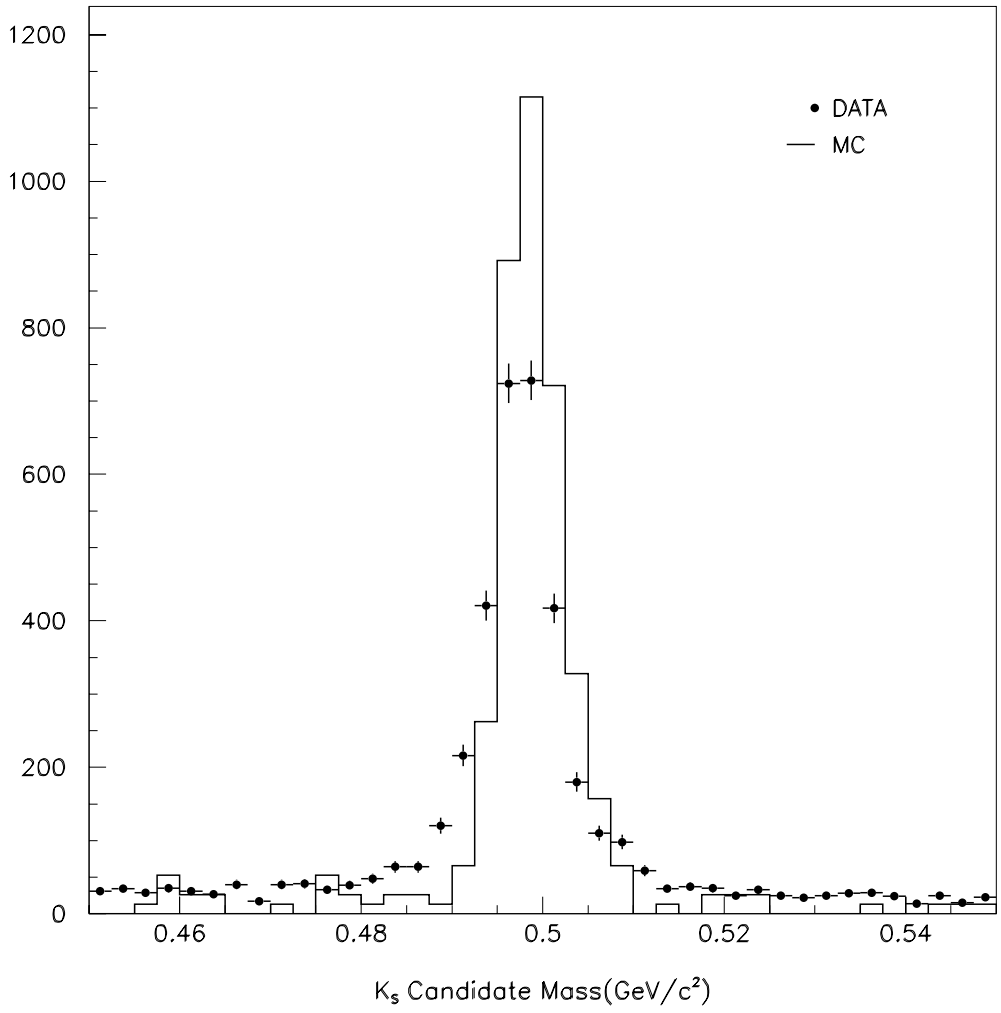

Figure 5.5: *The K_S candidate mass spectrum after all cuts have been applied.*

5.8 π^0 Reconstruction

Now that there are possible J/ψ and K_S candidates, we look for π^0s for combination with the K_S in constructing the K^{*0}. The starting point is the list of all EMC bumps with no associated charged track. All possible combinations of pairs of these photon candidates is made in an attempt to reconstruct $\pi^0 \to \gamma\gamma$. Combinations are kept if they have an invariant mass between 70 MeV/c^2 and 200 MeV/c^2. In an attempt to remove low energy calorimeter noise, then following energy cuts are applied: $E_\gamma > 100\,\text{MeV}$ and $E_{\pi^0} > 300\,\text{MeV}$. In addition, a lateral shower shape parameter can be defined

$$LAT = \frac{\sum_{i=3}^{N} E_i r_i^2}{\sum_{i=3}^{N} E_i r_i^2 + E_1 r_0^2 + E_2 r_0^2}, \tag{5.17}$$

where the cluster is composed of N crystals with energies E_i ordered so that $E_1 > E_2 > ... > E_N$ and r_0 is the average distance between two crystals (about 5 cm in the BABAR EMC). The polar coordinates r_i, ϕ_i are in the plane perpendicular to the line joining the interaction point and the cluster center and are shown in figure 5.6. This variable provides discrimination between electromagnetic and hadronic showers on the basis of their average properties. In the case of electromagnetic showers, most of the energy is deposited in two or three crystals giving a small value of LAT. For hadronic showers, the variable should be closer to one due to the squared distances enhancing the effect from widely spread hadronic interactions. The photons are required to have LAT < 0.8. The distributions of LAT, E_γ and E_{π^0} are shown in figure 5.7.

No attempt is made here to identify merged π^0s, that is decays in which the two photon showers overlap in the EMC to such a degree that they cannot be resolved individually. The effect becomes increasingly important at high π^0 energies. At 1 GeV for instance, nearly 20% of π^0s are merged. This number increases to 70% at 2 GeV [58].

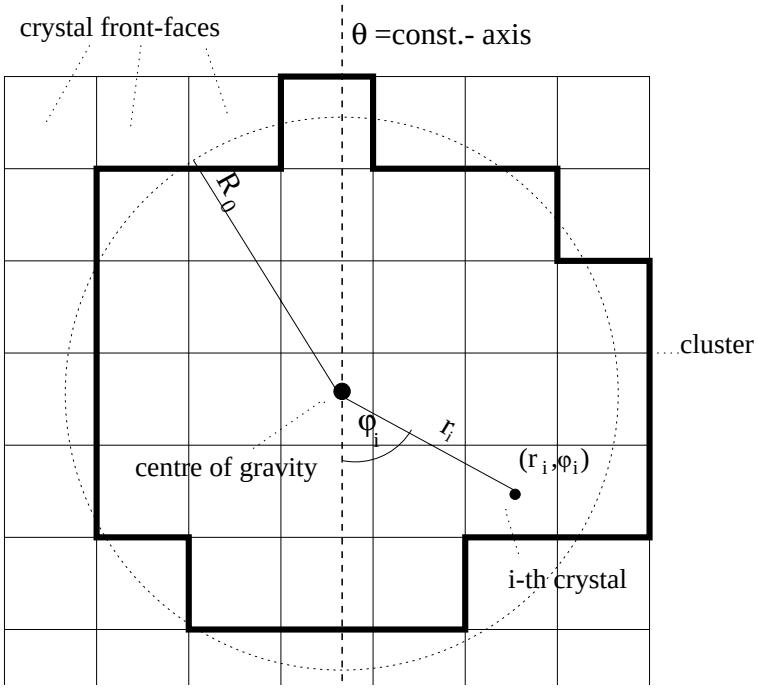

Figure 5.6: *The plane of polar coordinates for defining the LAT variable.*

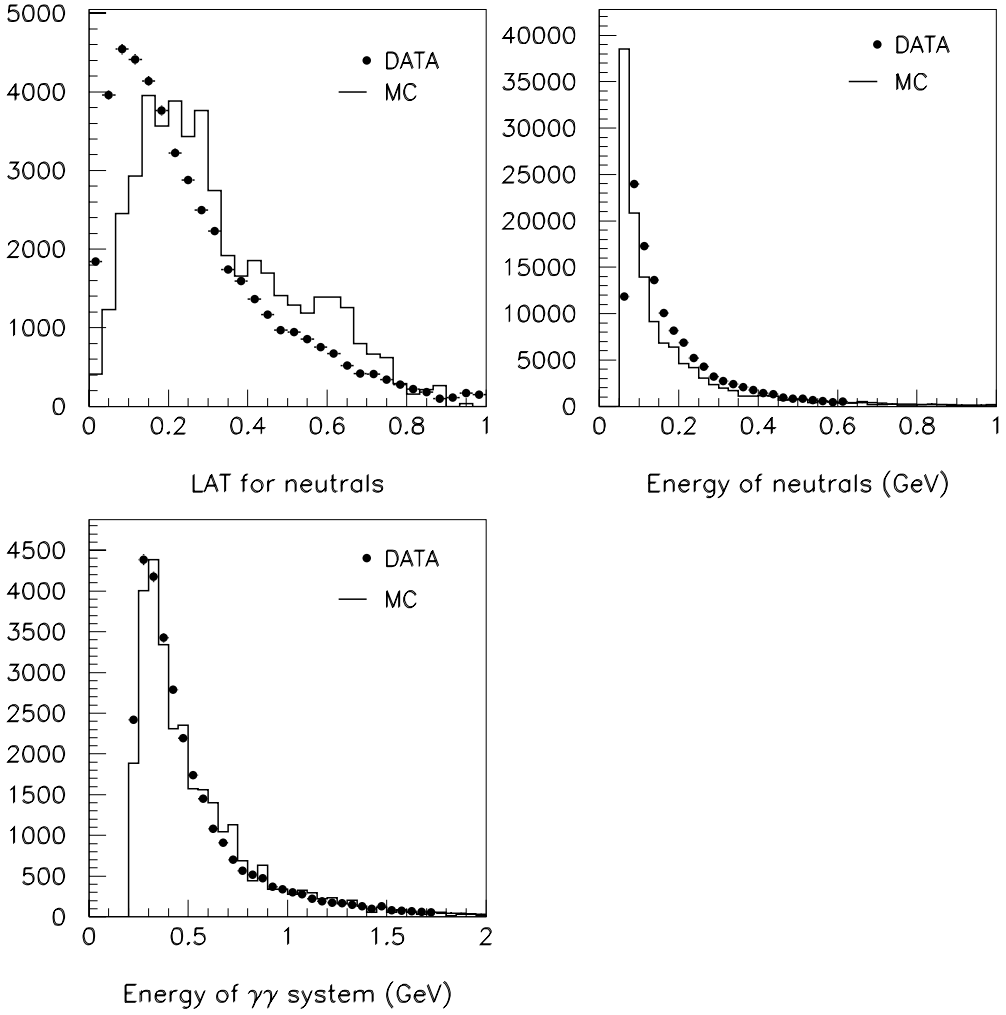

Figure 5.7: *Data-MC distributions for the LAT, E_γ and E_{π^0} variables used in π^0 selection.*

5.9 Building the $K^{*0}(K_S\pi^0)$

Once there are a set of K_S and π^0 candidates for a given event, all possible combinations of them are made to form K^{*0} candidates. Cuts are placed on the masses of the K_S and π^0 at $467.5\,\mathrm{MeV/c^2} < \mathrm{M_{K_S}} < 527.5\,\mathrm{MeV/c^2}$ and $115\,\mathrm{MeV/c^2} < \mathrm{M_{\pi^0}} < 145\,\mathrm{MeV/c^2}$ as well as an adjusted π^0 energy cut determined from Monte Carlo of $0.3\,\mathrm{GeV} < \mathrm{E_{\pi^0}} < 1.6\,\mathrm{GeV}$. It turns out that this combination of cuts alone does not give a particularly convincing $K^{*0} \to K_S\pi^0$ signal. The main culprit is the π^0. For this data set, the detector is essentially still in a tuning phase where individual subdetectors are in an iterative cycle of calibration. Of course, this will always be the case but the hope is that eventually the calibrations become stable. This was not the case for the EMC while this data was being collected. Thus, the π^0 mass peak appears shifted from the true mass as well as being broader than expected. To help correct for a poorly calibrated EMC in this data, the π^0 calibration as mentioned in section 4.2.4 was applied. The aim is to shift the π^0 and K^{*0} mass peaks closer to their expected values and possibly also reduce their widths.

5.9.1 'Re-calibrating' the π^0

The method [59] applies corrections to the photon energies with the aim of improving the position of the mass peak. This is done using the constraint

$$M_\pi^2 = 2E_1E_2(1 - \cos\alpha) \tag{5.18}$$

where M_π is the true π^0 mass, E_i are the corrected photon energies and α is the angle between the two photons as seen from the origin of the BABAR coordinate system. Equation 4.2 is used to express the above constraint in terms of the correction coefficients C_i allowing them to be extracted from fits to a π^0 sample from real data. The sample was taken from the same data set which is used throughout this analysis using the same cuts as in section 5.8. Feeding this data into the offline calibration

program yielded stable, non-zero coefficients for the constant, $\ln E$, $(\ln E)^2$ and $(\cos\theta)^2$ terms of the correction function after a few iterations. These constants were then used to adjust the photon energies at the PAW analysis stage which in turn necessitated recalculation of the kinematic parameters for the π^0, K^{*0} and B^0. When recalculating the K^{*0} parameters, the K_S mass was fixed at its PDG value. The π^0 and K^{*0} mass spectra before and after recalibration are shown in figures 5.8 and 5.9 respectively for a subset of the main data sample. The original π^0 cuts were not retuned once the this stand-alone calibration was applied. The size of the data set under consideration meant that it was only practical to derive a calibration based on some small subset of the data. Once this correction is applied to the entire data set, the effect is a rather broad peak albeit shifted close to the correct π^0 mass. The original mass cut, for instance, now appears to be rather too tight and some signal is lost. In the future a full treatment would involve deriving calibrations for each small data subset individually and tuning the cuts accordingly. However, what is really worth waiting for is when the π^0 calibration is run over each batch of data immediately after it has been reconstructed and then the necessary constants are available to all physics users automatically.

5.10 Reconstruction of $K^{*0} \to K^+\pi^-$, $\overline{K}^{*0} \to K^-\pi^+$

Looking for the K^{*0} in its partner mode to two charged tracks is an entirely different proposition. On the one hand there is no π^0 to worry about and on the other there is now a charged kaon in the decay, which would benefit from some form of particle identification. The fundamental problem with this data set is that BABAR's primary kaon identification device, the DIRC, was not fully installed when the data was taken. Thus no attempt has been made here to use this device.

When forming the K^{*0} candidates, all oppositely charged combinations of pion and kaon candidates are used where the list of kaons is just a copy of the list of all charged

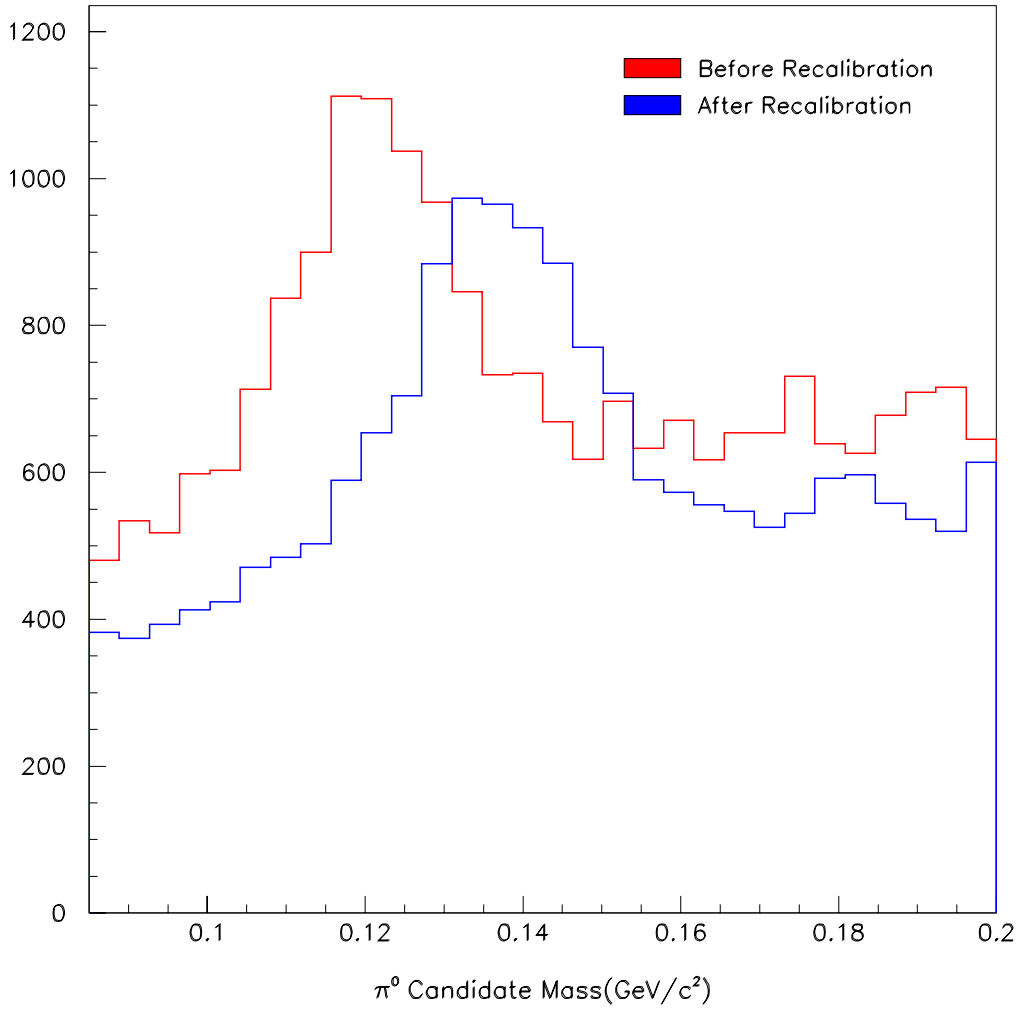

Figure 5.8: *The $\gamma\gamma$ mass spectrum before and after recalibration. The peak has clearly been shifted to the vicinity of the expected π^0 mass (135 $\mathrm{MeV/c^2}$).*

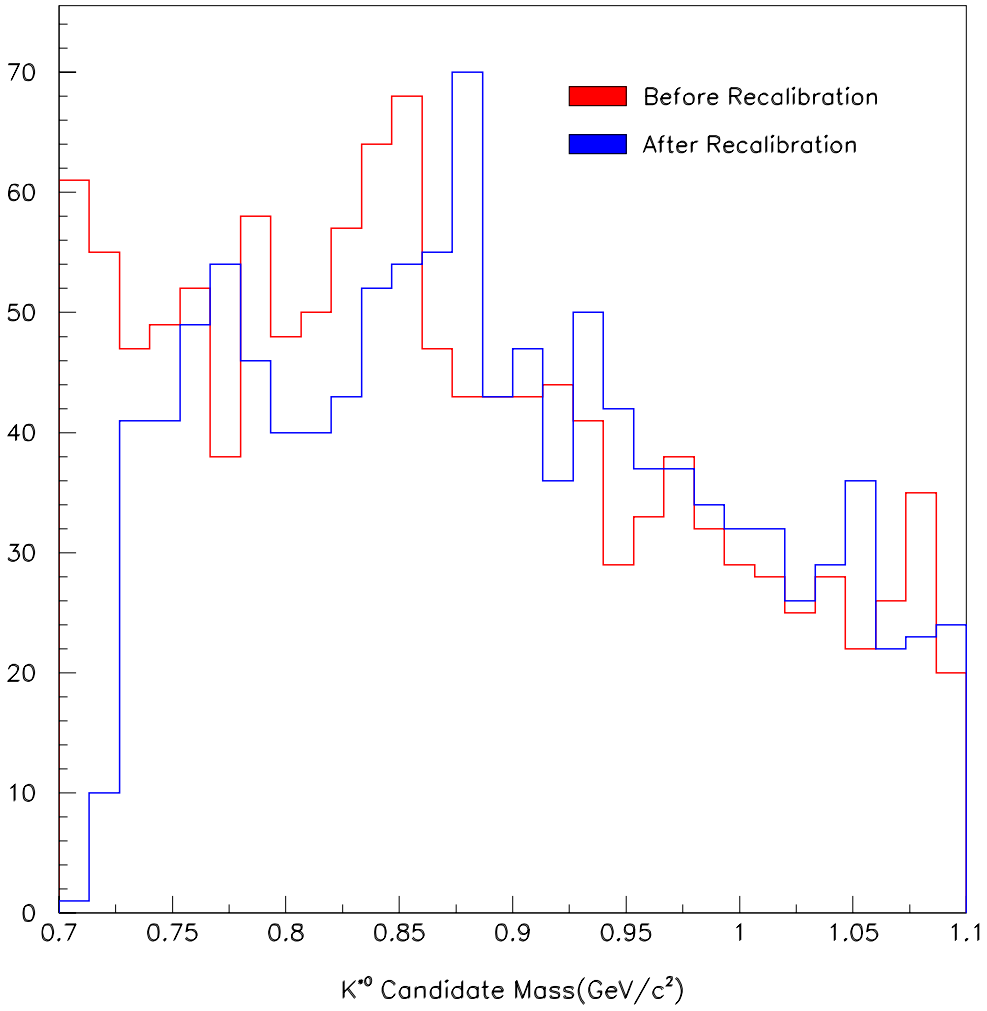

Figure 5.9: *The $K^{*0} \to K_S\pi^0$ candidate mass spectrum before and after recalibration. The expected K^{*0} mass is 896* $\mathrm{MeV/c^2}$.

tracks with their masses set accordingly. The vertexing routine used to fit the tracks to a common vertex is the same as that used for the $J/\psi \to l^+l^-$ decay. The $K\pi$ system is then subject to a loose mass cut of $0.7\,\mathrm{GeV/c^2} < \mathrm{M_{K^*}} < 1.1\,\mathrm{GeV/c^2}$ to cut down the amount of data that is stored in the ntuple. At the PAW analysis level, only combinations with a χ^2 probability for the vertex of greater than 1% are accepted. The momentum of the K^{*0} in the CMS is restricted to $1.45\,\mathrm{GeV/c} < \mathrm{p^*_{K^*}} < 1.7\,\mathrm{GeV/c}$ and the invariant mass is required to be within $75\,\mathrm{MeV/c^2}$ of the PDG value. The distributions of χ^2 probability and CMS momentum for the K^{*0} candidates is shown for data and MC in figure 5.10. In the case of the CMS momentum, the two distributions do not compare exactly since the MC sample consists of signal events whereas the data sample contains a much greater proportion of background.

5.11 Building the B^0 from $J/\psi K^{*0}(K_S\pi^0)$

The B^0 is initially formed from all combinations of J/ψ and K^{*0} candidates while requiring that the K_S points back to the J/ψ vertex within 200 mrad and subject to the mass cut $5\,\mathrm{GeV/c^2} < \mathrm{M_B} < 5.5\,\mathrm{GeV/c^2}$. The K^{*0} mass must be between $0.7\,\mathrm{GeV/c^2}$and $1.1\,\mathrm{GeV/c^2}$. When the kinematic quantities of the B^0 candidate are recalculated following the π^0 recalibration, the J/ψ mass is fixed at its PDG value.

5.12 Building the B^0 from $J/\psi K^{*0}(K^\pm\pi^\mp)$

One more readily expects to see evidence of a signal in this channel than the previous mode since it has a higher reconstruction efficiency as well as a branching ratio that is roughly four times larger than the $K^{*0} \to K_S\pi^0$ channel. The reconstruction of B candidates proceeds largely as described above with a mass cuts of $5\,\mathrm{GeV/c^2} < \mathrm{M_B} < 5.5\,\mathrm{GeV/c^2}$ and $0.7\,\mathrm{GeV/c^2} < \mathrm{M_{K^*}} < 1.1\,\mathrm{GeV/c^2}$. A full fit is now performed

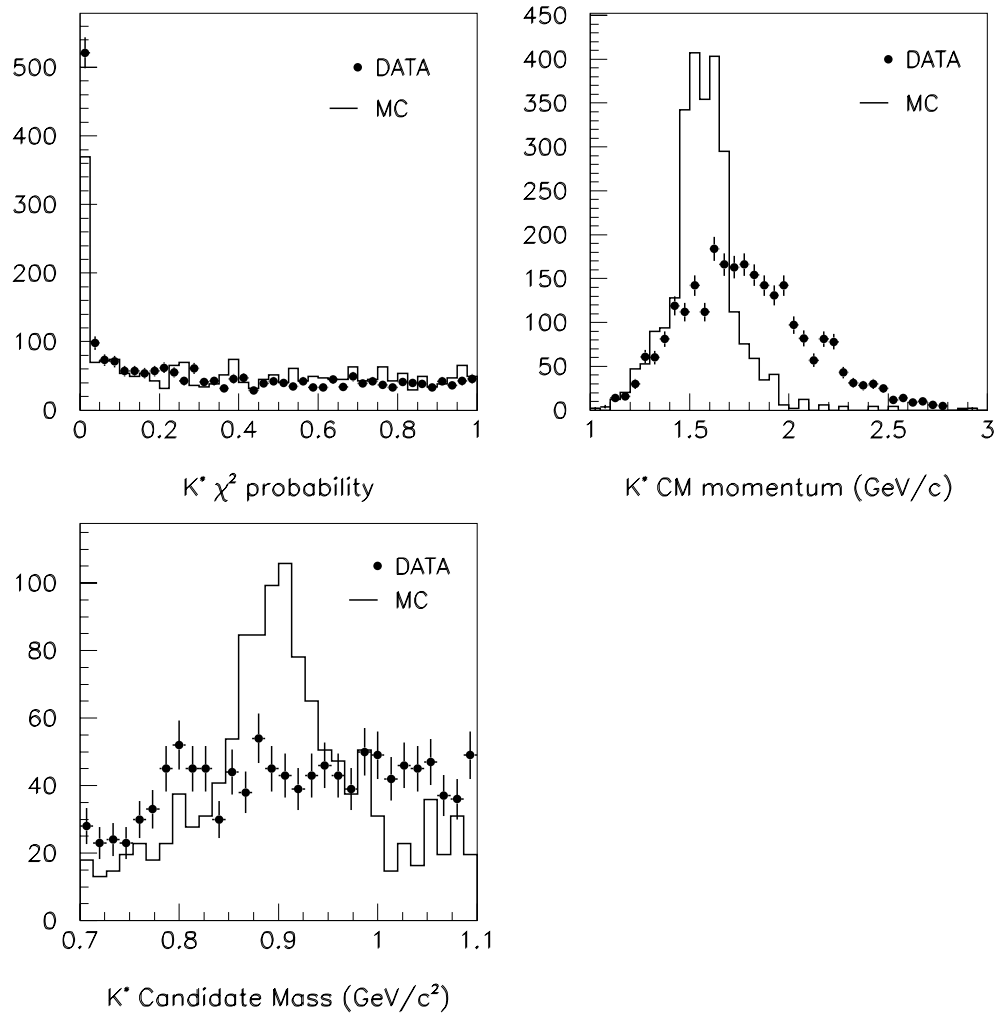

Figure 5.10: *The χ^2 probability distribution, CMS momentum spectrum and mass spectrum for $K^{*0} \to K^+\pi^-$ candidates. The MC sample is for signal events.*

on the four tracks that compose the B^0 candidate. Constraints are imposed such that the J/ψ daughters come from a common vertex and yield the correct J/ψ mass. The K^{*0} daughters are also constrained to come from a common vertex and the two vector mesons must point back to the same point, representing the decay of the B^0. It is then the fitted parameters which are used to calculate the kinematic parameters ΔE and M_b as described in the next section. Also, the R2 parameter described above was required to be less than 0.4, to further aid continuum background rejection.

As mentioned above, further cuts are applied to the $J/\psi \to \mu^+\mu^-$ mode when reconstructing the B in this channel. Firstly, it is required that the fits of the J/ψ and K^{*0} to their respective vertices must have converged. A kind of pseudo-χ^2 is then formed to provide some measure of the separation of the two vertices. It is written as

$$\chi^2_{\psi K^*} = \sqrt{\frac{(v_x^{\psi} - v_x^{K^*})^2}{\sigma^2_{\psi x} + \sigma^2_{K^* x}} + \frac{(v_y^{\psi} - v_y^{K^*})^2}{\sigma^2_{\psi y} + \sigma^2_{K^* y}} + \frac{(v_z^{\psi} - v_z^{K^*})^2}{\sigma^2_{\psi z} + \sigma^2_{K^* z}}} \tag{5.19}$$

where the v_i and σ_i are the coordinates and errors respectively of the J/ψ and K^{*0} vertices. Since the two vertices should be at the same point, a cut is placed such that the χ^2 must be less than 20. The pull distributions for the separation of the two vertices in x, y and z are shown in figure 5.11.

A cut is also placed on the angle between the K^{*0} and one of the leptons from the J/ψ in the rest frame of the J/ψ. The absolute value of the cosine of this angle is required to be less than 0.7. The motivation for this requirement comes from knowledge of the angular distributions of the vector meson decay products in $B \to J/\psi K^*$. A comparison of this 'helicity angle' for data and MC is shown in figure 5.12. After all these cuts it is useful to look at the composition of the final sample to check that the right kind of events are being selected. For instance, the mass distributions for the J/ψ in both the electron and muon channel after all cuts are shown in figure 5.13.

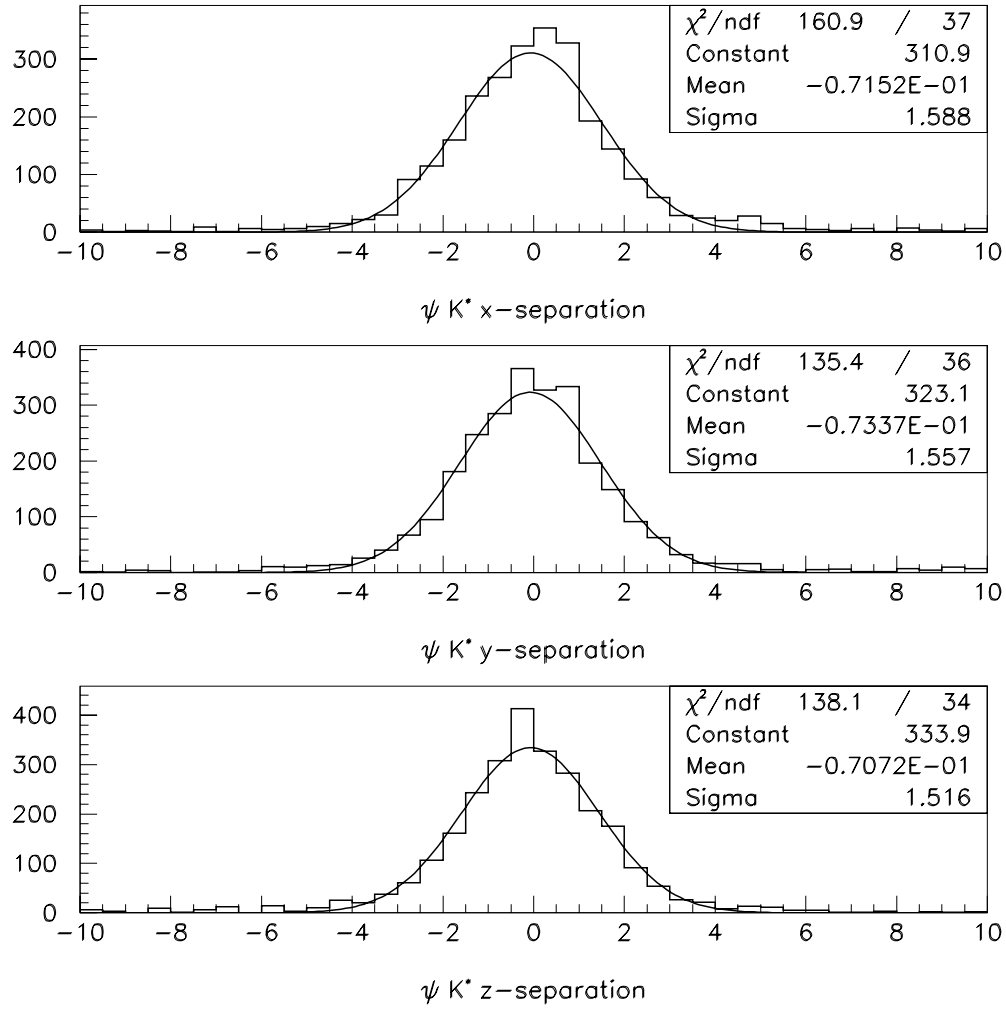

Figure 5.11: *Pull distributions for the separation of the J/ψ and K^{*0} vertices.*

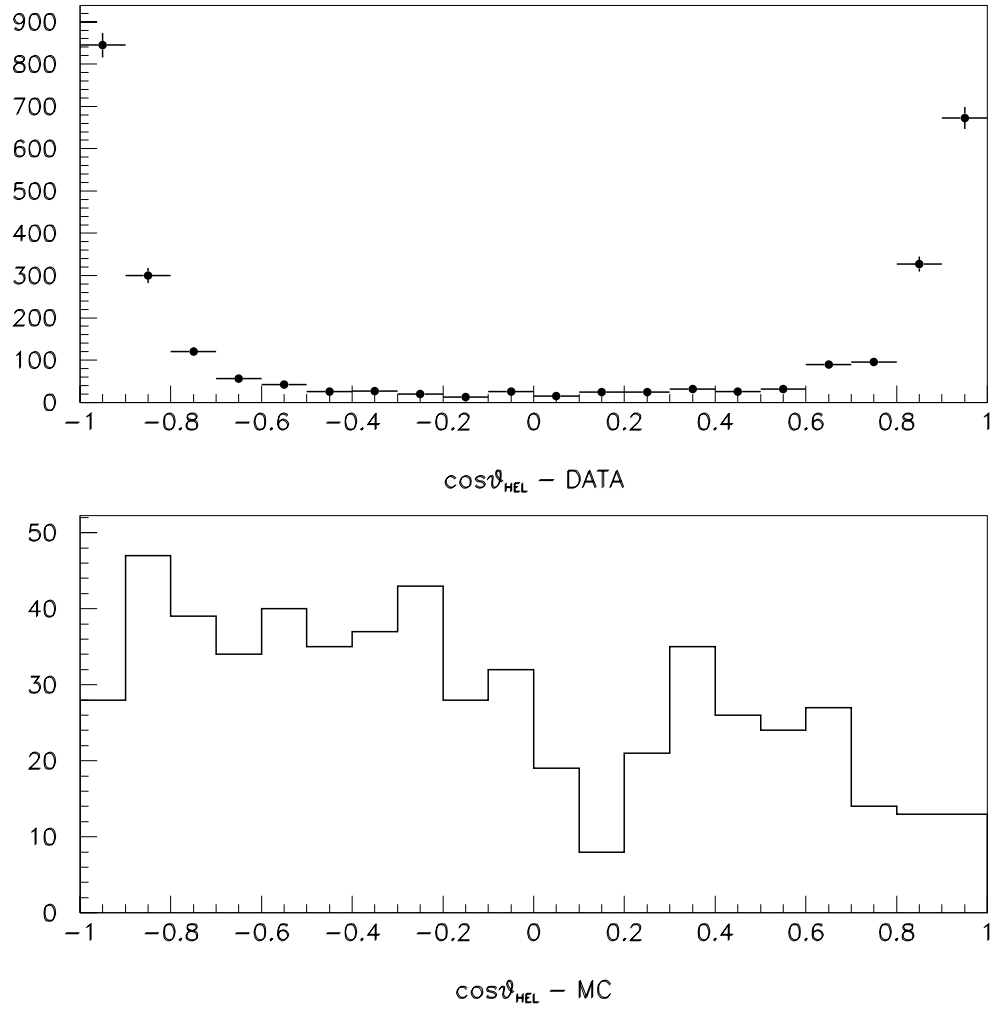

Figure 5.12: *A comparison between data and MC for the 'helicity angle' in* $J/\psi K^{*0}$.

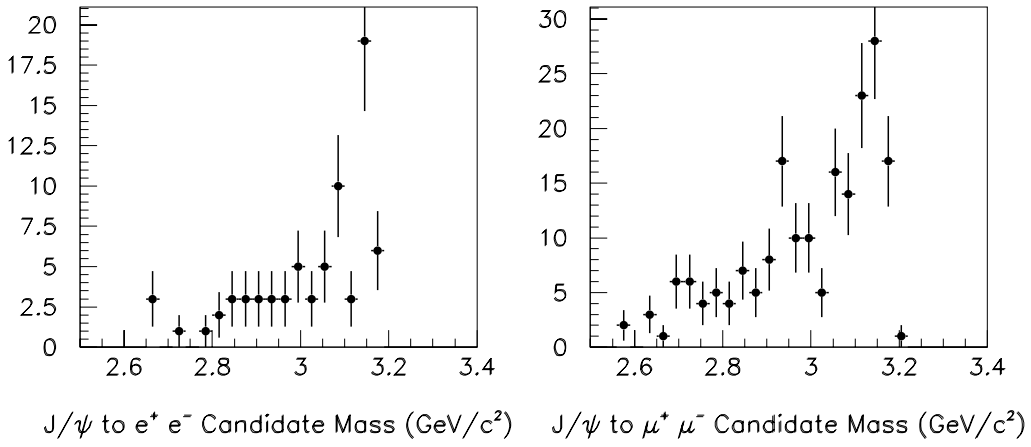

Figure 5.13: *The mass peaks for $J/\psi \to e^+e^-$ and $J/\psi \to mu^+mu^-$ after all cuts in the analysis.*

5.12.1 The Search for a Signal

Once all the cuts have been applied, the resultant sample of putative $B^0/\overline{B}^0$ candidates is examined for any evidence of a signal above the background expectations. The currently accepted method employed in BABAR physics analyses for doing this in exclusive B decays involves plotting ΔE against M_b. The ΔE variable is the measured energy of the B candidate minus $\sqrt{s}/2$. Thus it is expected to peak around zero for signal and is a check that one B candidate really does correspond to one half of the event. The other thing to check is that this combination really is a B meson and one way of doing this is to form the beam-constrained mass M_b from $\sqrt{s/4 - p_B^2}$ where p_B is the measured three-momentum of the B candidate. Thus any signal will show up as an excess of events around (5.279 GeV/c^2, 0.0 GeV) in the $M_b, \Delta E$ plane This excess is quantified by drawing a 'signal box' on the plot. One finds the resolution on ΔE and M_b from the data (or Monte Carlo if sufficient statistics are not available) and defines a three standard deviation signal region.

Events outside this region are assumed to be background dominated. Taking the ratio of the area of the signal box to the area of the plot minus the signal box allows one to make a rough estimate of the expected number of background events inside the signal box. One then decides whether there is good evidence for a signal on the basis of how many events are remaining after the background has been subtracted from the signal region.

5.13 Monte Carlo Analysis

Practically the same analysis was performed on a sample of 1000 Monte Carlo events as was used on the data itself. The events are all 'signal', where $e^+e^- \to B^0\overline{B}^0$ and one of the B's subsequently decays to $J/\psi K^{*0}$ where $J/\psi \to l^+l^-$ and $K^{*0} \to K^\pm\pi^\mp$. The full selection chain was carried out and the individual efficiencies were found to be as shown in table 5.3.

Selection	MC Efficiency
B-like event	(97 ± 3) %
At least one J/ψ candidate	(82 ± 3) %
$J/\psi \to e^+e^-$	(86 ± 5) %
$J/\psi \to \mu^+\mu^-$	(94 ± 5) %
$B^0 \to J/\psi K^{*0}$ analysis	(29 ± 2) %
All cuts (# in final sample/initial # of events)	(21 ± 1) %

Table 5.3: *Efficiencies from Monte Carlo of the different stages of selection for the* $B^0 \to J/\psi K^{*0}(K^\pm\pi^\mp)$ *analysis.*

5.14 Calculation of the $B^0 \to J/\psi K^{*0}$ Branching Ratio

In order to make a measurement of the branching ratio, one first carries out the background subtraction in the $\Delta E, M_b$ plot as described above. The events remaining form the final signal sample, but it is necessary to know the original number of $B^0 \to J/\psi K^{*0}$ events before any selection and so the signal efficiencies of these selections must be known. In particular, efficiencies must be known for the general J/ψ selection, the electron and muon skims and the cuts of the $J/\psi K^{*0}$ analysis. The final result is then simply the number of signal events in the original (pre-selection) sample divided by the number of B^0s present in the original sample. The latter is determined from the luminosity of the original data set, suitably corrected by taking the $\Upsilon(4S)$ resonance lineshape into account. The BaBar charmonium group has quoted the corrected luminosity for the first set of skims as $602\,\mathrm{pb}^{-1}$. Taking the $B\overline{B}$ cross-section from table 2.2.2, this yields $602\mathrm{pb}^{-1} \times (1.05 \times 10^3)\mathrm{nb} = 6.32 \times 10^5$ neutral B mesons. There is an implicit division and multiplication by two in the above, since half the events produce charged B mesons but for each event with neutrals, there are two mesons. Figure 5.14 shows the raw B^0 mass, the $\Delta E, M_b$ plane, and ΔE and M_b separately for the $K^{*0} \to K^{\pm}\pi^{\mp}$ channel. For comparison, the same plots for signal MC are shown in figure 5.15. In the case when there is more than one set of quantities for a given event, the set which has ΔE closest to zero is chosen. Subtracting background from the signal region of the $\Delta E, M_b$ plot as described above yields 12.6 events. The total efficiency for signal events in Monte Carlo is 21.4%. The branching ratio is then

$$BR\left[B^0 \to J/\psi(l^+l^-)K^{*0}(K^{\pm}\pi^{\mp})\right] = \frac{12.6}{0.214 \times (6.32 \times 10^5)} = 9.3 \times 10^{-5}.$$

Only the data sample representing the charged decay of the K^{*0} has been used here. For completeness, the kinematic variables for the $B^0 \to J/\psi K^{*0}(K_S\pi^0)$ channel are shown in figure 5.16 for data and in figure 5.17 for signal Monte Carlo.

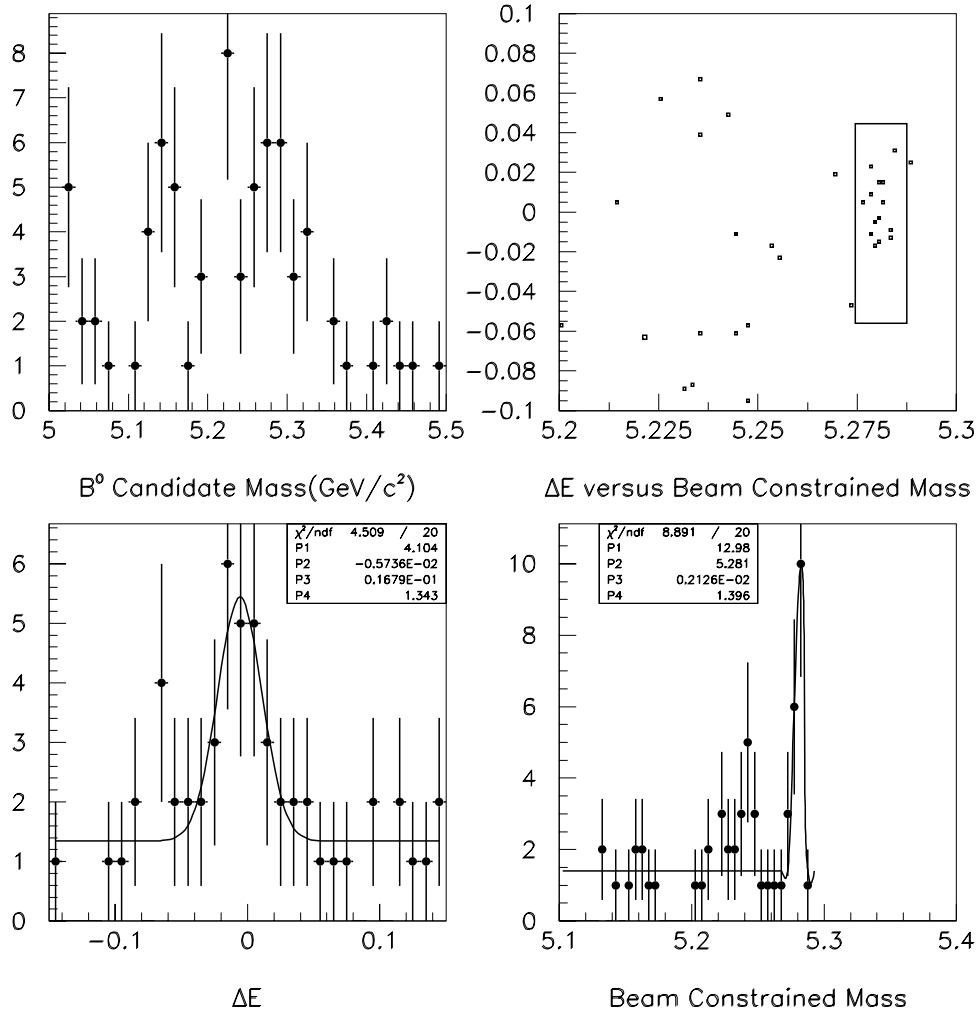

Figure 5.14: *The relevant kinematic quantities for the final* $B^0 \to J/\psi K^{*0}(K^{\pm}\pi^{\mp})$ *sample.* ΔE *and* M_b *have been fitted with lineshapes composed of a Gaussian peak and a flat background. The signal box in the 2d plane represents* 3σ *either side of the peaks.*

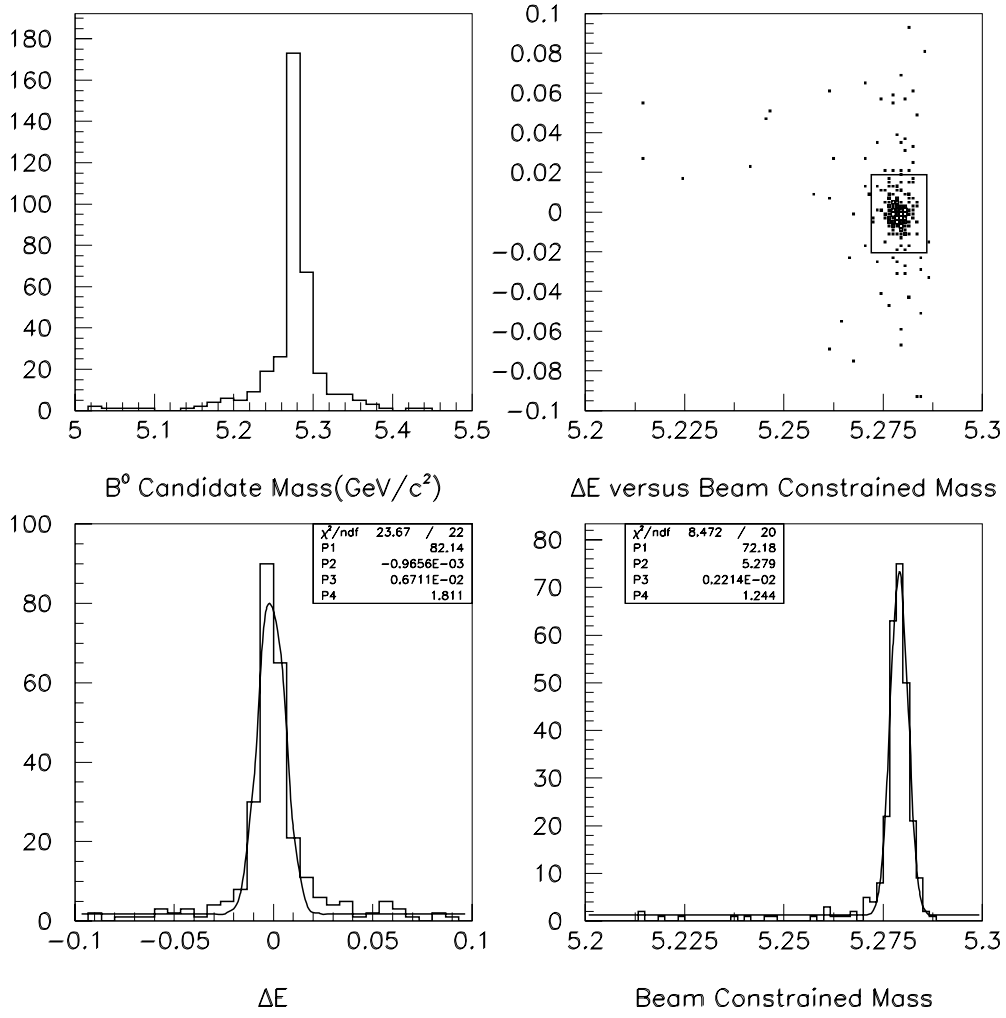

Figure 5.15: *MC - The relevant kinematic quantities for the final* $B^0 \to J/\psi K^{*0}(K^{\pm}\pi^{\mp})$ *sample.* ΔE *and* M_b *have been fitted with lineshapes composed of a Gaussian peak and a flat background. The signal box in the 2d plane represents* 3σ *either side of the peaks.*

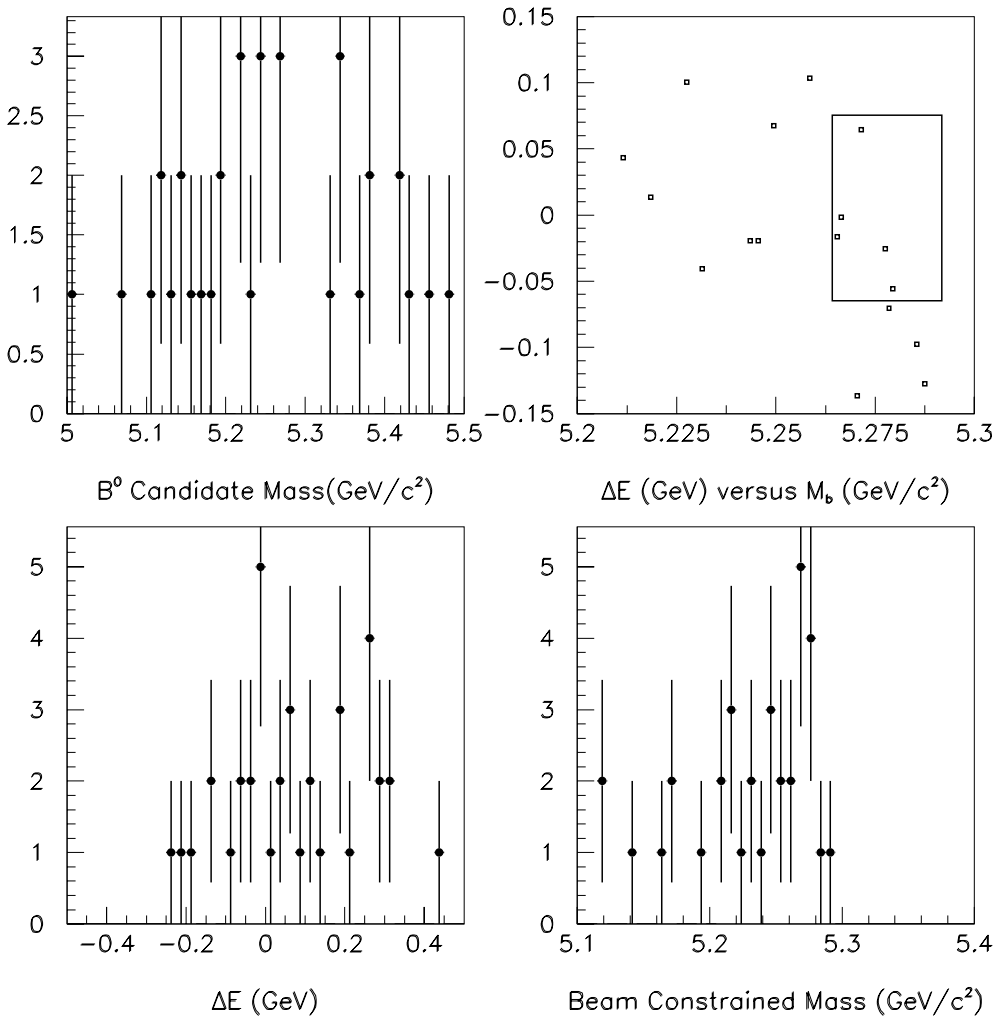

Figure 5.16: *The relevant kinematic quantities for the final* $B^0 \to J/\psi K^{*0}(K_S\pi^0)$ *sample.* ΔE *and* M_b *have been fitted with lineshapes composed of a Gaussian peak and a flat background. The signal box in the 2d plane represents* 3σ *either side of the peaks.*

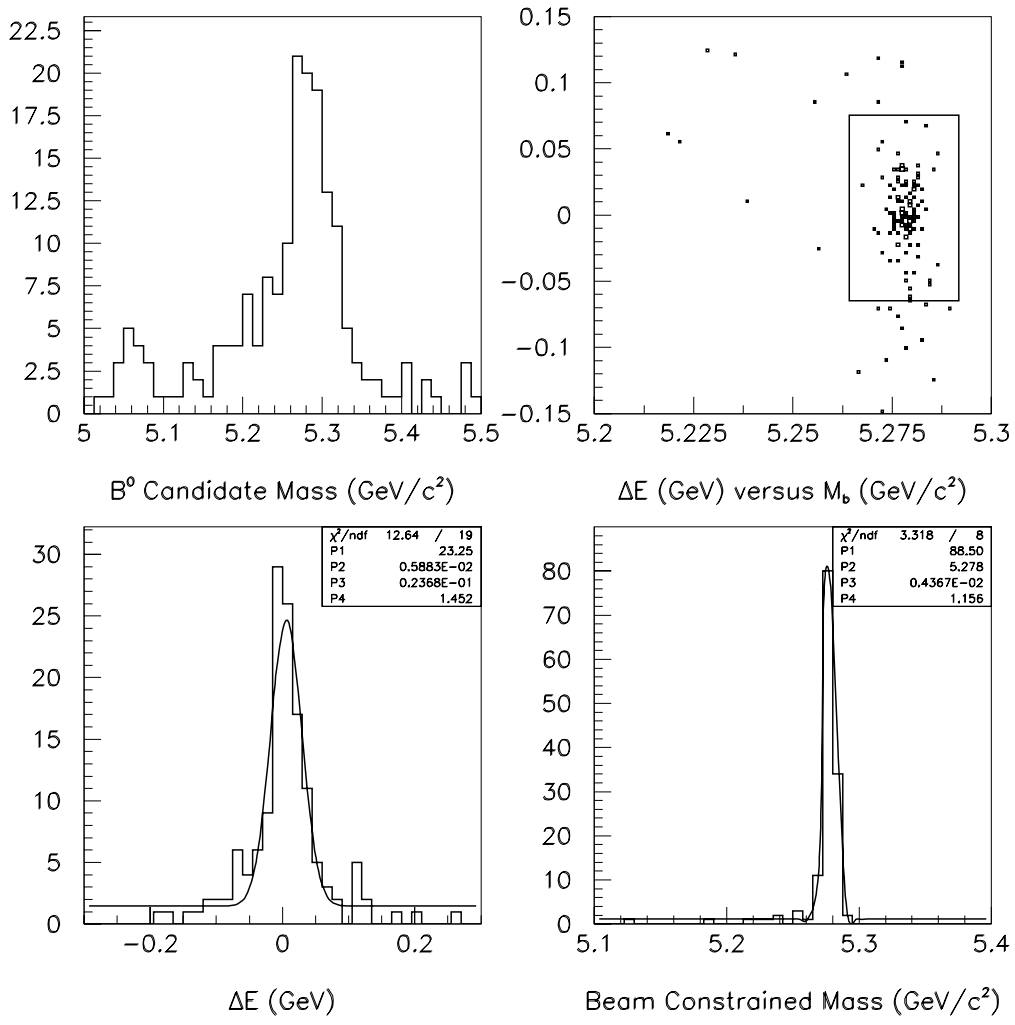

Figure 5.17: *MC - The relevant kinematic quantities for the final* $B^0 \to J/\psi K^{*0}(K_S\pi^0)$ *sample.* ΔE *and* M_b *have been fitted with lineshapes composed of a Gaussian peak and a flat background. The signal box in the 2d plane represents* 3σ *either side of the peaks.*

5.15 Error Analysis

There are errors on the three quantities in the branching ratio equation. The uncertainty on the total neutral B meson yield comes from the estimate of the $e^+e^- \to b\overline{b}$ cross-section as quoted in the BaBar physics book [60], (1.05 ± 0.1) nb. The statistical errors on the Monte Carlo efficiency and the background subtracted signal yield were taken as $\sqrt{N}$. In addition there are systematic uncertainties due to how much faith can be put in both the MC efficiency and the background estimate from which the final signal yield is derived. It has been estimated that the size of the uncertainty on both the final number of signal events and the MC efficiency is 10%.

Adding these contributions in quadrature gives a final result of

$$BR\left[B^0 \to J/\psi(l^+l^-)K^{*0}(K^\pm\pi^\mp)\right] = (9.3 \pm 2.7 \pm 1.6) \times 10^{-5}$$

where the first error is statistical and the second systematic. This is to be compared with the currently accepted value of

$$(1.35 \pm 0.18) \times 10^{-3} \times (0.1203 \pm 0.0027) \times 0.67 = (1.09 \pm 0.15) \times 10^{-4}.$$

The three terms in the above product are the branching fractions for $B^0 \to J/\psi K^{*0}$, $J/\psi \to l^+l^-$ and $K^{*0} \to K^\pm\pi^\mp$ respectively.

5.16 Chapter Summary

An analysis has been developed to select $B^0 \to J/\psi K^{*0}$ events using the BaBar detector. It has been shown how the EMC can be used for electron and muon identification as well as providing useful discriminating variables for γ selection. A clean K_S sample can be achieved by using a variety of geometrical cuts using information from the tracking system. The technique of using the so-called π^0 calibration to improve the π^0 and $K^{*0} \to K_S\pi^0$ signals has been demonstrated to

be beneficial, especially given the relatively uncalibrated energies in this data set. Furthermore, this selection has been used as part of a full analysis chain, going right through to the measurement of the $B^0 \to J/\psi K^{*0}$ branching ratio using the charged decay mode of the K^{*0}.

Prospects for the analysis of this B meson decay mode look good. With a well calibrated, fully working detector running in b-factory mode the quantity and quality of data produced should allow not only a considerable refinement of this measurement, but also determinations of the dilution factor and $\sin 2\beta$ as described at the start of the chapter.

Chapter 6

Conclusions

The BaBar experiment has been running since May 1999 with the main aim of measuring CP asymmetries in the B meson system. A comprehensive description of the phenomenon of CP violation within the standard model has been given along with its relevance for this experiment. The measurements from BaBar can be used to over constrain the unitarity triangle through the analysis of many different B decay modes. One of the decay modes which can be used to measure $\sin 2\beta$ is $B^0 \to J/\psi K^{*0}(K_S\pi^0)$. The analysis in this case is complicated by the need for study of the vector meson decay angles, which is facilitated by the addition of non CP-eigenstate modes: $B^0 \to J/\psi K^{*0}(K^{\pm}\pi^{\mp})$, $B^{\pm} \to J/\psi K^{*\pm}(K^{\pm}\pi^0)$ and $B^{\pm} \to J/\psi K^{*\pm}(K_S\pi^{\pm})$.

One of the principal components of the detector is a CsI crystal electromagnetic calorimeter (EMC). The importance of calibrating this device accurately and through several independent methods has been stressed. A description of the work done to date on the minimum ionizing particle calibration for correction of single crystal energies has shown that this method will work well in conjunction with other calibrations to provide a well calibrated EMC at all energies of interest. It has already been demonstrated with some success using cosmic ray muons.

A well calibrated EMC will come into its own as a particle identification device, particularly for electrons and photons. However there is also evidence that this device can be used to provide some level of muon discrimination by virtue of the minimum ionizing nature of these particles. The distributions of deposited energy of the various particle species have been studied, and the software developed to provide particle identification statistics for the muon hypothesis based on certain characteristics of particles in the detector.

An analysis of the two main $B^0 \to J/\psi K^{*0}$ decay channels was performed with the first 6 months worth of data from the experiment, some of which uses the cosmics-derived EMC calibration. Selection of the electrons and muons for J/ψ reconstruction uses information from the EMC, and a first test of the π^0 calibration machinery has been shown to improve the $K^{*0} \to K_S\pi^0$ signal. The branching ratio for $B^0 \to J/\psi(l^+l^-)K^{*0}(K^\pm\pi^\mp)$ has been measured as $(9.3 \pm 2.7 \pm 1.6) \times 10^{-5}$ which is in agreement with the expected value. The prospects for this decay channel given greater statistics from the experiment look very good and over time it will provide an invaluable contribution to the constraints on the unitarity triangle.

Appendix A

The Bethe-Bloch Formula

The Bethe-Bloch formula describes the mean rate of energy loss (or stopping power) by ionization of a charged particle [5] :

$$-\frac{dE}{dx} = Kz^2 \frac{Z}{A} \frac{1}{\beta^2} \left[\frac{1}{2} \ln \frac{2m_e c^2 \beta^2 \gamma^2 T_{max}}{I^2} - \beta^2 - \frac{\delta}{2} \right]. \tag{A.1}$$

Here T_{max} is the maximum kinetic energy which can be imparted to a free electron in a single collision, the kinematic variables β and γ have their usual meanings and the other variables are defined in table A.1. In this case the units are chosen so that dx is measured in mass per unit area (g cm^{-2}).

It is helpful to now point out the main features of this formula (see figure 3.2 for an example). Firstly, there is a minimum - at a few hundred MeV for muons - with a steep slope on the low side and a more gentle rise on the high side. This 'relativistic rise' is caused by an extension of the particle's electric field with increasing energy such that the distant-collision contribution to equation A.1 increases as $\ln \beta\gamma$. In reality however, the medium becomes polarized, limiting this field extension and flattening out the rise. Thus the rate of increase of energy loss above the minimum is relatively slow and generally any particle travelling at a momentum greater than that corresponding to its minimum ionization in the medium is referred to as a minimum ionizing particle(MIP).

Table A.1: *Summary of the Variables Used in the Bethe-Bloch Formula*

Symbol	Definition	Units or Value
E	Incident particle energy	MeV
T	Kinetic energy	MeV
$m_e c^2$	Electron mass $\times c^2$	0.510 999 06(15) MeV
r_e	Classical electron radius $e^2/4\pi\epsilon_0 m_e c^2$	2.817 940 92(38) fm
N_A	Avogadro's number	$6.022\,136\,7(36) \times 10^{23}$ mol^{-1}
z	Charge of incident particle in units of electron charge	
Z	Atomic number of medium	
A	Atomic mass of medium	g mol^{-1}
K/A	$4\pi N_A r_e^2 m_e c^2/A$	0.307 075 MeV g^{-1} cm^2 for A=1 g mol^{-1}
I	Mean excitation energy	eV
δ	Density effect correction to ionization energy loss	

Appendix B

The Landau Distribution

In thin materials, the ionization energy loss of a charged particle is given by a small amount of interactions, each with a wide range of possible energy transfers. This gives a characteristic shape to the energy loss distribution. An approximation to the classical formulation of Landau can be written as [44]

$$f(\lambda) = \frac{1}{\sqrt{2\pi}} e^{-\frac{1}{2}(\lambda + e^{-\lambda})} \tag{B.1}$$

where λ represents a normalized deviation from the most probable energy loss $(\Delta E)_{mp}$:

$$\lambda = \frac{\Delta E - (\Delta E)_{mp}}{\xi}, \qquad \text{where} \quad \xi = K \frac{Z}{A} \frac{\rho}{\beta^2} X. \tag{B.2}$$

Here ΔE is the actual loss and ξ the average energy loss given by the first term in the Bethe-Bloch formula. The symbols in the expression for ξ are defined in appendix A apart from ρ which is the density of the medium in question and X which is the pathlength in the material. An expression for $(\Delta E)_{mp}$ can be found in [53].

The shape of the Landau distribution is shown in figure B.1 for a 500 MeV/c muon traversing 1 cm of CsI. The long tail for large energy losses corresponds to interactions where one or more energetic δ electrons are produced. Thus the distribution

is asymmetric and the mean - the variation of which is described by the Bethe-Bloch formula - is generally higher than the peak value. In fact, there is no well defined mean theoretically since the distribution goes to infinity. In practice however, one chooses some high cut off (often arbitrarily) and calculates the mean from the truncated distribution.

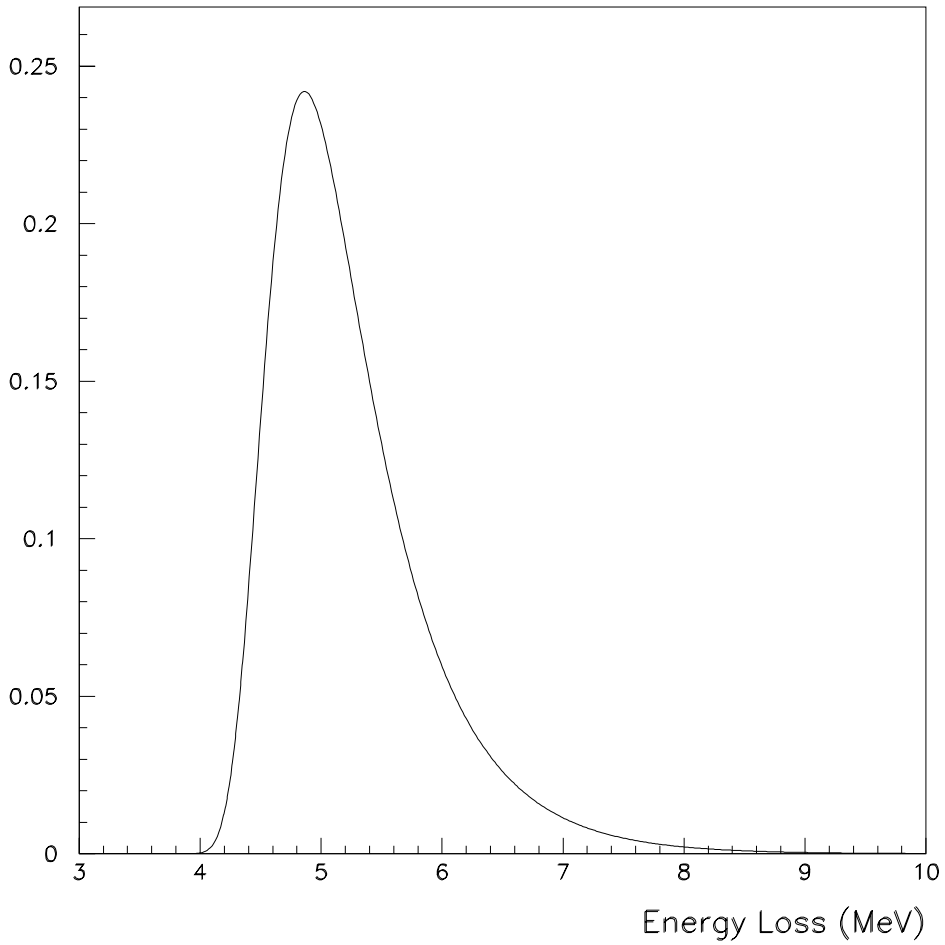

Figure B.1: *The Landau distribution for a muon with momentum 500 MeV/c traversing 1 cm of CsI.*

References

[1] J.H. Christenson, J.W. Cronin, V.L. Fitch and R. Turlay, "Evidence For the 2π Decay of the K_0^2 Meson," Phys. Rev. Lett. **13**, 138 (1964).

[2] A.D. Sakharov, "Violation of CP Invariance, C Asymmetry, And Baryon Asymmetry of the Universe," Pisma Zh. Eksp. Teor. Fiz. **5**, 32 (1967).

[3] M. Kobayashi and T. Maskawa, "CP Violation In the Renormalizable Theory of Weak Interaction," Prog. Theor. Phys. **49**, 652 (1973).

[4] P.F. Harrison and H.R. Quinn [BABAR Collaboration], "The BABAR physics book: Physics at an asymmetric B factory," Sec. 1.2.3 (1998).

[5] C. Caso *et al.*, "Review of particle physics. Particle Data Group," Eur. Phys. J. **C3**, 1 (1998).

[6] P.F. Harrison and H.R. Quinn [BABAR Collaboration], "The BABAR physics book: Physics at an asymmetric B factory," Sec. 1.3 (1998).

[7] J.D. Lewis [CDF Collaboration], "Measurements of the CP-violation parameter $\sin 2\beta$ in $B^0 \to J/\psi K_S^0$ decays," FERMILAB-CONF-99-124-E.

[8] H.H. Williams *et al.*, "A Measurement of the Lepton Charge Asymmetry in $K_L^0 \to \pi^{\pm} l^{\mp} \nu$ Decays," Phys. Rev. Lett. **31**, 1521 (1973).

[9] M. Fabbrichesi, "The $\Delta I = 1/2$ Selection Rule," hep-ph/9607348.

[10] A. Alavi-Harati *et al.* [KTeV Collaboration], "Observation of direct CP violation in $K_{S,L} \to \pi\pi$ decays," Phys. Rev. Lett. **83**, 22 (1999)

[11] V. Fanti *et al.* [NA48 Collaboration], "A new measurement of direct CP violation in two pion decays of the neutral kaon," Phys. Lett. **B465**, 335 (1999).

[12] D.C. Dunbar, J. Forshaw, E.W.N. Glover and T.R. Morris, "Proceedings of the School for Young High Energy Physicists," RAL-TR-1998-023, 137-43 (1998).

[13] P.F. Harrison and H.R. Quinn [BABAR Collaboration], "The BABAR physics book: Physics at an Asymmetric B Factory," Sec. 1.4 (1998).

[14] A. Ali, "B Decays - Introduction and Overview," in *B Decays*, ed. S. Stone, World Scientific(1994).

[15] C. Jarlskog, "A Basis Independent Formulation of the Connection Between Quark Mass Matrices, CP Violation and Experiment," Z. Phys. **C29**, 491 (1985).

[16] C. Jarlskog, "Commutator of the Quark Mass Matrices in the Standard Electroweak Model and a Measure of Maximal CP Violation," Phys. Rev. Lett. **55**, 1039 (1985).

[17] M. Neubert, "B decays and CP violation," Int. J. Mod. Phys. **A11**, 4173 (1996) hep-ph/9604412.

[18] C. Jarlskog and R. Stora, "Unitarity Polygons and CP Violation Areas and Phases in the Standard Electroweak Model," Phys. Lett. **208B**, 268 (1988).

[19] M. Gronau and D. London, "Isospin Analysis of CP Asymmetries in B Decays," Phys. Rev. Lett. **65**, 3381 (1990).

[20] J.P. Alexander *et al.* [CLEO Collaboration], "First measurement of the $B \to \pi l\nu$ and $B \to \rho(\omega) l\nu$ Branching Fractions," Phys. Rev. Lett. **77**, 5000 (1996).

[21] P.F. Harrison and H.R. Quinn [BABAR Collaboration], "The BABAR physics book: Physics at an asymmetric B factory," Sec. 14.2 (1998).

[22] P.F. Harrison and H.R. Quinn [BABAR Collaboration], "The BABAR physics book: Physics at an Asymmetric B Factory," Sec. 3.1 (1998).

[23] T. Sjostrand, "PYTHIA 5.7 and JETSET 7.4: Physics and manual," hep-ph/9508391.

[24] D. Boutigny *et al.* [BaBar Collaboration], "BaBar Technical Design Report," SLAC-R-0457.

[25] "An Asymmetric B factory based on PEP: Conceptual design report," SLAC-0372.

[26] "PEP-II: An Asymmetric B Factory. Conceptual Design Report. June 1993," SLAC-418.

[27] D.C. Carey, K.L. Brown and F.C. Iselin, "Decay Turtle (Trace Unlimited Rays Through Lumped Elements): A Computer Program For Simulating Charged Particle Beam Transport Systems, Including Decay Calculations," SLAC-0246.

[28] GEANT Detector Description Tool, version 3.21, CERN Program Library W5013, CERN(1993)

[29] A. Snyder, "Effect of vertex cuts on CP reach," SLAC-BABAR-NOTE-177.

[30] F. Forti, "TRACKERR studies for optimization of vertex detector resolution," SLAC-BABAR-NOTE-195.

[31] G. Sciolla *et al.* [BaBar Drift Chamber Collaboration], "The BaBar drift chamber," Nucl. Instrum. Meth. **A419**, 310 (1998).

[32] A. Boyarski, D. Briggs and P. Burchat, "Studies of helium based drift chamber gases for high luminosity low-energy machines," Nucl. Instrum. Meth. **A323**, 267 (1992).

[33] B. Ratcliff, "The B factory detector for PEP-II: A Status report," *Presented at 26th International Conference on High Energy Physics (ICHEP 92), Dallas, TX, 6-12 Aug 1992.*

[34] W.W. Allison and P.R. Wright, "The Physics Of Charged Particle Identification: dE/dx, Cerenkov And Transition Radiation," OXFORD-NP-35-83.

[35] P.F. Harrison and H.R. Quinn [BABAR Collaboration], "The BABAR physics book: Physics at an asymmetric B factory," Sec. 3.5 (1998).

[36] G.M. Haller and D.R. Freytag, "Analog Floating Point BiCMOS Sampling Chip and Architecture of the BaBar CsI Calorimeter Front End Electronics System at the SLAC B Factory," SLAC-BABAR-NOTE-285.

[37] J. Dowdell, BaBar Calorimeter DAQ System Overview (BaBar Calorimeter internal note, August 1996).

[38] P.F. Harrison and H.R. Quinn [BABAR Collaboration], "The BABAR physics book: Physics at an asymmetric B factory," Sec. 3.6 (1998).

[39] R. Santonico, R. Cardarelli, A. Di Biagio and A. Lucci, "Progress In Resistive Plate Counters," Nucl. Instrum. Meth. **A263**, 20 (1988).

[40] R. Santonico and R. Cardarelli, "Development Of Resistive Plate Counters," Nucl. Instrum. Meth. **187**, 377 (1981).

[41] N. Dyce *et al.*, The BaBar Trigger Group, "The BaBar Trigger System Design Requirements", V4.71(1997)

[42] S. Gehrig, "Design and Simulated Performance of the Level 1 Trigger System", BaBar Note #380(1997)

[43] L. Lista, "Muon Identification in the IFR", BaBar Note #413(1998)

[44] F. Sauli, "Principles Of Operation Of Multiwire Proportional And Drift Chambers," CERN-77-09.

[45] PAW - Physics Analysis Workstation, Users Guide, CERN Program Library Q121, CERN(1999)

[46] J. Izen *et al.*, "Some Statistics for Particle Identification", BABAR Note #422(1999)

[47] J. Button-Shafer *et al.* "Use of radioactive photon sources with the BABAR electromagnetic calorimeters," SLAC-BABAR-NOTE-322.

[48] Yu.I.Skovpen, "Calibration of Calorimeter with Bhabha Events" SLAC-BABAR-NOTE-356.

[49] Yu.I.Skovpen, "Calibration of Photon Energy with Radiative Bhabha Events" SLAC-BABAR-NOTE-357.

[50] A. Bukin and H. Marsiske, "Absolute Photon Energy Calibration in the BABAR Calorimeter Using π^0's" SLAC-BABAR-NOTE-339 and SLAC-BABAR-NOTE-433

[51] D. Brown, "An object-oriented extended Kalman filter tracking algorithm," *Talk given at Computing in High-energy Physics (CHEP 97), Berlin, Germany, 7-11 Apr 1997.*

[52] J. Mathews and R. L. Walker, "Mathematical Methods of Physics"(2nd Ed.), W. A. Benjamin(1970) and A. Palano, PhD thesis(1971), University of Bari, Italy.

[53] H. D. Maccabee and D. G. Papworth, "Correction to Landau's Energy Loss Formula", Phys. Lett. **30A(4)**, 241(1969)

[54] D.M. Wright, "BEGET: The B Factory event generator. Version 21," SLAC-BABAR-NOTE-149.

[55] P.F. Harrison and H.R. Quinn [BABAR Collaboration], "The BABAR physics book: Physics at an asymmetric B factory," Sec. 5.1.3 (1998).

[56] C.P. Jessop *et al.*[CLEO Collaboration], "Measurement of the decay amplitudes and branching fractions of $B \to J/\psi K^*$ and $B \to J/\psi K$ decays," Phys. Rev. Lett. **79**, 4533 (1997) hep-ex/9702013.

[57] A.S. Dighe, I. Dunietz, H.J. Lipkin and J.L. Rosner, "Angular distributions and lifetime differences in $B_s \to J/\psi\phi$ decays," Phys. Lett. **B369**, 144 (1996) hep-ph/9511363.

[58] P.D. Strother, PhD thesis (1998), University of London (Imperial College)

[59] Developed by R. Barlow at the University of Manchester

[60] P.F. Harrison and H.R. Quinn [BABAR Collaboration], "The BABAR physics book: Physics at an asymmetric B factory," Sec. 3.1.1 (1998).